

**SYNTHESIS AND CHARACTERIZATION OF MULTI-CATALYST POLYELECTROLYTE
MEMBRANES AS PROTECTIVE MATERIALS FOR THE DECOMPOSITION OF CHEMICAL
WARFARE AGENTS**

By

JONATHAN COLÓN-ORTIZ

A dissertation submitted to the

School of Graduate Studies

Rutgers, The State University of New Jersey

In partial fulfillment of the requirements

For the degree of

Doctor of Philosophy

Graduate Program in Chemical and Biochemical Engineering

Written under the direction of

Alexander V. Neimark

And approved by

New Brunswick, New Jersey

May, 2019

© 2019

Jonathan Colón-Ortiz

All Rights Reserved

ABSTRACT OF THE DISSERTATION

SYNTHESIS AND CHARACTERIZATION OF MULTI-CATALYST
POLYELECTROLYTE MEMBRANES AS PROTECTIVE MATERIALS FOR THE
DECOMPOSITION OF CHEMICAL WARFARE AGENTS

by JONATHAN COLÓN-ORTIZ

Dissertation Director:

Alexander V. Neimark

There is an urgent need for the advancement of technology to enable the decomposition of chemical warfare agents (CWA) in an effective and efficient manner. Developing materials that can target a variety of CWA has many challenges. However, the development of novel materials has made possible the emergence of self-decontaminating materials to address this threat. A multi-catalytic polyelectrolyte membrane (MC-PEM) composite has been designed to protect users while decomposing particularly nerve and blister agents. It is comprised of a polyelectrolyte membrane that encloses metal-oxide nanoparticles (MONP) within the substrate and incorporates polyoxometalates (POM) on the surface of the substrate. MONP provide the decomposition of nerve agents via hydrolysis and POM provide the catalytic decomposition of blister agents via photo-oxidation, while also providing colorimetric sensing capabilities. This technology is envisioned to be used as a coating layer within military textiles and other applications that require safety against harmful substances.

ACKNOWLEDGEMENTS

God is my strength and all things were possible through Him. I want to thank my parents, Margarita Ortiz and Orlando Colón for believing in me even before I thought I could become a doctor. To my brother and sisters José, Jennifer and Francheska Colón, as a first generation engineer and graduate student I did all this journey to set an example to our family's next generations. To Luz Minerva Lugo and Omar Paoli who were my adoptive parents, figuratively speaking, and inspiration to go get a bachelor's degree in chemical engineering. To my childhood best friends Reynaldo Rosa, Hector Ayala, Yordano López, José Oscar Torres, and Wilfredo Figueroa for supporting me. To my many motherly figures, Marisol Soliván, Pilar Rivera, Sonia Rivera, Idalia Ortiz, Vilma Santiago, Griselle Ortiz, Damaris Lebrón, Lizzy Rosario, Dorothy Oluyemi, and Maria Morales for their immense wisdom and encouragement. To Ramón Ortiz, Rafael Pérez, Dionisio Acosta, Babajide Oluyemi, Frank Morales, Scott Washburn, and Mario Thorp for being role models.

To the Adventist Federation of College Students at the University of Puerto Rico at Mayagüez Campus and all of their members who were a light through my journey during college, especially to, Salim, Kayla, Priscila and Mar Elisha Pérez, Andrea and Luisana Pagán, Rafael Terán, Jaref Rodriguez, Stephanie Ramírez, Joel Cruz, Garbiel Orengo, Jonatan Alicea, Melina Ramírez, Francisco Salas, Misael Montañez, Juan Avellanet, Roddy Vázquez, Amer Otero, Catherine Cuevas, Ana Martínez, Yeida and Natalie Rivera, Elvin Estremera, Edgardo Cintrón, Matthew and Marlene Hernández, Enid Dipiní, Hector Ayala, Janice Jiménez, David Acevedo, and Siaritza Milián for making my life so much better and helping finish my bachelor's degree.

To Kevin Calkins, Apoorva Vadlamani, Jessica Lee, Sana Yousaf, Harini Kantamneni, Ashley Pennington, Sebastián Escotet, Silvio Dantas, Sean Burgess, Clara Hartmanshenn, Ileana Marrero, Yoliem Miranda, Katherine Koh, Tao Zhang, Yifan Wang, Krizia Karry, Jieun Yang, Heveline Follman, and Taís Silva for making my experience at Rutgers University an unforgettable experience.

I would like to thank the Rutgers University faculty, staff and colleagues for an enriching and learning experience, particularly Lynn DeCaprio, Lobna Elberri, Charanjeet Kaur, Charlie Roth, Evelyn Erenrich, Dawn Lopez, Tewodros Asefa, and John Landers.

Finally, I would like to express my deepest appreciations to my advisor Alexander Neimark for his immense patience, wisdom, knowledge, and friendship. You were the key person that guided me to achieve a dream that I would have ever imagine fulfilling, my doctorate degree. I will be forever thankful.

DEDICATION

*This work is dedicated to my beloved sisters,
Jennifer Colón and Francheska M. Colón*

TABLE OF CONTENTS

ABSTRACT OF THE DISSERTATION.....	ii
ACKNOWLEDGEMENTS	iii
DEDICATION	v
TABLE OF CONTENTS	vi
LIST OF FIGURES	ix
LIST OF TABLES	xii
CHAPTER 1. Background and Motivation.....	1
1.1 CHEMICAL WARFARE AGENT (CWA) BACKGROUND.....	1
1.2 CWA DECOMPOSITION PATHWAYS.....	3
1.2.1 GENERAL MECHANISMS FOR THE HYDROLYSIS OF CWA	3
1.2.2 GENERAL MECHANISMS FOR THE OXIDATION OF CWA.....	3
1.2.3 METAL-OXIDES AS CATALYSTS FOR THE DECOMPOSITION OF CWA.....	4
1.2.4 POLYOXOMETALATES AS CATALYSTS FOR THE DECOMPOSITION OF CWA.....	7
1.2.5 METAL-ORGANIC FRAMEWORKS AS CATALYSTS FOR THE DECOMPOSITION OF CWA	10
1.2.6 ZEOLITES AS CATALYSTS FOR THE DECOMPOSITION OF CWA	15
1.3 CURRENT TECHNOLOGY FOR CWA DECOMPOSITION.....	17
1.4 MULTI-CATALYST POLYELECTROLYTE MEMBRANE DESIGN	18
CHAPTER 2. Objectives and Research Approach.....	20
2.1 CHARACTERIZATION OF <i>IN-SITU</i> GROWTH OF MONP IN PEM.....	20
2.2 HYDROLYTIC DECOMPOSITION OF CWA AND SIMULANTS	20
2.3 PHOTO-OXIDATIVE DECOMPOSITION OF CWA AND SIMULANTS	21
2.4 TRANSPORT PROPERTIES AND PROTECTIVE CAPABILITIES OF PEM COMPOSITES	21
CHAPTER 3. Materials & Methodology.....	23
3.1 MATERIALS.....	23
3.1.1 SOLVENT CASTING OF NEXAR™ & SEBS FILMS	23
3.1.2 SYNTHESIS OF <i>IN-SITU</i> GROWN MONP IN PEM	23
3.1.3 SYNTHESIS OF EX-SITU GROWN MONP AND OXYGEN VACANCY INDUCTION	24
3.1.4 SYNTHESIS OF MESOPOROUS METAL-OXIDES.....	24
3.1.5 SYNTHESIS OF K ₅ CoW ₁₂ O ₄₀ ·20H ₂ O POM	25
3.2 METHODS	26

3.2.1	MANIPULATION OF MORPHOLOGY AND PARTICLE SIZE DISTRIBUTION OF IN-SITU GROWN MONP WITHIN PEM	26
3.2.2	EVALUATION OF THE POM DETOXIFICATION PERFORMANCE AGAINST CEES AND EES VAPORS.....	27
3.2.2.1	Vials-in-Vial closed vapor adsorption system	27
3.2.2.2	Gas Chromatography – Mass Spectrometry (GC-MS)	27
3.2.3	SURFACE AREA AND POROSITY ANALYSIS	27
3.2.4	STRUCTURAL AND MORPHOLOGICAL CHARACTERIZATION	28
3.2.4.1	X-ray diffraction (XRD)	28
3.2.4.2	Scanning Transmission Electron Microscopy (STEM)	28
3.2.4.3	Transmission Electron Microscopy (TEM)	28
3.2.4.4	Thermogravimetric Analysis (TGA).....	29
3.2.5	SURFACE CHEMISTRY AND CHEMICAL ANALYSIS	29
3.2.5.1	Field-Emission Scanning Electron Microscopy (FESEM) with Energy-Dispersive X-Ray Spectroscopy (EDX).....	29
3.2.5.2	Thermal Analysis (TA) coupled with Mass Spectrometry (MS)	29
3.2.5.3	X-Ray Photoelectron Spectroscopy (XPS)	29
3.2.5.4	Nuclear Magnetic Resonance (NMR) Spectroscopy	30
3.2.6	OPTICAL PROPERTIES ANALYSIS	30
3.2.6.1	Diffuse reflectance Ultraviolet-Visible-Near Infra-Red (DRUV-Vis-NIR)	30
3.2.6.2	Diffuse Reflectance Infrared Fourier Transform Spectroscopy (DRIFTS)	30
<u>CHAPTER 4. Characterization of <i>in-situ</i> Growth of MONP in PEM.....</u>		<u>31</u>
4.1	<i>IN-SITU</i> GROWTH OF ZNO WITHIN PEM	31
4.2	MANIPULATION OF <i>IN-SITU</i> GROWN ZNO PARTICLE SIZE DISTRIBUTION WITHIN PEM	36
4.3	MANIPULATION OF <i>IN-SITU</i> GROWN ZNO MORPHOLOGY WITHIN PEM	39
<u>CHAPTER 5. Hydrolytic Decomposition of CWA and Simulants.....</u>		<u>44</u>
5.1	SURFACE MODIFICATION ON MONP TO IMPROVE REACTIVITY AGAINST CWA AND SIMULANTS.....	44
5.2	CWA SIMULANT REACTIVITY AGAINST SURFACE-MODIFIED ZrO ₂ /Zr(OH) ₄	50
<u>CHAPTER 6. Photo-Oxidative Decomposition of CWA and Simulants</u>		<u>62</u>
6.1	PHYSICAL AND CHEMICAL CHARACTERIZATION OF POM.....	63
6.2	PHOTO-OXIDATIVE CAPABILITIES OF POM AGAINST H-AGENT SIMULANTS.....	70
6.3	COLORIMETRIC SENSING CAPABILITIES OF POM WITH RESPECT TO H-AGENT SIMULANTS.....	77
<u>CHAPTER 7. Transport Properties and Protective Capabilities of PEM Composites.....</u>		<u>80</u>

7.1 DMMP SORPTION WITHIN MONP-PEM COMPOSITES	80
7.2 LIQUID WATER-AND WATER-VAPOR SORPTION WITHIN MONP-PEM COMPOSITES ..	82
7.3 <i>IN-SITU</i> MONITORING OF DMMP PERMEATION DYNAMICS ACROSS MONP-PEM COMPOSITES	85
 <u>CHAPTER 8. Conclusions and Recommendations on Future Research.....</u>	<u>93</u>
 <u>Bibliography</u>	<u>95</u>

LIST OF FIGURES

Figure 1-1. General hydrolysis mechanism for sarin.	3
Figure 1-2. General oxidation mechanism for sulfur mustard (with potential hydrolysis).	4
Figure 1-3. Schematic of designed multi-catalyst polyelectrolyte system for CWA protection...	19
Figure 4-1. X-ray diffractograms of Nexar-ZnO (black), SEBS-ZnO (red), Nafion-ZnO (green) and reference bulk ZnO (blue).	33
Figure 4-2. TEM micrographs of ZnO in PEM substrates (left) and their respective ZnO particle size distributions (right): (a) Nexar-ZnO, (b) Nexar-ZnO PSD – n=70, (c) SEBS-ZnO, (d) SEBS-ZnO PSD – n=150, (e) Nafion-ZnO, (f) Nafion-ZnO PSD – n=50.	34
Figure 4-3. TGA thermographs of SEBS-H ⁺ (black), SEBS-ZnO (magenta), Nexar-H ⁺ (green), Nexar-ZnO (brown), Nafion-H ⁺ (blue), Nafion-ZnO (red).	35
Figure 4-4. TEM Images of Nafion-ZnO treated with NaOH (left) and Nafion-ZnO treated with NH ₄ OH (right). Insets are particle size distributions of ZnO nanoparticles in each sample, left – n=50, right – n=100.	37
Figure 4-5. UV-Vis spectra of Nafion-ZnO treated with NaOH (black), Nafion-ZnO treated with NH ₄ OH (red), and Nafion in acid form (blue).	38
Figure 4-6. Wide-angle x-ray diffraction for zinc oxide – Nafion composites prepared with different binary solvent mixtures. The percent of alcohol in the binary mixtures are 20% (black), 40% (blue) 60% (green) and 80% (red). Top inset includes the fitted data for for the low index planes corresponding to composites prepared at different concentrations of alcohol. Y-axis displays the intensity and is in a.u. The bottom inset plots the evolution of the three primary surface planes as a function of alcohol content. The lines correspond to the following planes: solid line – {100}, dashed line – {002} and dotted line – {101}.	41
Figure 4-7. (a) Raw XRD diffractograms of Nexar-ZnO with varying amount of binary solvent/water composition: (black) control Nexar-ZnO, (red) 20 % (v/v) MeOH, (blue) 40 % (v/v) MeOH, (green) 60 % (v/v) MeOH, (magenta) 80 % (v/v) MeOH (b) Fitted XRD diffractograms of Nexar-ZnO with varying amount of binary solvent/water composition: (black) control Nexar-ZnO, (red) 20 % (v/v) MeOH, (blue) 40 % (v/v) MeOH, (green) 60 % (v/v) MeOH, (magenta) 80 % (v/v) MeOH.	42
Figure 4-8. (a) Evolution of the relative peak area of the three main ZnO crystallographic planes as a function of methanol content in solvent: (black) (100), (green) (002), (red) (101) and (blue) the (002)/(100) peak area ratio. (b) Average ZnO nanoaggregate size as a function of methanol content in solvent.	43
Figure 5-1. (a) Nitrogen adsorption isotherms for ZrO ₂ /Zr(OH) ₄ (untreated – red, H ₂ O ₂ treated – blue). Solid squares are adsorption points and open squares are desorption points. (b) Pore size distributions based on NLDFT model (untreated – red, H ₂ O ₂ treated – blue).	45
Figure 5-2. (a) Adsorption Isotherms for untreated CeO ₂ (red) and H ₂ O ₂ treated CeO ₂ (blue). (b) Pore size distribution of untreated CeO ₂ (red) and H ₂ O ₂ treated CeO ₂ (blue) based on a NLDFT model. (c) Adsorption Isotherms for untreated ZnO (red) and H ₂ O ₂ treated ZnO (blue). (d) Pore size distribution of untreated ZnO (red) and H ₂ O ₂ treated ZnO (blue) based on a NLDFT model.	46
Figure 5-3. (a) Zr 3d core level spectrum of untreated ZrO ₂ /Zr(OH) ₄ (b) O 1s core level spectrum of untreated ZrO ₂ /Zr(OH) ₄ (c) Zr 3d core level spectrum of H ₂ O ₂ treated ZrO ₂ /Zr(OH) ₄ (d) O 1s core level spectrum of H ₂ O ₂ treated ZrO ₂ /Zr(OH) ₄	47
Figure 5-4. (a) Aggregate size distributions of untreated ZrO ₂ /Zr(OH) ₄ , inset – TEM micrograph of untreated ZrO ₂ /Zr(OH) ₄ . (b). Aggregate size distributions of H ₂ O ₂ -treated ZrO ₂ /Zr(OH) ₄ , inset – TEM micrograph of H ₂ O ₂ treated ZrO ₂ /Zr(OH) ₄	49

Figure 5-5. X-ray diffractogram of untreated $\text{ZrO}_2/\text{Zr}(\text{OH})_4$ (red) and H_2O_2 treated $\text{ZrO}_2/\text{Zr}(\text{OH})_4$ (blue). Symbols above peaks represent phases of: (*) ZrO_2 , (†) $\text{Zr}(\text{OH})_4$, (‡) NaNO_3 .	49
Figure 5-6. Different reactive sites and hydroxyl groups present on the $\text{ZrO}_2/\text{Zr}(\text{OH})_4$ structure.	50
Figure 5-7. Closer examination of the P=O mode occurring at 1256 cm^{-1} for defect DMCP (top) and occurring at 1288 cm^{-1} for DMHP (bottom) for the H_2O_2 -treated $\text{ZrO}_2/\text{Zr}(\text{OH})_4$.	51
Figure 5-8. Closer examination of the P=O mode occurring at 1256 cm^{-1} for DMCP (top) and occurring at 1288 cm^{-1} for DMHP (bottom) for the untreated $\text{ZrO}_2/\text{Zr}(\text{OH})_4$.	52
Figure 5-9. a) Plausible reaction pathways involving b-OH groups affecting both the control and defective sample. b) Plausible reaction pathways involving water which only affects the defective sample. Red indicates reactive surface bound species. c) The two pathways concluded here.	53
Figure 5-10. Low wavenumber region of DMCP on H_2O_2 -treated $\text{ZrO}_2/\text{Zr}(\text{OH})_4$ between 1400-900 wavenumbers. Inset: Peak height as a function of time. O = 1177 cm^{-1} , X = 1144 cm^{-1} . A lag phase occurs for the first 30 minutes, after which a linear increase in products could be observed. Modes in red represent those attributed to decomposition product. Time intervals between spectra are: 0, 2, 5, 10, 20, 30, 40, 50, 60, 70, 80, 90, 100, 110, 120 min.	55
Figure 5-11. Low wavenumber region of DMCP on untreated $\text{ZrO}_2/\text{Zr}(\text{OH})_4$ between 1400-900 wavenumbers. Inset: Peak height as a function of time. O = 1115 cm^{-1} , X = 1095 cm^{-1} . Modes in red represent those attributed to decomposition product. Time intervals between spectra are: 0, 2, 5, 10, 20, 30, 40, 50, 60, 70, 80, 90, 100, 110, 120 min.	56
Figure 5-12. High wavenumber region of DMCP on H_2O_2 -treated $\text{ZrO}_2/\text{Zr}(\text{OH})_4$. O = 3700 cm^{-1} , X = 3628 cm^{-1} . Modes in red represent those attributed to decomposition product. Time intervals between spectra are: 0, 2, 5, 10, 20, 30, 40, 50, 60, 70, 80, 90, 100, 110, 120 min.	57
Figure 5-13. High wavenumber region of DMCP on the untreated $\text{ZrO}_2/\text{Zr}(\text{OH})_4$. Time intervals between spectra are: 0, 2, 5, 10, 20, 30, 40, 50, 60, 70, 80, 90, 100, 110, 120 min.	58
Figure 5-14. Low wavenumber region of the post heating of DMCP on H_2O_2 -treated $\text{ZrO}_2/\text{Zr}(\text{OH})_4$. O = 1144 cm^{-1} , X = 1177 cm^{-1} . Modes in red represent those attributed to decomposition product. Time intervals between spectra are: 0, 2, 4, 6, 8, 10, 12, 14, 16, 18, 20, 22, 24, 26, 28 min.	59
Figure 5-15. Post-heating comparison of DMCP to DMHP exposure on H_2O_2 -treated $\text{ZrO}_2/\text{Zr}(\text{OH})_4$.	61
Figure 6-1. (a) POM-h powder of bright yellow color, (b) theoretical 3D representation of the structure of $(\text{Co}^{\text{III}}\text{W}_{12}\text{O}_{40})^{-5}$ ion (red spheres – oxygen atoms, blue spheres – tungsten atoms, and the yellow sphere in the core – cobalt atom), and (c) TEM image of POM-h nanorods.	63
Figure 6-2. O 1s, W 4f, Co 2p, S 2p, and K 2p core level spectra of POM-h.	65
Figure 6-3. SEM images of (a-b) POM-h (polyoxometalate phase colored yellow and red, yellow arrows indicate the rod-like POM, red arrows -the orzo like particles, and green arrows-the potassium persulfate phase), (c-d) with the EDX elemental energy histogram as insets, and (d, f) EDX maps with weight percent of detected elements.	67
Figure 6-4. XRD patterns (a), FTIR spectra (b), thermal analysis (TA) curves (c), DTA curves (d), DTG curves (e), of pure KPS and synthesized POM-h nanorods, MS thermal profiles (in helium) of the fragments representing oxygen (m/z 16), O_2 or S (m/z 32), CO_2 (m/z), and SO_2 (m/z 64) for KPS (f), diffuse reflectance UV-Vis-NIR spectra (g), Tauc plots of KPS and POM-h (h).	68
Figure 6-5. The recorder weight uptakes/changes after interactions with CEES or EES vapors for 1 and 7 days under light or in the dark.	71
Figure 6-6. Chromatograms of the headspace after exposure to (a) CEES and (b) EES vapors under light irradiation for 1 (1dL), 3 (3dL), and 7 (7dL) days, and in the dark for 7 days (7dD); (d) the	

names, abbreviations, and the chemical structures of all detected compounds exposed to CEES (c) or EES.....	74
Figure 6-7. (a) Fast and gradual color changes upon the exposure to CEES and EES vapors at ambient light irradiation up to 24 hours, (b) the initial powder and the samples exposed for 1 day under ambient light (1dL) to CEES and EES, (c) the exposed samples to CEES and EES for 7 days under light (7dL), (d) a gradient representation of the gradual color during the exposure to CEES and EES vapors, (e) and the color after exposure of the powder to the droplet of the surrogate...	78
Figure 7-1. a) Sorption of water and b) relative sorption of water (with respect to saturation at 60 minutes) as a function of time within: Nafion-H ⁺ (black squares-dashed line), Nafion-Zn ²⁺ (red circles-dashed line), Nafion-ZnO blue triangles-dashed lines), Nexar-H ⁺ (black squares-solid line), Nexar-Zn ²⁺ (red circles-solid line), Nexar-ZnO (blue triangles-solid line), and SEBS-H ⁺ (green stars-solid line).....	81
Figure 7-2. a) Sorption and b) relative sorption (with respect to saturation at 60 minutes) as a function of time for: Water-Nafion-H ⁺ (black squares-dotted line), Water-Nafion-ZnO (red circles-dotted line), Nafion-H ⁺ (black squares-dashed line), Nexar-ZnO (red circles-dashed line).....	81
Figure 7-3. Water-vapor sorption isotherms (adsorption and desorption branches): (a) Nexar-H ⁺ (black), Nexar-Zn ²⁺ (red), Nexar-ZnO (green) (b) Nafion-H ⁺ (black), Nafion-Zn ²⁺ (red), Nafion-ZnO (green).....	83
Figure 7-4. Wide angle x-ray diffractograms for Nexar-ZnO (black), Nafion-ZnO (green), and hexagonal-lattice bulk ZnO reference (blue).	85
Figure 7-5. Experimental in-operando Raman spectroscopy setup for permeation cell.	86
Figure 7-6. (a) Raman spectra for DMMP samples in solutions of varying concentrations: (gray) 1 vol.% DMMP, (orange) 3 vol.% DMMP, (blue) 5 vol.% DMMP, (green) 10 vol.% DMMP, (violet) 25 vol.% DMMP, (red) 100 vol.% DMMP. Inset shows a closer look at DMMP peak at 7715 cm ⁻¹ . (b) Calibration curve for DMMP based on Raman spectra.	87
Figure 7-7. DMMP spectral evolution at peak located at 715 cm ⁻¹ as a function of time for DMMP permeation through: (a) Nafion-H ⁺ , (b) Nafion-ZnO, (c) Nexar-H ⁺ , (d) Nexar-ZnO.....	88
Figure 7-8. DMMP concentration in receiving compartment as a function of time through: (black triangles) Nafion-H ⁺ , (red triangles) Nafion-ZnO, (blue triangles) Nexar-H ⁺ , and (green triangles) Nexar-ZnO. Error bars are based on standard deviation from duplicate experiments.	89
Figure 7-9. Rearranged DMMP permeation as expressed in Equation 2: (black triangles) Nafion-H ⁺ , (red triangles) Nafion-ZnO, (blue triangles) Nexar-H ⁺ , and (green triangles) Nexar-ZnO. Error bars are based on standard deviation from duplicate experiments.....	91

LIST OF TABLES

Table 1-1. Summary of studies on MONP against various CWA/simulants	6
Table 1-2. Summary of studies on POM against various CWA/simulants	10
Table 1-3. Summary of studies on MOF against various CWA/simulants	14
Table 1-4. Summary of studies on MOF against various CWA/simulants	17
Table 6-1. All identified compounds in the headspace of ViV, along with details on their nomenclature, linear chemical formula, abbreviation, molar mass, and retention times (min) at the chromatograms.....	75
Table 7-1. List of transport properties of DMMP across PEM studied.....	90

CHAPTER 1. Background and Motivation

1.1 Chemical Warfare Agent (CWA) Background

Chemical warfare agents (CWA) are part of a larger group of weapons of mass destruction (WMD), which are known to create mass casualties even with small quantities. These agents can be weaponized via aerosols that can travel through air and target multiple people without detection. Currently, there are various types of CWA, which are classified into their respective categories according to how they affect the human body. Among these lethal agents, there are blister agents, blood agents, and nerve agents. Blister agents, such as sulfur mustard (HD), are known to affect skin, eyes, and the respiratory tract. They can be absorbed by inhalation or through the skin and cause painful and large blisters. Blood agents, such as hydrogen cyanide (AC), are known to affect the ability of blood cells to transfer oxygen causing the body to experience internal suffocation. Nerve agents, such as sarin (GB), are known to inhibit an enzyme called acetylcholinesterase. This enzyme is responsible for aiding in the transmission of nervous impulses through the body. Inhibition of this enzyme effectively causes muscle paralysis, loss of consciousness and eventually death.

The use of CWA goes back to World War I, where lethal gases, such as phosgene and sulfur mustard caused over 1.2 million casualties. In World War 2, Nazi Germany was responsible for the death of several millions of people of whom many of them died due to exposure to hydrogen cyanide gas. There are many other instances in which CWA have been used to cause mass destruction such as: the Vietnam War – where agent orange was used, in a train station in Matsumoto, City Japan – where sarin was used leading to several

deaths and thousands of injured victims, in United States – where letters containing anthrax spores were sent to media and congressional offices and caused the death of 5 officials¹.

The mitigation of chemical warfare agents (CWA) using inorganic materials has been studied for many years going to work from Li et. Al., in 1991² where metal-oxide nanoparticles (MONP) were used as destructive adsorption materials against nerve agent simulants. The choice of inorganic catalysts has been very popular as the synthesis of these can be very cost-effective and straightforward to synthesize. Since then, several types of catalysts have been proposed as destructive sorbents against CWA. The most studied group of inorganic catalysts towards CWA decomposition are metal-oxides systems. Metal-oxides have been shown to decompose nerve and blister agents through hydrolysis mechanisms³⁻⁹. Not only have MONP the capabilities to hydrolyze nerve and blister agents, but also shows oxidative/photo-oxidative capabilities towards blister-agents, particularly oxides like TiO_2 ¹⁰⁻¹⁸. Another popular choice for the catalytic decomposition of CWA include metal-organic frameworks (MOF). MOF, although relatively more difficult to synthesize, show great promise towards the degradation of agents, particularly nerve agents like VX, where it has been reported that the complete decomposition of VX was complete in the order of a few minutes¹⁹⁻²⁵. Less popular alternatives as catalysts have also shown its ability to decompose CWA like polyoxometalates (POM) and zeolites. POM are typically used as photo-oxidative catalysts as they have several active oxygen species available in their surface. It has been reported that POM have the capability to oxidize blister agents and simulants into non-toxic products, but are not as efficient as MOF²⁶⁻²⁸. An interesting aspect about POM nano-clusters is their ability to change colors when CWA are adsorbed to them adding to their oxidative capabilities the ability to be used as sensors²⁹.

1.2 CWA Decomposition Pathways

1.2.1 General mechanisms for the hydrolysis of CWA

In Figure 1-1 a general hydrolysis mechanism is presented where a nerve agent, such as sarin (GB) is decomposed by a nucleophilic attack on the phosphorous atom causing a dehalogenation, fluorine ion leaves, producing an intermediate called isopropyl-methyl phosphonic acid. Subsequently, another attack on the phosphor atom again causes the isopropyl group to leave producing methylphosphonic acid, which is a non-toxic compound³⁰.

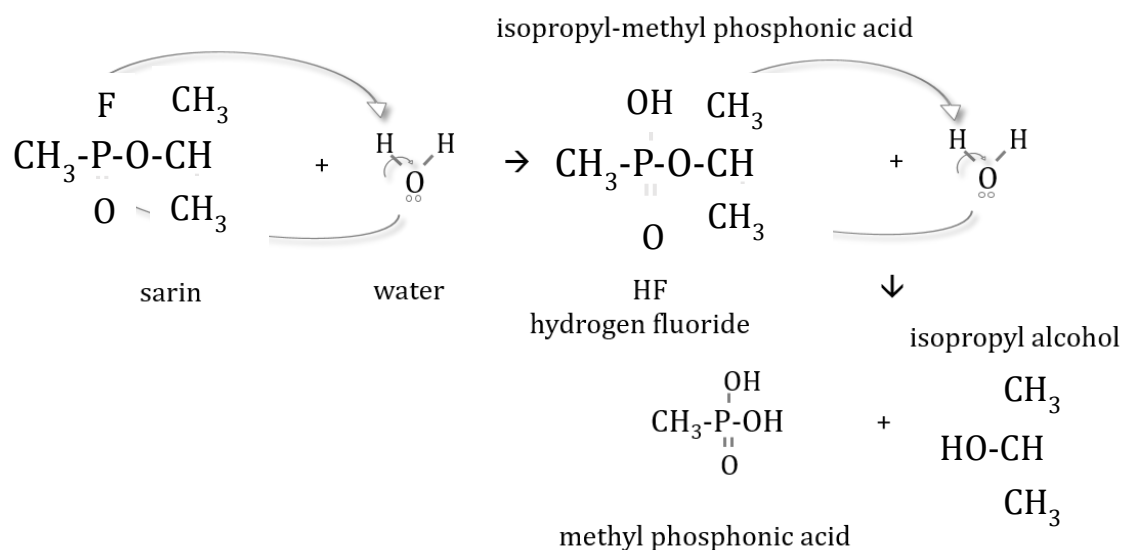


Figure 1-1. General hydrolysis mechanism for sarin.

1.2.2 General mechanisms for the oxidation of CWA

In Figure 1-2 a general oxidation mechanism is presented where a blister agent, such as sulfur mustard (HD) is decomposed by a nucleophilic attack on the sulfur atom causing the production of 2-chloroethyl sulfoxide. This is the desired compound to produce as it is non-toxic. However, a subsequent oxidation on 2-chloroethyl sulfoxide produces an undesired product, which is the 2-chloroethylsulfone. This compound has similar vesicant properties and it poses high toxicity. Once 2-chloroethyl sulfoxide is produced, under the

proper environment, this compound can hydrolyze causing the dehalogenation of one or both chlorides producing an even less-toxic compound named thiodiglycol sulfoxide.

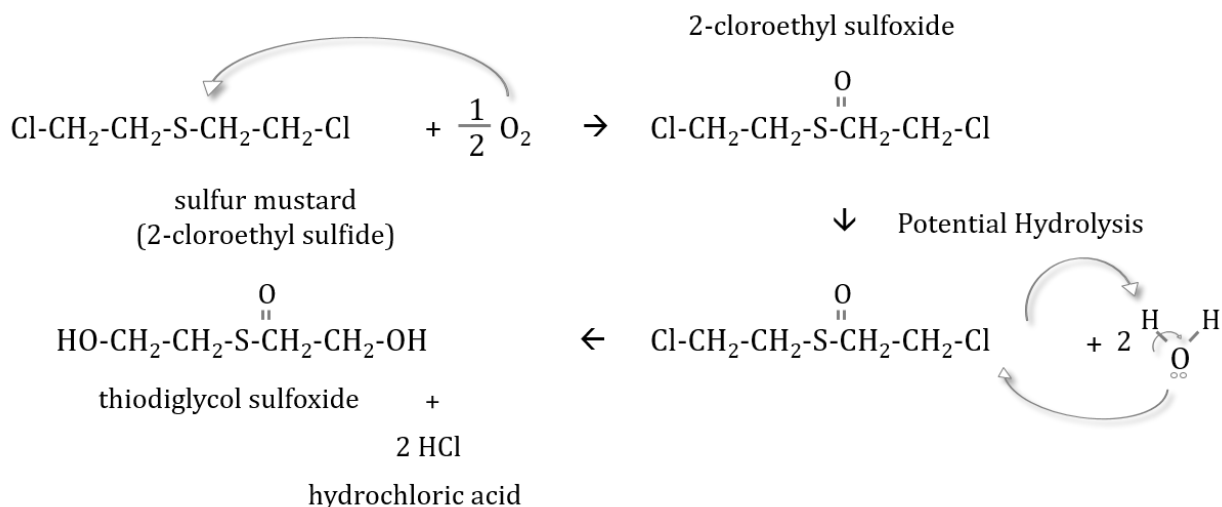


Figure 1-2. General oxidation mechanism for sulfur mustard (with potential hydrolysis).

1.2.3 Metal-oxides as catalysts for the decomposition of CWA

Mahato, et. Al., discuss on the variety of available reactive sites within metal-oxide surfaces, particularly on ZnO ⁶. GB was converted to its hydrolysis intermediate product, isopropyl methylphosphonic acid (IMPA) and consequently to the hydrolysis final product, methylphosphonic acid (MPA). The formed MPA seemed to bind with basic groups existing on ZnO . It appears that ZnO surface area facilitates the adsorption of the agent, such as sarin, and then, the surface hydroxyls and other reactive sites, like edge and surface defects, reacted with the agent thereby rendering the toxic agent to non-toxic product.

Various mechanisms have been proposed for the hydrolysis of G, V, and H agents, which converge to the hydroxyl moieties on metal-oxide surfaces to attach on the phosphorus-halogen (G and H agents) or phosphorus-sulfur bonds (V agents) producing the typical phosphonic acids (G and V agents) and thioglycol (H agents) products. One

drawback of metal-oxide systems is that due to being such strong bases they sorb the catalytic products quite tightly. Bandosz, et. Al., report on the decomposition of VX, HD and GB along with role of surface hydroxyls in $\text{Zr}(\text{OH})_2$ in the hydrolysis of VX⁸. Metal oxides such as MgO and CaO are so basic that they irreversibly sorb the autocatalytic byproduct ethyl methylphosphonic acid (EMPA) onto the surface effectively self-poisoning the EMPA-catalyzed hydrolysis reaction resulting in quite slow VX-reaction rates.

Vernekar, et. Al. have studied how oxygen vacancies on cerium oxide improve the catalytic activity for the decomposition of paraoxon³¹. Vacancy engineered cerium oxide surfaces show superior decontamination of paraoxon, a nerve agent simulant, due to the selective and preferential binding of water and paraoxon with multi-valent $\text{Ce}^{+3}/\text{Ce}^{+4}$ sites. Cerium oxide containing only Ce^{4+} ions favors the binding of paraoxon throughout the catalyst surface since phosphoryl oxygens are attracted to metal-oxide surfaces, but the binding and activation of water molecules on cerium oxide surfaces is disfavored. On the contrary, when cerium oxide surfaces exhibit a large number of Ce^{3+} ions adsorption of H_2O molecules is favored adsorption of paraoxon is disfavored. Therefore, having mixed oxidation cerium states have a synergistic effect as the preferential binding of H_2O at Ce^{3+} sites and paraoxon at Ce^{4+} sites allows for an efficient hydrolysis decomposition.

Tang, et. Al., discussed that the activity of MONP towards the decomposition of HD highly depended on the surface acid–base properties of MONP and the amount of adsorbed H_2O on MONP surfaces³². An increase in surface acidity or basicity was able to improve the degradation of HD over the oxides. More than 10 kinds of products from hydrolysis, were observed based on various mechanisms such as elimination and addition–elimination

reactions for HD over aluminum oxides. It is suggested that the elimination of HCl from HD was accomplished by basic and possibly Lewis acid sites of the oxide surfaces. HD hydrolysis against metal-oxides occurred through the cleavage of both C–Cl and C–S bonds as also reported by Singh et. Al.³³ Moreover, the presence of surface hydroxyls and water on metal-oxide surfaces significantly improves the hydrolysis rate of HD as also observed by Zafrani et. Al.³⁴

Table 1-1 shows selected references of MONP that have been studied for CWA decomposition.

Table 1-1. Summary of studies on MONP against various CWA/simulants

Metal-Oxide	Agent Tested	Environment	Reference
TiO₂	HD	Hexane	Naseri, M.T., et al. (2013) ³⁵
ZnO	Sarin	Dosed onto the catalyst	Mahato, T.H., et al. (2009) ³⁶
ZnO/CuO	GB HD	Dichloromethane	Kumar, P., et al. (2013) ³⁷
Al₂O₃	VX/GB/HD/GD	Injected into catalyst	Wagner, G.W., et al. (2001) ³⁸
CaO	VX/GB/HD/GD	Injected into catalyst	Wagner, G.W., et al. (2000) ³⁹
Nanotube TiO₂	VX/GD/HD	Aqueous	Wagner, G.W., et al. (2008)
Polysulfone fibers with MgO	Paraoxon	Heptane	Sundarrajan, S., et al. (2007) ⁴⁰
TiO₂	DMMP	Ultrahigh vacuum	Panayotov, D.A., et al. (2009) ⁴¹
Al₂O₃/ MnO_x	DMMP	Slurry	Mitchell, M.B., et al. (2011) ⁴²
CeO₂	Paraoxon	N-methylmorpholine	Vernekar, A.A., et al. (2016) ⁴³
Zr(OH)₄	GD HD VX	Dosed onto the catalyst	Bandosz, T.J., et al. (2012) ⁴⁴
Fe&Mn Oxides	HD Soman	Dosed onto the catalyst	Stengl, V., et al., (2012) ⁴⁵
CeO₂	Parathion-methyl	Hexane	Janos, P., et. Al. (2015) ⁹
CaO, MgO, Fe₂O₃, TiO₂	CEES HD Paraoxon	Organic solvent	Koper, O., et. Al. (1999) ⁴

1.2.4 Polyoxometalates as catalysts for the decomposition of CWA

POM have been extensively used as catalysts for one-pot synthesis of complex molecules⁴⁶⁻⁴⁸, water and alcohol oxidation⁴⁹⁻⁵¹, CWA oxidative decomposition^{27, 52}, and have been incorporated in a variety of ceramic and organic substrates such as metal-organic frameworks (MOF)⁵³⁻⁵⁶, metal-oxides⁵⁷⁻⁵⁸, zeolites⁵⁹, and polymers^{28, 60}. POM have the advantage of being environmentally friendly, relatively cheap and photo-reactive. Among the variety of POM available, the Keggin-type polyanions are among the most structurally robust and promising in terms of reactivity⁶¹. These heteropoly-acids are known to be highly stable in humid and aerated environments, low in toxicity and capable of undergoing fast reversible redox reactions. In addition, they exhibit the ability to change color when an oxidizing moiety reacts with the POM and the core transition metal within the POM reduces its oxidation state. It was reported that POM color transitions are different when having a different core transition metal incorporated within the POM structure⁵². This colorimetric detection feature can be used for the development of CWA sensors.

Mizrahi, et. Al. have proposed generalized mechanisms of reaction for the hydrolysis of VX and GB and oxidation of HD on $(\text{NH}_4)_3\text{PW}_{12}\text{O}_{40}$ ²⁷. VX oxidation may occur either on the sulfide or iso-propyl amine group. It is important that high selectivity is achieved towards the oxidation on the sulfur, as it will yield a subsequent hydrolysis reaction to ethylmethyl phosphonic acid (EMPA) products much faster than if the amine group is oxidized. Similarly, GB undergoes a nucleophilic attack on the phosphorous which induces the elimination of fluorine and production of isopropylmethyl phosphonic acid (IMPA), which can undergo through a second nucleophilic attack inducing the isopropyl alcohol group to be eliminated producing MPA as described in Section 1.2.1. It appears as

the $[\text{PW}_{12}\text{O}_{40}]^{3-}$ anion is responsible for the nucleophilic attack on the phosphorous atom of both organophosphates.

Kinnan, et. Al., report the use of polyoxoniobates, $\text{X}_8[\text{Nb}_6\text{O}_{19}]$ (where $\text{X} = \text{Li}^+, \text{K}^+$, or Cs^+), for the hydrolysis of nerve agents and simulants such as GB, soman (GD), and difluorophosphate (DFP).⁶² The change in cation in the polyoxoniobate salt (Li^+ , K^+ , and Cs^+) appears to not have much of an impact when decomposing GB, half-life of 0.03 hr, but does impact the degradation of DFP as the half-life goes from 3.2 hr to 27 hr for $\text{Li}_8[\text{Nb}_6\text{O}_{19}]$ and $\text{Cs}_8[\text{Nb}_6\text{O}_{19}]$, respectively. For GD the half-life increased with increasing the ratio of agent to catalyst from 0.27 hr to 1.54 hr against $\text{Li}_8[\text{Nb}_6\text{O}_{19}]$. It appears as the diffusion of GD to the catalyst is the rate-limiting step.

Giles et. Al., report the use of Wells-Dawson POM $\text{K}_8[\text{Ni}(\text{H}_2\text{O})(\alpha_2\text{-P}_2\text{W}_{17}\text{O}_{61})] \cdot 17\text{H}_2\text{O}$ and $\text{K}_{15}\text{H}[\text{Zr}(\alpha_2\text{-P}_2\text{W}_{17}\text{O}_{61})_2] \cdot 25\text{H}_2\text{O}$. They present that the Zr^{4+} based POM generates several reactive species such as a Venturello complex $[\text{PO}_4[\text{W}(\text{O})(\text{O}_2)_2]_4]^{3-}$, and other tungsten peroxo species when in an aqueous 15 wt% hydrogen peroxide solution. The resulting half-life of Demeton-S was 2.2 min. Much faster when compared to 15 wt% hydrogen peroxide solution without incorporated POMs, which resulted in a half-life of 40.9 min

The versatility of a material that can sense and decompose agents has brought polyoxometalates (POM) to the attention of many researchers. Guo, et. Al., report the successful oxidation of CEES against $\text{K}_4\text{Li}_2[\text{MnV}_{14}\text{O}_{40}] \cdot 21\text{H}_2\text{O}$ in the presence of *tert*-butyl hydroperoxide. In addition, this catalyst has the ability to change colors, from orange to green, which is due to the reduction of V(V) to V(IV) by CEES⁶³. Similarly, Johnson, et. Al., have studied the potential sensing/detecting capabilities of POM based oxidation

reactions. They found that the colors changes observed on POM depend on the metal in the core of the POM structure. The multiplicity in oxidation states of these metallic cores in POM make them quite reactive.

Wu, et. Al, also took advantage of the color changing characteristic of POM against the decontamination of CEES by using phosphorus based POM on polymeric substrates²⁸. $H_5PV_2Mo_{10}O_{40}$ was incorporated into a blend of poly-vinyl alcohol (PVA) and polyethyleneimine (PEI) with a ratio of 10:20 wt.% of PVA:PEI. Using infrared spectroscopy (IR) they were able to detect the decomposition of CEES into its sulfoxide oxidation product. When CEES was exposed to $H_5PV_2Mo_{10}O_{40}$ the sulfur atom in CEES is oxidized into the sulfoxide product reducing the Mn(III) to Mn(IV) yielding a red POM. When Mo^{6+} is substituted by V^{5+} the catalyst exhibits a color change from orange to blue when exposed to CEES also yielding oxidative products of CEES.

Liu, et. Al. were able to impregnate nylon-6 fibers with molybdenum ($H_{3+n}PMo_{12-n}VO_n \cdot xH_2O$) and tungsten ($H_3PW_{12}O_{40} \cdot xH_2O$) based POM and observed its oxidative capabilities as these materials are sought to be used in textiles for CWA protection. It was reported that CEES degradation improved by increasing the number of V^{5+} within the POM structure. More reactive lattice oxygen associated to Mo-O-V species are generated by substituting Mo^{6+} with V^{5+} ions.

Below in Table 1-2 are presented selected references of POM that have been studied for CWA decomposition.

Table 1-2. Summary of studies on POM against various CWA/simulants

POM	Agent Tested	Environment	Reference
H₄PMo₁₁VO₄/nylon-6 fiber	HD	Solution-based	Liu, F., et Al. (2014) ⁶⁴
(NH₄)₃PW₁₂O₄₀	VX,GB,HD	Aqueous	Mizrahi, D.M. et Al. (2010) ⁶⁵
H₃PW₁₂O₄₀/TiO₂	HD	Hexane slurry, UV lamp	Naseri, M.T., et Al. (2012) ³⁵
Fe^{III}[H(ONO₂)₂]PW₁₁O₃₉⁵⁻	CEES	Acetonitrile	Okun, N.M., et Al. (2006) ⁶⁶
K₄Li₂[MnV₁₄O₄₀]·21H₂O	CEES	Toluene	Guo, W., et Al. (2015) ⁶⁷
Li₈Nb₆O₁₉	DFP, GD, GB	Water	Kinnan, M., et. Al. (2014) ⁶²
K₅CoW₁₂O₄₀	CEES	Bulk powder	Johnson, R.P., et. Al. (1999) ²⁹
K₁₅H[Zr(α₂-P₂W₁₇O₆₁)₂]·25H₂O	Demeton-S	Aqueous solution	Giles, S.L., et. Al. (2017) ²⁶
K₅CoW₁₂O₄₀	CEES	Bulk powder	Giannakoudakis, D. et. Al. (2019) ⁶⁸

1.2.5 Metal-organic frameworks as catalysts for the decomposition of CWA

Metal-organic frameworks (MOF) are among the most reactive catalysts to date with respect to the decomposition of CWA. MOF are particularly effective against G-type and V-type agents, Katz, et. Al.²¹, report half-lives of 3.5 min for the decomposition of paraoxon (VX simulant) and Moon, et. Al.²³, report half-lives of 1.8 minutes towards the hydrolysis of VX.

Lopez-Maya et. Al., studied the catalytic activity of UiO-66 [Zr₆O₄(OH)₄(bdc)₆] by modifying the MOF catalyst⁶⁹. This modification was done by incorporating basic lithium alkoxides (butyl and ethyl alkoxides) [UiO-66@LiO*t*Bu, UiO-66@LiO*t*Et], missing linker defects [UiO66@AcO], and by introducing acidic Brønsted sites [UiO-66@SO₄H]. It appears that the most reactive catalyst with respect to diisopropylfluorophosphate (DIFP) decomposition is [UiO-66@LiO*t*Bu] with a half-life for P–F bond hydrolysis of 5 min and

complete hydrolysis after 30 min. As the alkoxy chain in the MOF structure is reduced, the catalytic activity is also reduced. The half-life of [UiO-66@LiO*t*Et] is 30 min with complete hydrolysis after 250 min. The unmodified UiO-66 and defect [UiO-66@AcO] show three-fold slower kinetics with respect to [UiO-66@LiO*t*Bu] and lose their activity after 75% conversion of DIFP due to catalyst poisoning. By adding acidic sites such as HSO₄⁻ the catalytic activity drops even further to a 30% DIFP degradation. Therefore, the presence of basic alkoxy sites within the acidic metal centers promote a synergistic efficient catalysis against DIFP. With respect to dimethyl methylphosphonate (DMMP) and CEES, [UiO-66@LiO*t*Bu] is the most reactive having a half-life of 25 min and 3 min and complete conversions after 300 min and 16 min for DMMP and CEES, respectively. [UiO-66@LiO*t*Bu] outperformed all other catalysts studied by this reference.

Similarly, Katz et. Al. studied the catalytic activity of UiO-66 against paraoxon while modifying the bridging ligands in the MOF with NO₂, OH, and NH₂ groups.⁷⁰ Inspired by the naturally occurring reaction of phosphoesterase enzymes in phosphate hydrolysis, the previously mentioned MOFs were synthesized. UiO-66-NO₂ and UiO-66-(OH)₂ were used to compare the amino moiety of UiO-66-NH₂ against aspartate and histidine moieties based on the enzymatic mechanism for the hydrolysis of paraoxon. Half-lives for the hydrolysis of paraoxon were 35, 60, 45, and 1 min for UiO-66, UiO-66-(OH)₂, UiO-66-NO₂, and UiO-66-NH₂, respectively in the presence of a buffer (N-ethylmorpholine, pH 10). Clearly, the presence of a proximal anchored base significantly improves the reactivity of UiO-66 against paraoxon hydrolysis. These base (NH₂) modified UiO-66 are capable of acting as Brønsted bases, which make all the difference as NO₂ and OH modified UiO-66 don't have this capability although they are capable of hydrogen bond donating and receiving as UiO-

66-NH₂. In addition, UiO-67 was also studied by adding amine-based ligands to the linking moieties of the MOF structure. In this case, both a primary amine (NH₂) and a tertiary amine N(Me)₂ ligand was incorporated within the biphenyl dicarboxylate (BPDC) linker in MOF UiO-67. Under the same conditions as the experiments with UiO-66, the half-lives obtained were 4.5, 2, and 2 min for UiO-67, UiO-67-N(Me)₂, and UiO-NH₂, respectively. When half of the catalyst was used, the half-lives were 15, 7, and 3.5 min for UiO-67, UiO-67-N(Me)₂, and UiO-NH₂, respectively. Given that there was a higher reduction in the catalysis of UiO-67-N(Me)₂ the hypothesis is that since the dimethylamino moiety is a stronger base, it is harder to deprotonate in order to regenerate the catalyst.

Moon et. Al., also studied the catalytic activity of UiO-66 and UiO-67 as in the previous reference²⁴. Studies done with ³¹P NMR spectroscopy show that UiO-67, UiO-67-NH₂, and UiO-67-N(Me)₂ selectively hydrolyze the P–S bond in VX to the non-toxic ethyl methyl phosphonate (EMP) anion and 2(diisopropylamino)ethanethiol (DESH). Complete conversion of VX was observed within 15 min [for UiO-67-N(Me)₂] to about 50 min (for UiO-67 and UiO-67-NH₂). Initial half-lives were 1.8 min, 6.0 min, and 7.9 min for UiO-67-N(Me)₂, UiO-67-NH₂, and UiO-67, respectively. The catalytic enhancement in UiO-67-N(Me)₂ and UiO-67-NH₂ may be due to amino group to act as proton-transfer agents. Since the tertiary amine in UiO-67-N(Me)₂ is more basic than the primary amine on UiO-67-NH₂, this tertiary amine moiety facilitates the proton transfer from BPDC linker to bound agent greater than the primary amine. In addition, unmodified UiO-66 shows a VX hydrolysis half-life of 90 min, which is significantly larger than unmodified UiO-67. This reduction in catalytic activity of UiO-66 may be due to steric crowding about the Zr₆ cluster. Since UiO-67 has a longer linking chain, it prevents this steric crowding allowing

easier adsorption of agent molecules within the MOF. Based on results obtained for the decontamination of VX in buffer solution, UiO-67-N(Me)₂ was tested in an aqueous solution without the aid of buffer and was proven to be the most reactive catalyst yielding a selective hydrolysis of the P–S bond half-life of 7 min.

Peterson et. Al., studied the same materials (UiO-66 and UiO-67 with amino functionalized linking ligands) and have observed conversions of DMNP and soman near 100% within the first three minutes²⁵. For DMNP, the hydrolysis half-life was found to be 25 and 0.9 min for UiO-66 and UiO-66-NH₂, respectively and 3.5, 1.9, and 1.5 min for UiO-67, UiO-67-NH₂, and UiO-67-N(Me)₂, respectively. There is significant difference between the reactivity of UiO-66 and UiO-67. UiO-66 has an average pore aperture size of 6Å, while DMNP has kinetic dimensions of 4.5 x 11 Å which makes diffusion inside the MOF structure very difficult. Therefore, reaction on UiO-66 mostly occurs on its surface. Since UiO-67 has an approximate pore aperture size between 8 and 11.5 Å, DMNP can diffuse easier within the MOF structure having much more reactive sites available, thus increasing reactivity significantly. Similar to Moon et. Al., findings, UiO-67 catalysts with amine functional groups showed to be the most reactive²³.

Li, et. Al. worked on studying how methyl-paraoxon hydrolysis reactivity is impacted by MOF particle size⁷¹. In this case, NU-1000 was used in particles sizes that range from 75 to 15,000 nm. Particles size distributions (PSD) obtained from density functional theory (DFT) calculations show that the ratio between mesopores (31Å) and micropores (10Å) increases as the size of NU-1000 nanocrystals decreases. Results show that as mean particle size decreases, the hydrolysis of methyl-paraoxon significantly increases.

Mondloch et. Al., studied the effect that dehydrating MOF structure has on the hydrolytic catalysis of DMNP and GD using NU-1000²². By treating the catalyst at 300 °C terminal aquo and hydroxo ligands were removed and converted bridging hydro to oxo groups (NU-1000-dehyd). The hydrolysis half-life of DMNP appeared to be 1.5 min achieving complete conversion in about 10 min when using NU-1000-dehyd. By dehydrating the MOF structure of NU-1000 four of the six Zr^{IV} ions are six-coordinate or coordinatively unsaturated Lewis-acidic ions. Therefore, two-thirds of metal-ions within the MOF crystal are potentially available as active sites, a large amount when compared to UiO-66. Experiments suggest that one key step in the hydrolysis mechanism involves P=O binding at these Zr^{IV} Lewis-acidic centers in the MOF crystal. Thus the enhancement in reactivity of NU-1000-dehyd.

Table 1-3 shows selected references of MOF that have been studied for CWA decomposition.

Table 1-3. Summary of studies on MOF against various CWA/simulants

MOF	Agent Tested	Environment	Reference
UiO-66-Li-tert-BuO	DIFP DMNP CEES	Aqueous	Lopez, E., et Al. (2015) ⁷²
Cu-BTC	DECNP DECIP Sarin	Chloroform	Roy, A., et Al. (2013) ⁷³
NH ₂ -MIL-101 (Al)- PIB	DIFP	H ₂ O	Bromberg, L., et Al. (2012) ⁷⁴
UiO-67	pNNP	1,4-dioxane, aqueous	Nunes, P., et Al. (2015) ⁷⁵
NU-1000	DMNP	Aqueous	Mondloch, J. E., et Al. (2015) ⁷⁶
PCN-222/MOF-545	DMNP CEES	Methanol, N-ethylmorpholine	Liu, Y., et Al. (2015) ⁷⁷
NU-1000	Paraoxon	N-ethylmorpholine solution	Li, P., et Al. (2015) ⁷⁸
UiO-66	Paraoxon	N-ethyl-morpholine	Katz, M.J., et Al. (2015) ⁷⁹
PCN-222/MOF-545	CEES	Methanol	Liu, Y. et Al., (2015) ⁸⁰
UiO-67	DMNP	N-ethyl-morpholine	Peterson, G.W., et Al. (2015) ⁸¹

	Soman		
UiO-67	VX	N-ethyl-morpholine/ aqueous	Moon, S.Y., et Al. (2015) ²¹
H₃PW₁₂O₄₀ inside NU-1000	CEES	Acetonitrile	Buru, C. T., et. Al. (2017) ¹⁹
UiO-66	Paraoxon	Methanol or Water	Katz., M. J., et. Al. (2014) ²⁰
PMMA/Ti(OH)₄/ UiO-66 Composite	Paraoxon	Water	McCarthy, D. L., et. Al. (2017) ⁸²
MOF-808-activated	DMNP	Water	Moon, S. Y., et. Al. (2015) ²³
CuBTC	VX HD GD	In NMR rotor	Peterson., G. W., et. Al. (2013) ⁸³

1.2.6 Zeolites as catalysts for the decomposition of CWA

Cojocar, et. Al., have reported the photocatalytic oxidative decomposition of HD under various catalysts including zeolite Y with Mn²⁺ and Fe³⁺ phthalocyanines (MPc) trapped within zeolite Y's cavities under UV light. They report that the main reaction products found SO₂, CO₂, HCl, H₂O, bis(2-chloroethyl) sulfoxide, bis(2-chloroethyl) sulfone, and bis(2-chloroethyl) disulfide⁸⁴. Based on the reaction products they suggested that light absorption induces the generation of a radical cation of HD, which reacts with ambient oxygen to produce sulfoxides or induce S-C bond scissions. In the first route with the assistance of the photo-activated catalyst, the thiol radical is oxidized directly to CO₂, SO₂, and HCl. In the second route, the thiol radical undergoes an oxidative dimerization, resulting in disulfides that eventually for sulfoxides and sulfones when encountered with hydrogen peroxides.

Kanyi, et. Al., propose that when CEES is exposed to dry NaX it strongly adsorbs to an oxygen from the zeolite framework removing the chloride from CEES to form a framework-bound ethyl ethyl sulfide carbocation (framework ethoxy ethyl sulfide).⁸⁵ Upon addition of water, the framework-bound ethyl ethyl sulfide carbocation hydrolyzes to 2-hydroxyethyl ethyl sulfide (HEES), a compound that is significantly less toxic and does

not possess the vesicant properties of HD. This reaction appears to be from the direct hydrolysis of the framework ethoxy ethyl sulfide species to form HEES and an acid zeolite site. The same authors on another publication proposed the hydrolytic decomposition of DFP in the presence of NaX and show that DFP either in dry conditions or in the presence of water⁸⁶. DFP undergoes an elimination reaction in the dry zeolite. In the presence of water, DFP undergoes zeolite-catalyzed water hydrolysis via attack at the ester carbon, a mode of hydrolysis that differs from the typical P–F bond cleavage in solution chemistry in the absence of zeolite.

Wagner, et. Al., reported on the reactions between NaY and AgY zeolites against VX, HD, and their simulants⁸⁷. It was reported that NaY was not a suitable catalyst against the decomposition of HD as it produces toxic compounds thiodiglycol (TG) and chlorohydrin (CH), but is effective against VX as it produces the non-toxic ethyl methyl phosphonic acid (EMPA). HD reacted faster on NaY (via hydrolysis) than on AgY, but formed toxic CH-TG whereas on AgY, HD undergoes both elimination of HCl to form divinyl sulfide and hydrolysis followed by cyclization to yield 1,4-thioxane. AgY effectively decontaminates HD, whereas NaY does not. On NaY, only a slower, simple hydrolysis is observed for VX. Hydrolysis of the P – O bond in VX is not observed on either AgY or NaY, thus avoiding formation of toxic products.

Yang, et. Al., studied the decomposition of DMMP on NaX zeolites and found that there is strong adsorption of DMMP in NaX⁸⁸. In addition, there is substantial DMMP decomposition when in the presence of small amounts of water molecules per zeolite cage. The decreasing tendency for DMMP decomposition in the presence of H₂O may be explained by the electron withdrawing character of the H₂O via H-bonding to the

framework oxygen atoms. This lessens the electron-donating nucleophilicity of the framework oxygens. H₂O coordination to the supercage Na⁺ may also serve to lessen its ability to stabilize the leaving group phosphonate⁻¹ and phosphonate⁻² anions.

Table 1-4 shows selected references of MOF that have been studied for CWA decomposition.

Table 1-4. Summary of studies on MOF against various CWA/simulants

Reactive Material	Agent Tested	Environment	Reference
Ag-Z Micromotor	DECP	Aqueous	Singh, V. V., et al. (2015) ⁸⁹
Silicalite-1	CEES	Oxygen	Stout, S. C., et al. (2007) ⁹⁰
NaZSM-5			
NaX	CEES	Oxygen	Kanyi, C. W., et Al. (2009) ⁸⁵
NaX	DMMP	D ₂ O	Yang, S. W., et Al. (2006) ⁸⁸
NaY	VX	Injected into	Wagner, G. W., et Al. (1999) ⁹¹
AgY	HD	catalyst	
NaY-Ionic Liquid Polymer Composite	CEES	Aqueous	Hudiono, Y. C., et Al. (2012) ⁹²
Manganese phthalocyanine on NaY support	HD	Air	Cojocar, B., et. Al. (2008) ⁸⁴
Mn/zeolite-13X	Diethyl sulfide	Air/O ₃ /water vapor	Ramkrishna, C., et. Al., (2017) ⁹³

1.3 Current Technology for CWA Decomposition

Protective materials against chemical warfare agents (CWA), such as nuclear, biological and chemical (NBC) protective clothing, have been evolving from impermeable butyl rubber-based materials to permeable polyurethane foams mixed with activated carbon.⁹⁴ Current technology for the defense against CWA involves the use of a layer of highly porous activated carbon that efficiently traps the CWA molecules within itself. One of the challenges in designing protective wearable gear is the ability of the material to quickly permeate sweat and dissipate heat while blocking penetration of CWA through the protective material. Butyl rubber-based materials, such as earlier generations of NBC

protective clothing, are excellent at blocking hazardous chemicals, since they are impermeable, but are not able to dissipate heat or sweat from the body causing serious heat strain.⁹⁵ One of the most promising technological developments includes the Joint Service Lightweight integrated Suit Technology (JSLIST), a multilayered semipermeable adsorptive textile, as it provides improved chemical protection, more mobility for the user, and heat stress reduction features.⁹⁶ Another challenge is to incorporate components with high capacity to adsorb hazardous substances or catalytic materials within substrates to allow for CWA decomposition as they diffuse through the membranes. Activated carbon is relatively inert towards the decomposition of CWA at room conditions, such that in the event the user has a garment contaminated with CWA, the agent remains live while trapped in the pores of the activated carbon layer⁹⁷. Since current technology faces some practical challenges, it is of interest to study new materials that can be water-permeable while hindering/blocking the diffusion of CWA, mechanically stable, and easy to incorporate into military garments or other textiles designed for chemical protection.

1.4 Multi-Catalyst Polyelectrolyte Membrane Design

A plethora of catalysts have been studied for decomposition of CWA but only a few can be used in practical environments. Catalysts should be stable at ambient conditions, able to catalyze without the aid of solvents and decompose CWA quickly. These aspects are very important since the end goal is to develop a multi-catalytic system that can be incorporated within military uniform fabrics that will be used under harsh environments. Moreover, heat buildup within the suit remains an issue, and activated carbons can adsorb limited quantities of chemical agent before they lose effectiveness. Therefore, new semipermeable membrane barrier materials that could reject chemical agents but allow sweat to pass through⁹⁷. These membranes must provide high water vapor permeability and

be impermeable to CWAs. The systems protective capabilities will arise from the blocking of CWA diffusion through the membrane and by catalyzing their decomposition. For this purpose, we designed a self-detoxifying perm-selective multi-catalyst polyelectrolyte membranes (MC-PEM). Combining nano-segregating PEMs that trap/absorb toxic agents and allow water permeability and multicomponent catalysts that facilitate decomposition of toxic agents by hydrolysis or oxidation. The designed MC-PEM barrier as shown in Figure 1-3, will employ at least two different catalytic agents: metal oxide catalytic nanoclusters created within the membrane pores by an *in-situ* metal-oxide growth procedure to provide G-agent decomposition and polyoxometalate catalysts deposited at the outer surface via layer-by-layer deposition to provide H-agent decomposition and colorimetric sensing.

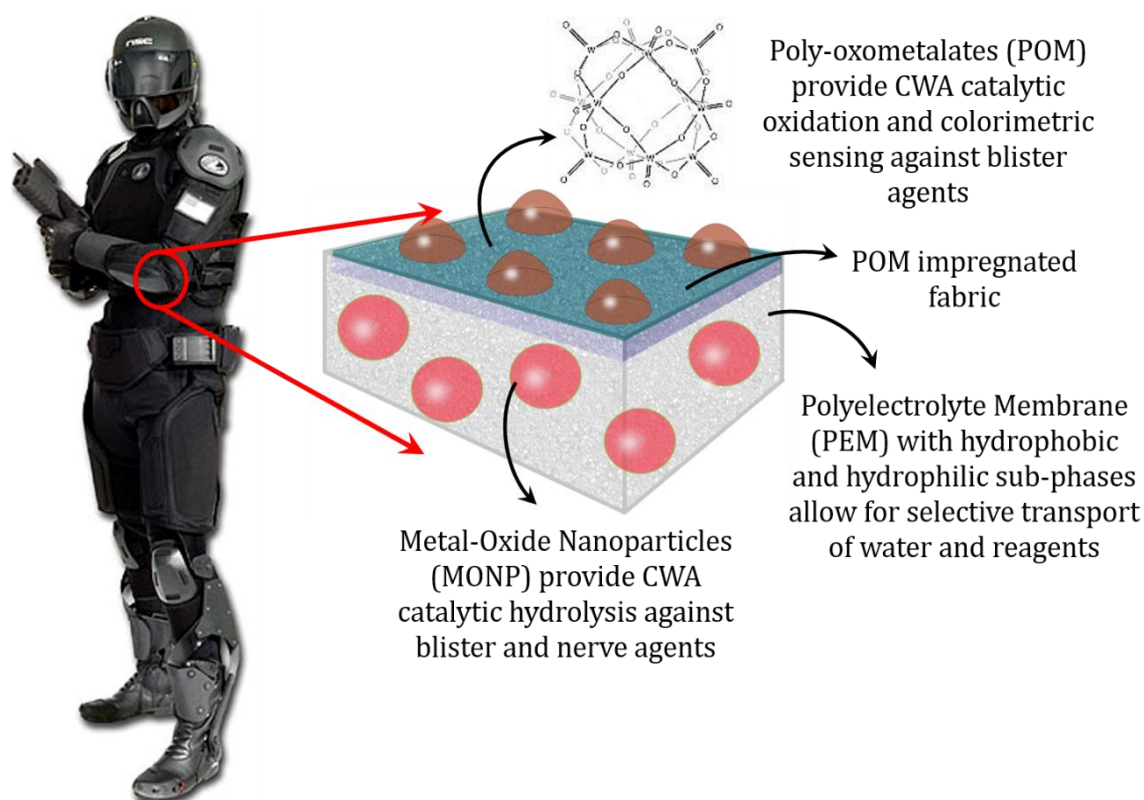


Figure 1-3. Schematic of designed multi-catalyst polyelectrolyte system for CWA protection.

CHAPTER 2. Objectives and Research Approach

2.1 Characterization of *in-situ* Growth of MONP in PEM

As described in Section 1.3, current technology for the defense against CWA involves the use of a layer of highly porous activated carbon that efficiently traps the CWA molecules within its volume. Challenges with the current technology include the hydrophobicity of carbon, which causes the users to suffocate because sweat cannot permeate through the carbon layer of the garment. In addition, activated carbon is relatively inert towards the decomposition of CWA at room conditions, such that in the event the user has a garment contaminated with CWA, the agent remains live while trapped in the pores of the activated carbon layer. Since current technology faces some practical challenges, it is of interest to study a substrate that can be water-permeable while hindering/blocking the diffusion of CWA, mechanically stable, and easy to incorporate into military garments.

2.2 Hydrolytic Decomposition of CWA and Simulants

It is well documented in literature that MONP nanoclusters are capable of hydrolyzing G-type agents quite effectively^{6, 44, 98}. Giannakoudakis, D., et. Al. report that there is near instant decomposition of VX and simulants⁸. Vernekar, et. Al. report half-lives of 17.8 min for the hydrolysis of paraoxon at room temperature against nano-ceria with induced surface defects³¹. Since it has been demonstrated that MONP are effective against the hydrolysis of G-type agents, these systems will be implemented towards the construction of the MONP-PEM composites.

It is of great importance that the reactivity of CWA be as close to instant as possible. Given that in the event that the smallest amount of CWA penetrate the proposed barrier may lead to serious implications on the well-being of the person using this technology, it

is a priority that this material be rigorously tested. The goal is to design a material that can trap CWA within its substrate, react quickly and have the capabilities of being reusable.

2.3 Photo-Oxidative Decomposition of CWA and Simulants

It is desired to develop sensors that can selectively detect the presence of CWA to alert users to the threat of such exposure. Such sensors must be chemically and thermally stable as well as being able to quickly respond to any potential CWA air-borne threats. Several POM candidates have been known for their capabilities to change color when H-agents are adsorbed at the surfaces of these crystalline surfaces. We consider the use of $K_5CoW_{12}O_{40}$ as a potential sensor. Not only can this material change colors from yellow to blue (when an H-agent is adsorbed) but it can also serve as a photo-oxidizing agent for H-agents.

2.4 Transport Properties and Protective Capabilities of PEM Composites

Transport properties of CWA through membrane or fabric systems are of paramount importance when designing protective textiles, as they determine the level of protection when exposed to these agents. Understanding the behavior of CWA/CWS through barriers enables the designer to devise clever ways to enhance the protective qualities of the materials involved in the protective fabric. Our goal is to develop a self-decontaminating barrier that would hinder the diffusion of CWA while providing catalytic centers for the decomposition of such agents.

The proposed research approach to accomplish the above objectives can be summarized as follows:

- Thorough understanding on the growth of MONP within PEM and the factors that influence such growth
- Production of MONP-PEM composites with homogeneously distributed MONP
- Characterize particle size, morphology and MONP content within PEM
- Thorough understanding on the reaction mechanisms involved in the hydrolysis of CWA on MONP and MONP-PEM systems.
- Production of bulk (crystalline and mesoporous) MONP and MONP-PEM composites
- Rigorous analysis on how surface chemistry of catalysts improves their hydrolytic capabilities
- Thorough understanding on the reaction mechanisms involved in the oxidation of CWA on POM clusters
- Rigorous analysis on the colorimetric sensing and oxidative capabilities of POM
- Study the transport properties of MONP-PEM composites against CWA

CHAPTER 3. Materials & Methodology

3.1 Materials

All chemicals pertaining to this research were obtained through Sigma Aldrich and were reagent grade with a purity higher than 98%, unless specified otherwise, and all chemical solutions were prepared in deionized (DI) water. Nafion[®] 117 membranes were obtained through Ion Power and Nexar MD9200 membranes were obtained through Kraton.

3.1.1 Solvent Casting of Nexar[™] & SEBS Films

A 1-L bottle of Nexar[™] MD9200 solution was provided by Kraton and used as received. 30 mL of Nexar[™] MD9200 solution were added to 100 mL of tetrahydrofuran (THF) and solution was kept under vigorous stirring overnight. Once solution was thoroughly mixed 30 mL of solution were added to a Teflon dish and a P2 filter paper was put on top to cover the Teflon dish to slow the rate of THF evaporation in order to make mechanically strong Nexar[™] films. These solutions were casted at room conditions overnight and were washed in DI water to remove any excess solvents. Films recovered had an average thickness of 250 μm .

SEBS solutions were obtained from Sigma Aldrich and used as received. 10 mL of SEBS (5 wt. % in dichloroethane and 1-propanol) were added to a Teflon dish, similarly to Nexar[™], covered with P2 filter paper and let solvent evaporate overnight. Films recovered had an average thickness of 210 μm .

3.1.2 Synthesis of *in-situ* grown MONP in PEM

Synthesis of MONP within PEM started by submerging pre-cut membranes (1 inch by 1 inch cuts) in 1 M HCl for 1-hour at room conditions to remove any impurities. Afterwards, membranes were washed in DI-water to remove excess HCl. After this step

samples were named “PEM-H⁺” where “PEM” represents either Nafion, SEBS, or Nexar (i.e.: Nafion-H⁺). Once membranes were treated with HCl, they were submerged into a metal-impregnation step, using 0.05M solution of metal-nitrate [Zn(NO₃)₂·6H₂O, Ce(NO₃)₃·6H₂O, ZrO(NO₃)₂·xH₂O] for 1-hour at room conditions and were named “PEM-Mⁿ⁺” where “n” is the valency of the metal in solution (i.e.: Nafion-Zn²⁺). Excess salt solutions were removed by washing membranes in DI-water and drying with Kim-wipes. Membranes were then submerged into a hydrolyzing step, where metal ions become metal-hydroxides, in a 0.5 M solution of NaOH at 60 °C for 1-hour and excess NaOH solution was removed by washing membranes in DI-water and drying with Kim-wipes. Samples after this step were named “PEM-M-OH” where “M” denotes the metal that was impregnated in PEM (i.e.: Nafion-Zn-OH). Finally, membranes were put in a muffle furnace at 100 °C, to induce a dehydration on MONP, for 1-hour and the resulting samples were named “PEM-MO” (i.e.: Nafion-ZnO).

3.1.3 Synthesis of ex-situ grown MONP and oxygen vacancy induction

Synthesis of ex-situ MONP was performed by mixing 100 mL of 0.05 M of metal-nitrate solutions with 100 mL of 0.5 M NaOH. Metal nitrate salts hydrolyzed forming metal-hydroxide precipitates. The precipitates formed were decanted and washed with water while filtering. Finally, the resulting powders were dried at 100 °C and annealed at various specified temperatures. For oxygen vacancy-induced MONP³¹, prior to annealing, they are suspended in a 1 M solution of H₂O₂ at 70 °C for two hours, filtered, and then annealed at specified temperatures.

3.1.4 Synthesis of Mesoporous Metal-Oxides

Synthesis of mesoporous metal-oxides was performed by using SBA-15 as a hard-template and dissolving the template to obtain the resulting mesoporous metal-oxide. The

synthesis procedure used can be found elsewhere⁹⁹. The procedure to synthesize SBA-15 consisted of mixing 27.8 g of Pluronic® P-123 (P123) with 504 g of water (where P123 was melted beforehand at 70 °C for 20 minutes) until a homogeneous solution was obtained. Then 15.5 g of 37% HCl solution were added to solution while under vigorous mixing until P123 was completely dissolved and brought to room temperature and left mixing overnight. 60 g of tetraorthosilicate (TEOS) were added to solution and mixture was stirred at 35 °C for 24 hours. Hydrothermal treatment was done by heating solution to 100 °C for 24 hours in a sealed container. Precipitate obtained was filtered using a vacuum pump and was calcined at 550 °C for 10 hours to remove surfactant.

Once SBA-15 was obtained, an incipient wetness impregnation-calcination method was used to make mesoporous metal-oxides. The procedure consisted of dissolving metal-nitrate salts in ethanol and mixing with SBA-15 by ultra-sonicating for 30 seconds. Ethanol was evaporated at 50 °C overnight. The resulting powder was calcined at 200 °C for 4 hours. This powder was then mixed again in an ethanol-metal-nitrate salt solution (for double metal-ion impregnation) and the same mixing and calcining procedure was performed and further calcined to 500 °C for 6 hours. Finally, the silica from the SBA-15 template was dissolved by using 2 M NaOH at 70 °C overnight and the mesoporous metal-oxide was retrieved by centrifugation and filtration.

3.1.5 Synthesis of $\text{K}_5\text{CoW}_{12}\text{O}_{40} \cdot 20\text{H}_2\text{O}$ POM

The synthesis of $\text{K}_5\text{CoW}_{12}\text{O}_{40} \cdot 20\text{H}_2\text{O}$ used can be found elsewhere¹⁰⁰. 19.8 g of $\text{Na}_2\text{WO}_4 \cdot 2\text{H}_2\text{O}$ were dissolved in 40 mL of deionized (DI) water and glacial acetic acid was added dropwise until the pH of the solution reached was 7.0. In a separate flask 2.5 g of $\text{Co}(\text{C}_2\text{H}_3\text{O}_2)_2 \cdot 4\text{H}_2\text{O}$ were dissolved in 12 mL of DI water and 5 drops of glacial acetic

acid were added. The Na_2WO_4 was heated until boiling and the $\text{Co}(\text{C}_2\text{H}_3\text{O}_2)_2$ was added all at once under vigorous stirring conditions and the resulting solution was left mixing at boiling conditions for 15 minutes. 13.0 g of KCl were added to the solution and was let to cool down at room temperature overnight. The precipitate was filtered and was added to 40 mL of 2 M H_2SO_4 and was heated for 5 minutes. The resultant solution was filtered to remove any undissolved solids and was heated until boiling under vigorous stirring. $\text{K}_2\text{S}_2\text{O}_8$ was added to the boiling solution in increments of 0.5 g until the solution turned gold and an extra 1.0 g after solution turned gold. Finally, the gold solution was put in an ice bath to crystallize the final product and was eventually filtered.

3.2 Methods

3.2.1 Manipulation of morphology and particle size distribution of in-situ grown MONP within PEM

When subjecting PEM to the in-situ growth of MONP procedure, as described in section 2.1.2, initially all solutions used were aqueous-based. For the morphological manipulation of the MONP crystal growth within PEM, the original metal nitrate solutions and sodium hydroxide solutions now had increasing amounts of alcohol present in the solution. Methanol (MeOH), ethanol (EtOH), 1-propanol (1-PrOH), and 2-propanol (2-PrOH) were added to 0.5 M of metal nitrate and sodium hydroxide solutions while all other conditions remained the same for the in-situ synthesis of MONP within PEM. For the particle size distribution (PSD) manipulation of MONP within PEM, a weaker base was used during the hydrolyzing step. Instead of using sodium hydroxide, an ammonium hydroxide solution was used while all other experimental parameters remained as described in section 2.1.2.

3.2.2 Evaluation of the POM detoxification performance against CEES and EES vapors

3.2.2.1 Vials-in-Vial closed vapor adsorption system

The adsorption of CEES or EES vapors was studied in batch experiments. Two 1 mL glass vials, the first containing 20 mg of the sample and the other containing 20 μ L of the surrogate (liquid phase) were introduced into a 20 mL reaction vessel closed. The vessel was hermetically sealed using a cap with a septum top. The containers were kept under visible light at room temperature for various intervals of time. The latter was done to allow the complete evaporation of the vapors in the container to ensure the equilibrium of any surface reaction, and to determine the maximum adsorption performance, and to monitor the evolution of the interactions. After specified predetermined reaction times, the containers were opened. The containers with the adsorbents were weighed directly, while they were also weighted after 1, 4, 6, 24, and 48 hours in air at atmospheric pressure. The mass gain as a result of the adsorption/desorption process recorded and expressed as a weight uptake (WU, mg/g).

3.2.2.2 Gas Chromatography – Mass Spectrometry (GC-MS)

The headspace of the closed vials-in-vial system was analyzed by GC coupled with a MS detector (Shimadzu Q5000). The chromatograms were recorded by injecting 40 μ L at 50 °C, with a split ratio of 7. The column was heated from 50 to 340 °C at a rate of 40 °C/min. Helium was used as a carrier gas. The eluting analytes were detected and characterized by mass spectrometry with electron ionization.

3.2.3 Surface area and porosity analysis

Surface area and total pore volume of samples were obtained from an Autosorb-1 N₂ gas adsorption instrument (Quantachrome Instruments). Adsorption/desorption isotherms were obtained at 77 K and 79 points were recorded including 11-points for BET surface area analysis using Quantachrome's Autosorb software version 1.55. Pore size

distributions were calculated using a cylindrical pore non-local density functional theory (NLDFT) model, based on the adsorption branch with N₂ at 77 K adsorption isotherm kernel. Outgassing was performed at 300 °C for three hours.

3.2.4 Structural and morphological characterization

3.2.4.1 *X-ray diffraction (XRD)*

X-ray diffractograms were obtained using a Phillips XPert diffractometer (Bragg-Brentano geometry) with a Cu_{Kα} anode (1.5405 Å). The instrument was operated at 45kV and 40mA with a 0.02 °/step acquisition rate with a dwell time of 2 seconds/step from 2θ angles over the range of 10 ° to 90 ° using a 0.3 mm fixed receiving slit. The software used to collect x-ray diffractograms was X'Pert Data Collector version 2.0e.

3.2.4.2 *Scanning Transmission Electron Microscopy (STEM)*

A high-resolution scanning-transmission electron microscope (Nion UltraSTEM) was used to obtain images of MONP within PEM substrates under a 60kV accelerating voltage in ultra-high vacuum (UHV) conditions.

3.2.4.3 *Transmission Electron Microscopy (TEM)*

Transmission electron micrographs were obtained by a JEOL 1200EX electron microscope with AMT-XR41 digital camera with an accelerating voltage of 80 kV and 2-seconds sample exposure time. Samples were supported on lacey carbon type-A 300 mesh copper grids.

MONP-PEM membranes were pulverized using a dremmel with a sandstone to grind the samples into a very fine powder that was later transferred into 1 mL of ethanol (EtOH) and sonicated for 5 minutes. Three drops of the suspension were added to a TEM copper grid and allowed to air-dry prior to using STEM. All other powder samples were treated the same as pulverized MONP-PEM samples.

3.2.4.4 *Thermogravimetric Analysis (TGA)*

Thermogravimetric analysis (TGA) was performed in a Perkin Elmer Pyris TGA 7 with approximately 2 mg of sample starting at 50 °C using a 5 °C/min ramp rate up to 800 °C with a nitrogen-flowrate of 20 mL/min.

3.2.5 Surface chemistry and chemical analysis

3.2.5.1 *Field-Emission Scanning Electron Microscopy (FESEM) with Energy-Dispersive X-Ray Spectroscopy (EDX)*

FESEM micrographs and elemental maps were obtained by a Zeiss Sigma Field Emission SEM with Oxford INCA PentaFETx3 EDS system (Model 8100) with an acceleration voltage of 20 kV and an aperture of 60 µm.

3.2.5.2 *Thermal Analysis (TA) coupled with Mass Spectrometry (MS)*

Thermogravimetric (TG), differential thermal (DTA) and derivative thermogravimetric (DTG) analyses were obtained under helium atmosphere using a thermal analyzer (SDT Q600, TA instruments). The materials were heated from room temperature up to 1000 °C, at a rate of 10 °C/min. The flow of ultra-dry He was 100 mL/min. The released gases during the thermal analysis were simultaneously analyzed using a gas analysis system (Omnistar GSD 320, Pfeiffer Vacuum). Based on it, thermal profiles for target m/z (17, 35, 44, 64, 73, and 75) were recorded.

3.2.5.3 *X-Ray Photoelectron Spectroscopy (XPS)*

XPS analysis was carried out a Thermo Scientific K-Alpha XPS spectrometer with non-monochromatic Al K α radiation (1486.7 eV) with a 128 channel detection system using a 400 µm diameter analysis area. The Thermo Scientific Advantage software package (version 5.981) was used for acquisition and data analysis. A Shirley-type background was subtracted from the signals. Recorded spectra were fitted using Gauss–Lorentz curves with

an L/G ratio of 0.3, in order to determine the binding energy of the various components of each element core level. The instrumental resolution of the spectrometer is 0.5 eV.

3.2.5.4 Nuclear Magnetic Resonance (NMR) Spectroscopy

Quantitative ^{31}P NMR spectra was obtained by a Varian NMRS 500 MHz using 64 scans with a 1-second delay in decoupled + NOE mode. For all spectra obtained, a 100 μL sample was added to 500 μL of 0.05 M solution of trimethylphosphate (TMP) in deuterated water.

3.2.6 Optical properties analysis

3.2.6.1 Diffuse reflectance Ultraviolet-Visible-Near Infra-Red (DRUV-Vis-NIR)

DRUV-Vis-NIR spectra were obtained between 200 and 1000 nm by using an Evolution 300 UV-Vis Spectrometer (Thermo) with a micro sample cup inside a Praying Mantis diffuse reflectance sphere (Harris).

3.2.6.2 Diffuse Reflectance Infrared Fourier Transform Spectroscopy (DRIFTS)

The in situ IR spectra were recorded with a Nicolet 6700 (Thermo Electron Corporation, Madison, WI) spectrometer equipped with a MCT-A (HgCdTe) detector cooled with liquid N_2 , and with a diffuse reflection accessory (DiffusIR, Pike Technologies, Madison, USA) and a diffuse reflectance cell (DiffusIR environmental chamber, Pike Technologies, Madison, USA). For the DRIFT analysis, the resolution was 2 cm^{-1} , and 128 transients were acquired per spectrum to provide a good balance between signal-to-noise and decent time resolution.

CHAPTER 4. Characterization of *in-situ* Growth of MONP in PEM

This chapter is based on work that has been published to the references shown below, and was used with written permission of publishing company:

- J. Landers*, J. Colón-Ortiz*, et. Al., In situ growth and characterization of metal oxide nanoparticles within polyelectrolyte membranes, *Angew. Chem., Int. Ed.*, 2016, **55**, 11522

* Equally contributing first authors

4.1 *In-situ* Growth of ZnO within PEM

The homogenous distribution of *in-situ* formed MONP within PEM substrates is of vital importance for providing the maximum CWA protection that can be achieved with such system. However, the *in-situ* growth of MONP within PEM is influenced by the substrate's properties. Such properties include the solubility of the solvent in PEM, the micro- and nano-structure of PEM used and chemical environment within the hydrophilic nano-phases where the *in-situ* growth of MONP occurs. All these parameters ultimately impact critical attributes of MONP in PEM, such as MONP morphology, particle size distribution (PSD) and catalytic activity. It is hypothesized that in a hydrated nano-segregated ionomer substrate, such as Nafion, growth of MONP is inhibited by the confining geometry of hydrophilic domains, elastic resistance of the polymer network, as well as by severe diffusion limitations in the hydrophilic subphase. As crystal nucleation occurs and nano-crystals grow, they experience steric forces due to the walls of the ionic domains as the crystal is big enough forcing the crystal growth to stop and yield nano-crystals close to the characteristic volume of the ionic domains. When the PEM has a high

solubility to organic solvent, it is hypothesized that the characteristic volume and shape of the ionic domains change, which in turn would favor the growth of nanocrystals of different morphology based on the geometrical change of the ionic domains due to solvent solvation. To study how PEM physical and chemical properties affect MONP *in-situ* growth in substrates, three kinds of PEM are proposed as candidates, which contain varying degrees of density of ionic moieties per polymer chain: Nafion (grafted copolymer), SEBS (tri-block copolymer), and Nexar MD9200 (penta-block copolymer).

The general scheme of formation of metal oxide nanoparticles within PEM substrates are as follows: First, a 1 inch by 1 inch piece of PEM, such as Nafion, is impregnated with an aqueous solution of zinc nitrate solution. Zn^{2+} ions cluster within the hydrophilic domains via ion-exchange with the sulfonated side chains of the PEM. After allowing the films to saturate with Zn^{2+} ions, the ionic clusters are converted to metal hydroxide nanoparticles, via hydrolysis, by placing the membrane in the presence of a strong base (0.5 M NaOH) at 60 °C. Due to a limited supply of Zn^{2+} , ions continue to hydrolyze to form nanoparticles inside the membrane. The final step involves heating the membranes at 100 °C for duration of 24 h in order to initiate the condensation reaction of the metal hydroxides nanoparticles to metal oxide nanoparticles. This procedure is currently undergoing a patent application process in which a provisional patent application has been granted.¹⁰¹

X-ray diffraction data was acquired to corroborate the presence of ZnO nanoaggregates as shown in Figure 4-1. One can observe that Nafion, Nexar and SEBS do

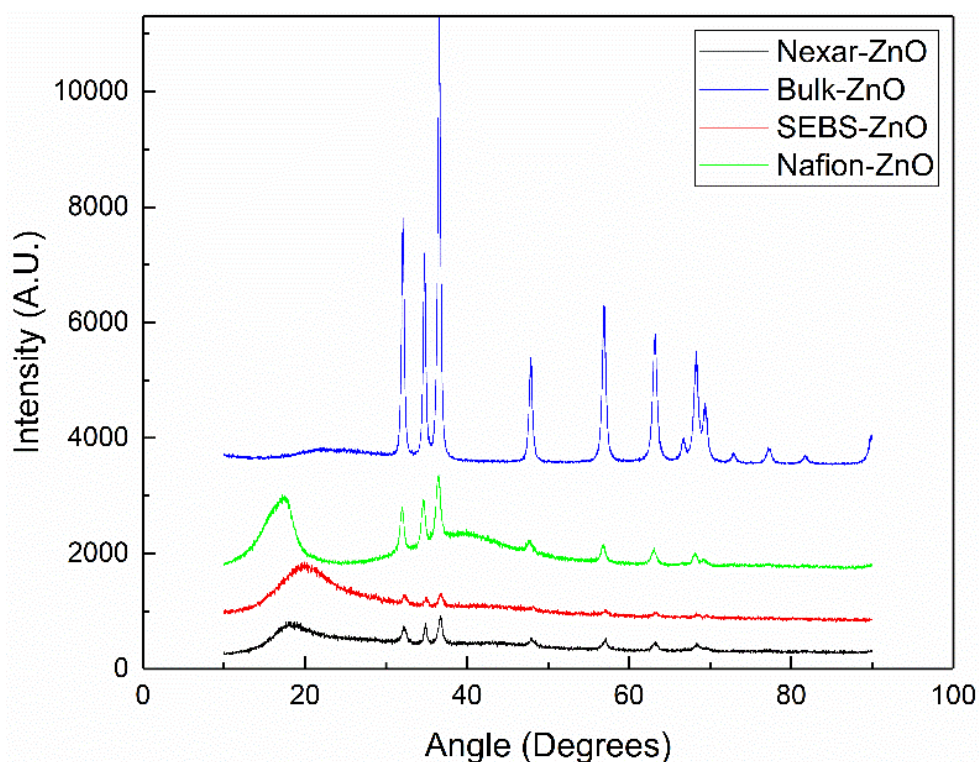


Figure 4-1. X-ray diffractograms of Nexar-ZnO (black), SEBS-ZnO (red), Nafion-ZnO (green) and reference bulk ZnO (blue).

have the characteristic peaks of hexagonal lattice ZnO as they match the superposed peaks of reference bulk ZnO. Once the presence of ZnO was confirmed by XRD, electron microscopy techniques were used to image and quantify the size of the ZnO nanoclusters within the PEM substrates. In Figure 4-2, it can be observed the ZnO particle size distribution within PEM substrates. ZnO nanoparticles range from 2 to 16 nm and have a spherical-like shape in Nexar-ZnO samples. SEBS – ZnO samples host the most homogeneously distributed ZnO nanoclusters as the distribution varies from 3 – 8 nm. Nafion – ZnO samples PSD ranges from 6 to 22 nm. Although all PEM (Nafion, Nexar and SEBS) were subjected to the same conditions for the *in-situ* growth of ZnO, it can be clear that the microstructure of the polymer does play an important role. The PSD of MONP

within PEM can be used as one design factor to help choose the appropriate PEM for the desired application.

Another property of interest of the PEM-MONP system is the amount of ZnO within the substrate per mass of membrane. To analyze the content of ZnO within PEM or

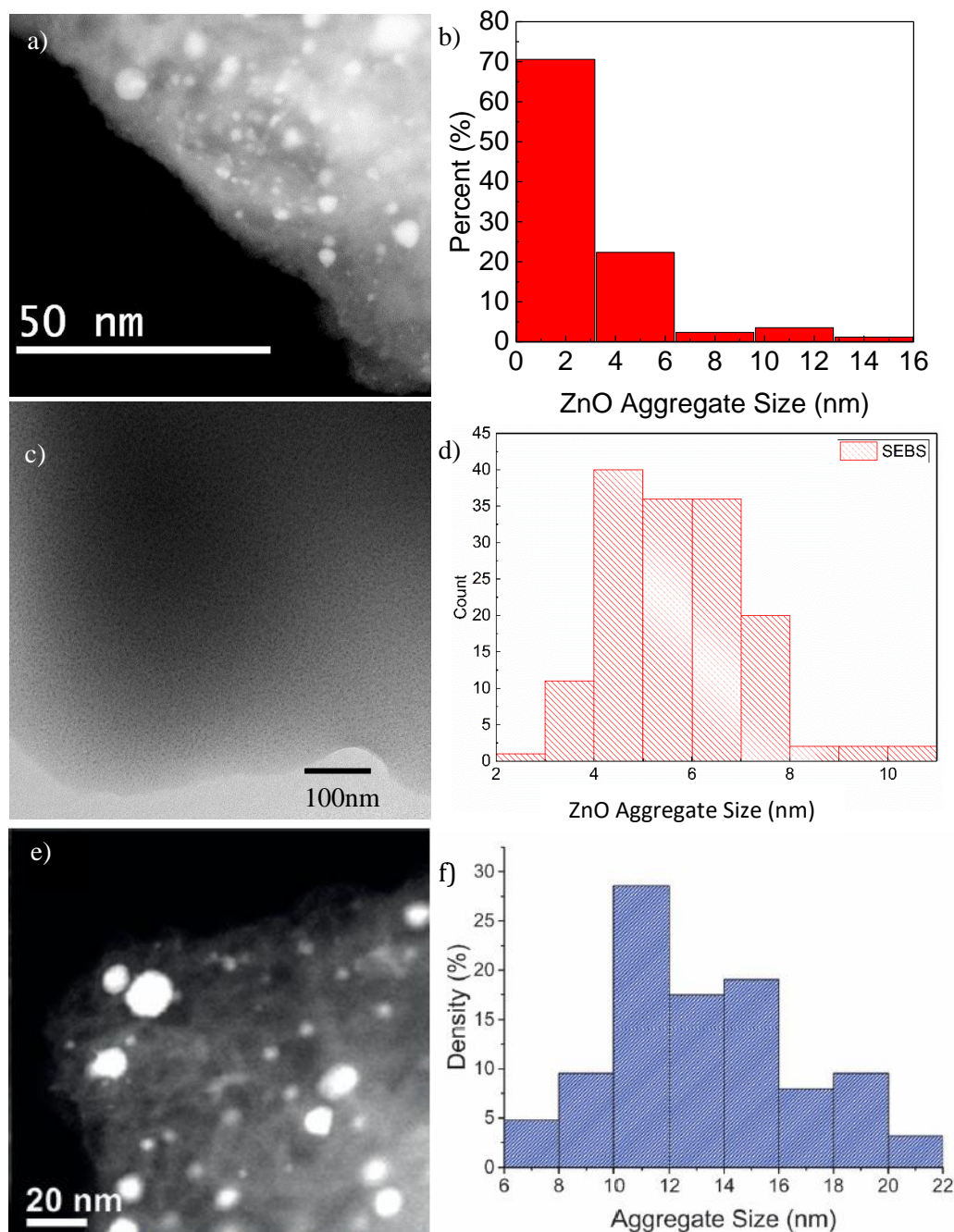


Figure 4-2. TEM micrographs of ZnO in PEM substrates (left) and their respective ZnO particle size distributions (right): (a) Nexar-ZnO, (b) Nexar-ZnO PSD – $n=70$, (c) SEBS-ZnO, (d) SEBS-ZnO PSD – $n=150$, (e) Nafion-ZnO, (f) Nafion-ZnO PSD – $n=50$.

“ZnO loading” thermogravimetric analysis (TGA) was used on PEM- H^+ samples, PEM Zn^{2+} , and PEM-ZnO. TGA experiments were under specified conditions in Section 3.2.4.4.

The amount of ZnO within PEM was calculated by subtracting the residual weight of PEM-ZnO at 600 °C against the weight of PEM- Na^+ and PEM- H^+ , see Figure 4-3. The average amount of ZnO within PEM substrates was approximately 7.7%, 6.1%, and 3.5% (w/w) for Nexar, SEBS and Nafion, respectively. The amount of ZnO within PEM directly correlates with the IEC of each polymer substrate, as the higher the IEC the greater the

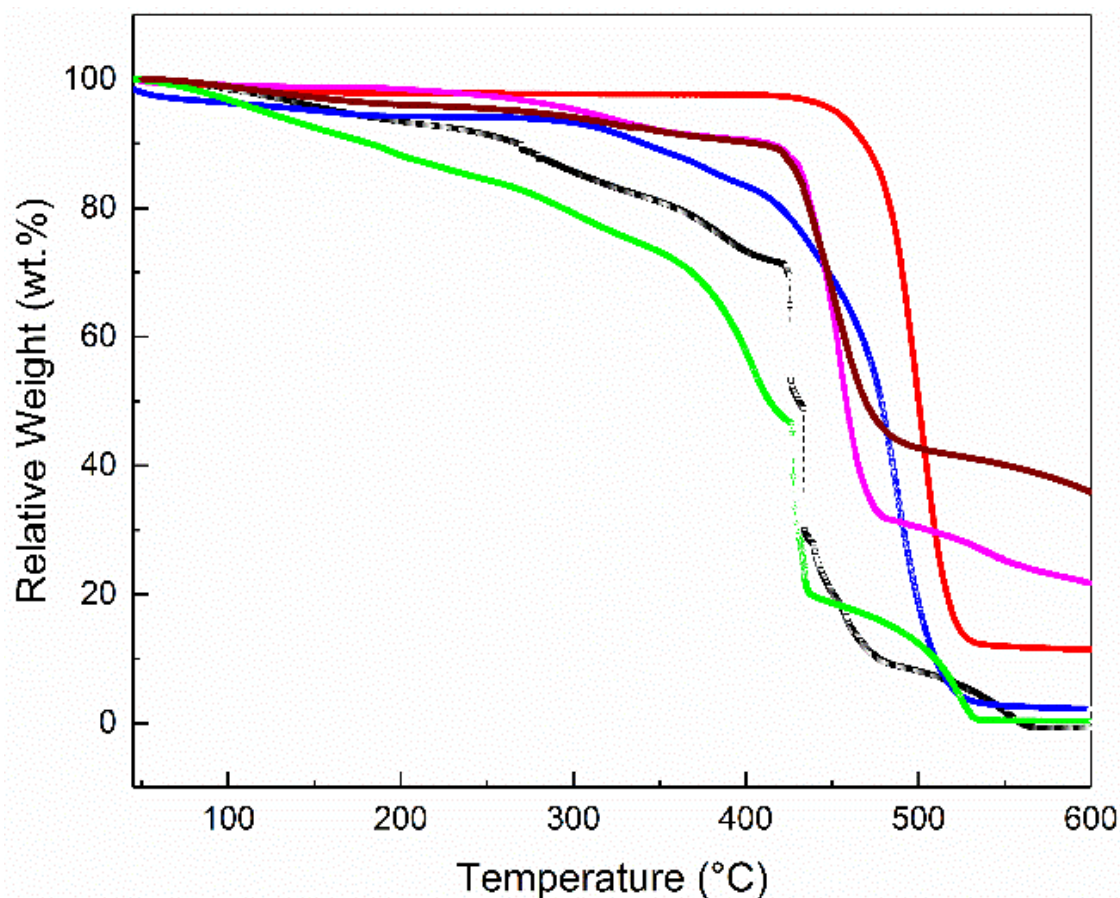


Figure 4-3. TGA thermographs of SEBS- H^+ (black), SEBS-ZnO (magenta), Nexar- H^+ (green), Nexar-ZnO (brown), Nafion- H^+ (blue), Nafion-ZnO (red)

amount of ZnO within PEM (IEC for Nexar, SEBS and Nafion are 2.0, 1.62, and 0.91 meq/g, respectively). The maximum theoretical amount of ZnO that could be “loaded”

within PEM hydrophilic sub-phases was estimated based on the IEC of PEM and assuming complete metal-ion exchange and that all Zn^{2+} ions convert to ZnO. These calculations yield a maximum amount of 8.1%, 6.6%, and 3.7% (w/w) of ZnO within Nexar, SEBS and Nafion, respectively. Therefore, one can calculate the degree of metal-substitution and conversion of ZnO within PEM by dividing the amount of ZnO found experimentally by the maximum theoretical amount, which in this case results in approximately 95% conversion to ZnO across all PEM. This suggests that the vast majority of the sulfonated sites do substitute the H^+ proton to the Zn^{2+} proton and subsequently Zn^{2+} is converted to ZnO.

4.2 Manipulation of *in-situ* Grown ZnO Particle Size Distribution within PEM

An attempt to control particle size of MONP within PEM was done and by changing the hydrolyzing base used for the formation of metal-hydroxides within PEM. As the strength of the hydrolyzing base decreases, the rate at which the metal-hydroxides are formed and grow also decreases. Therefore, using a weaker base such as ammonium hydroxide (pH ~ 10) should yield smaller nanoparticles when compared to using sodium hydroxide (pH ~ 14) for the same amount of time. In Figure 4-4 it can be observed that when using two different bases (NaOH and NH_4OH) in the formation of ZnO in Nafion 117 membranes, ZnO nanoparticles have quite different particle size distributions. TEM images show that when Nafion-ZnO membranes were treated with NaOH, the average particle size is within 15-20 nm. On the other hand, when Nafion-ZnO membranes were treated with NH_4OH the average particle size is within 3-6 nm, which is 3-5 times smaller.

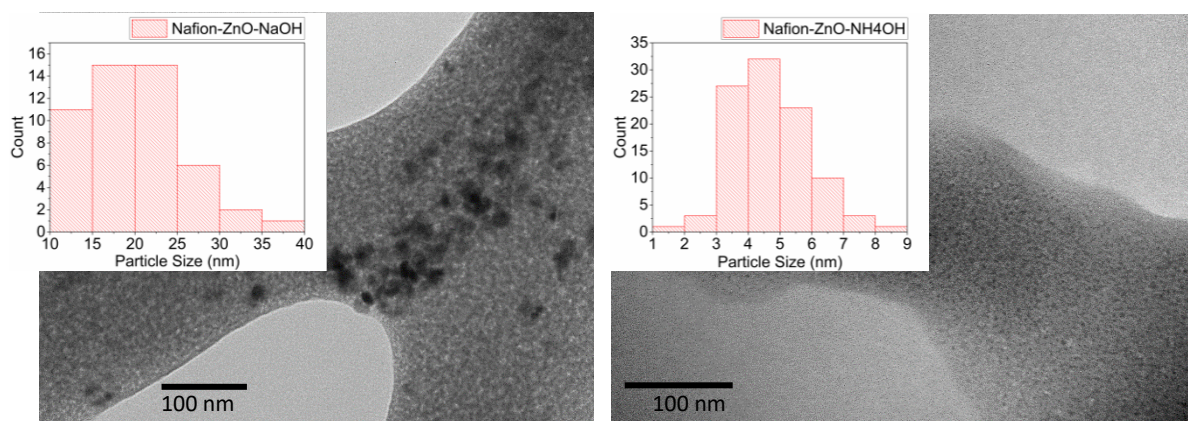
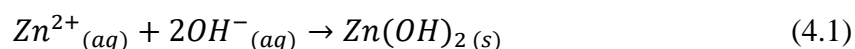


Figure 4-4. TEM Images of Nafion-ZnO treated with NaOH (left) and Nafion-ZnO treated with NH₄OH (right). Insets are particle size distributions of ZnO nanoparticles in each sample, left – n=50, right – n=100.

There are two possible explanations for this phenomenon. One possibility is that in the hydrolysis reaction between the metal-cation and the base, Equation 1, there is a kinetic factor involved.



The OH⁻ ions from NaOH are all immediately available to participate in the hydrolysis reaction, as NaOH is a strong base, leading to a fast precipitation of zinc hydroxide. On the other hand, the OH⁻ ions from NH₄OH are not all immediately available as this base is much weaker than NaOH and the release of OH⁻ is much slower and consequently leading to a slower growth of zinc hydroxide, yielding smaller nanocrystals. Another possibility is related towards the steric hindrance that the cations provide within the already confined hydrophilic sub-phases within the PEM, in which the crystal growth occurs. Since NH₄⁺ ions are much larger than Na⁺ ions, it might be possible that the bulky NH₄⁺ ions are providing an unfavorable steric hindrance towards the growth of the nanocrystal, forcing the crystal growth to halt due to an unfavorable environment caused by the electrostatics of the surrounding ammonium ions, yielding smaller nanocrystals.

In Figure 4-5 UV-Vis spectra shows that the onset of absorption for Nafion-ZnO treated with NaOH is at about 370 nm, whereas for Nafion-ZnO treated with NH_4OH has an absorption onset at about 350 nm. The acid form of Nafion has essentially no absorption. Based on the model developed by Pesika, et. Al.¹⁰² the average particle size of ZnO is about 10 nm when treated with NaOH and about 4 nm when treated NH_4OH . These results are in agreement with particle size distributions obtained from TEM images, noting that for NaOH treated sample, the model underestimates the average particle size by about 5 nm. Therefore, it has been demonstrated that by treating the membranes with a weaker base (NH_4OH) in the hydrolyzing step of the in-situ synthesis protocol, one can achieve smaller nanoparticles. Further studies will include the extent at which particle size distribution can be controlled by using a variety of bases and solvents.

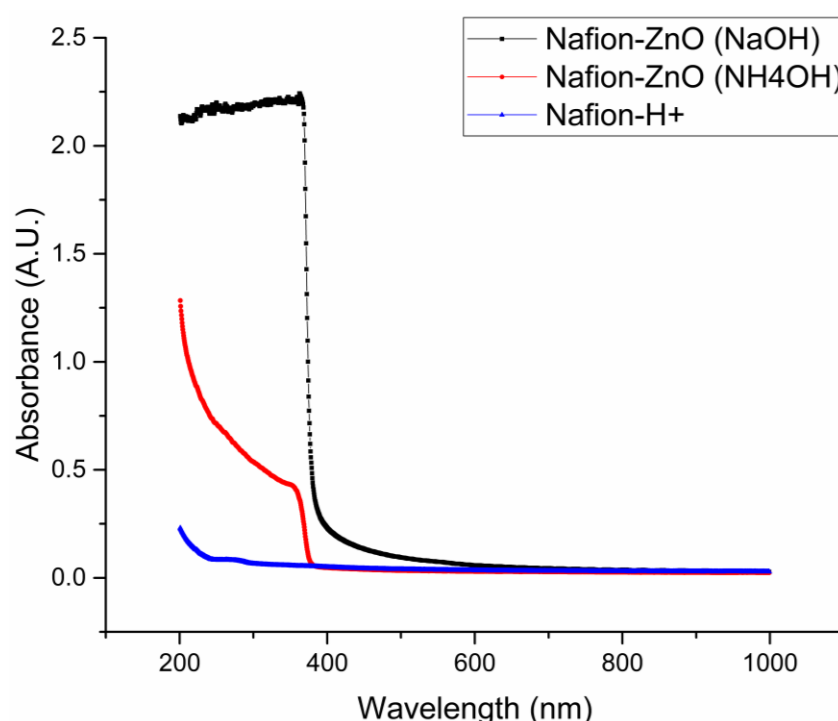


Figure 4-5. UV-Vis spectra of Nafion-ZnO treated with NaOH (black), Nafion-ZnO treated with NH_4OH (red), and Nafion in acid form (blue).

4.3 Manipulation of *in-situ* Grown ZnO Morphology within PEM

An attempt to control the morphology of MONP within PEM was done by changing the solvent at which the *in-situ* synthesis is done such that the membrane would swell at different degrees causing the hydrophilic domains within the PEM micro-structure to change yielding MONP of different sizes and shapes.

Crystallographic analysis of ZnO was performed by looking into the relative distribution between the {002} plane and the {100} surface facets of the Wurzite structure of the hexagonal-packed ZnO from XRD experiments. The main features displayed in the pattern are the three prominent peaks located at $2\theta \approx 31.7^\circ$, 34.4° and 36.2° , representing the three most thermodynamically stable crystallographic planes of the Wurzite structure (corresponding to the {101}, {002} and {100} planes, respectively), Figure 4-6. The integrated peak areas indicate that under aqueous conditions, the most prominent plane is the {100} plane, accounting for 45% of the total area among the three primary peaks. The integrated peak areas for the {101} and {002} planes meanwhile each represent approximately 27% and is indicative of the presence of zinc oxide nanorod seeds, defined by particles that have the {100} facet predominantly exposed, but has not reached the proper aspect ratio that would define a rod-like structure.

Binary mixtures of water and 4 different alcohols (methanol, ethanol, 1-propanol and 2-propanol) were chosen at 4 different concentrations in order to study the interplay between the swelling behavior of the host polymer and the growth dynamics of the inorganic phase. It was observed that during the *in-situ* growth there was a monotonic increase of swelling with the alcohol content and that swelling is more pronounced for less polar alcohols. This is attributed to the fact that binary mixtures of alcohol and water results

in a greater uptake than their pure components and that the enhanced swelling arises from the preferential solvation of the membrane backbone by the alcohol. XRD patterns and fitted peak areas for each condition are displayed in Figure 4-6. XRD analysis reveals that with the inclusion of any of the 4 alcohols, the peak representing the {101} plane of zinc oxide is no longer the most prominent but instead becomes subsidiary to the peak representing the {002} crystal plane. The insets for Figure 4-6 show the evolution of the fitted peaks for each condition. With increasing alcohol content there is a non-monotonic increase in the {002} plane that exceeds the growth of both the {101} and {100} planes, which corresponds to the formation of zinc oxide nanoplatelets. Interestingly, when zinc oxide is synthesized in the bulk solution (i.e. without the membrane) the integrated peak areas conform back to the ratio ascribed to the formation of zinc oxide without the presence of alcohol (i.e. the most prominent plane is the {101}). Changes in the hydrophilic domain structure may explain the preferred growth of the {002} plane of zinc oxide in alcoholic solutions. Within a given domain, the concentration and proximity of the sulfonated groups are assumed to be fixed.

Similar work was performed on Nexar membranes to observe how the environmental changes impact the growth of MONP within PEM. Sorption of organic solvents within Nexar membranes has a significant impact in the size of its hydrophilic subphases given that these less polar solvents have a preference to interact with the more hydrophobic hydrocarbon backbone of Nexar. Alcohol sorption has been studied, particularly for pervaporation applications, and it has been shown that within C2 to C4 alcohols the smaller the carbon chain on the alcohol, higher solvent sorption and swelling occur within Nexar

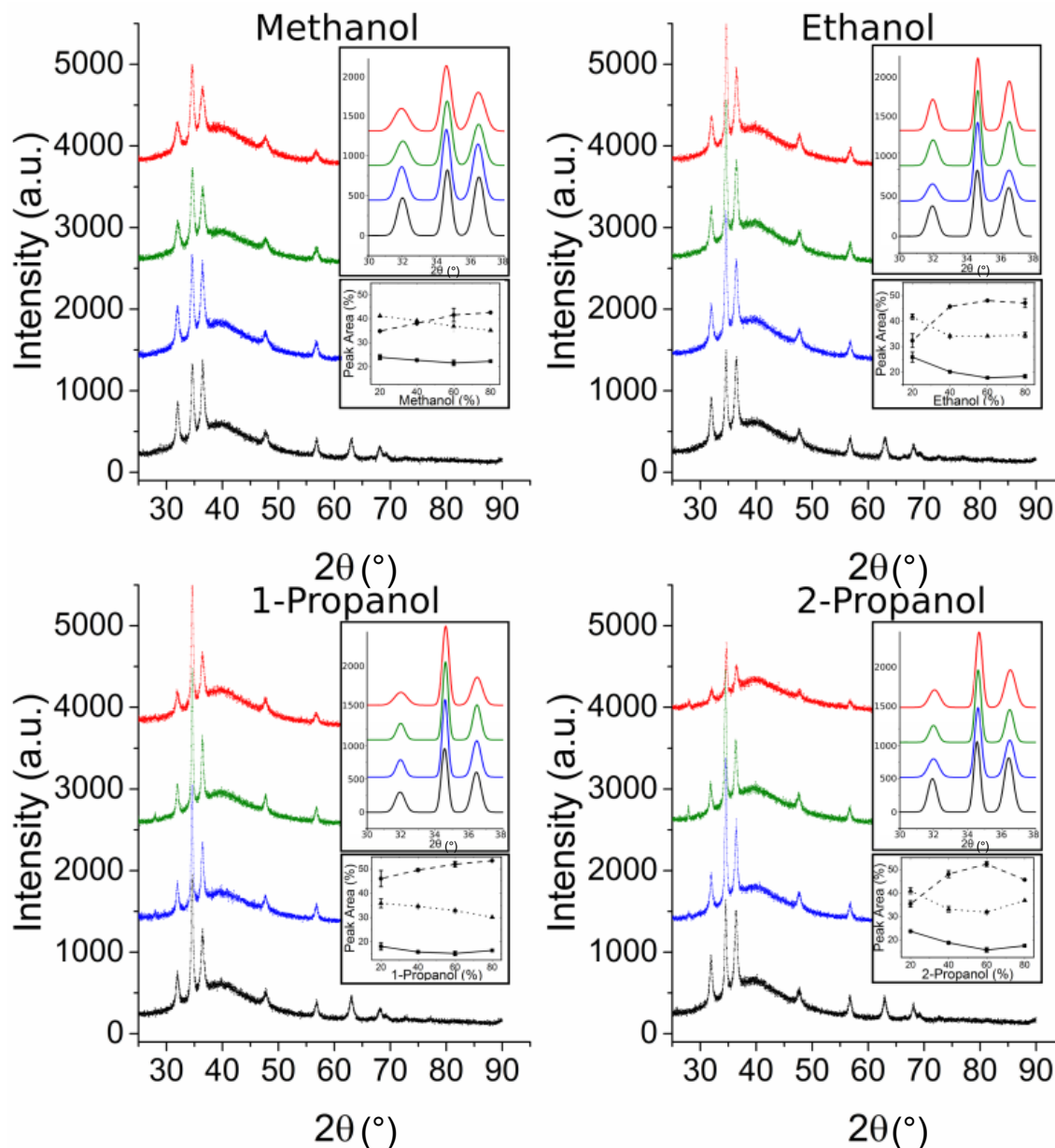


Figure 4-6. Wide-angle x-ray diffraction for zinc oxide – Nafion composites prepared with different binary solvent mixtures. The percent of alcohol in the binary mixtures are 20% (black), 40% (blue) 60% (green) and 80% (red). Top inset includes the fitted data for for the low index planes corresponding to composites prepared at different concentrations of alcohol. Y-axis displays the intensity and is in a.u. The bottom inset plots the evolution of the three primary surface planes as a function of alcohol content. The lines correspond to the following planes: solid line – {100}, dashed line – {002} and dotted line – {101}.

substrates.¹⁰³⁻¹⁰⁴ Given that alcohol sorption affects the hydrophilic subphase of Nexar, it can be one factor that can be used to manipulate the *in-situ* ZnO crystal growth. Figure 4-7(a) shows raw XRD data corresponding to the (100), (002), and (101) crystallographic planes. Raw XRD data was fitted by Gaussian curves and areas under the curves (AUC) were calculated.

Figure 4-7(b) shows the fitted peaks of the hexagonal-lattice XRD of Nexar-ZnO treated in different amounts of methanol/water and its impact on the ZnO growth within the substrates. It can be seen that with increasing amounts of methanol, less intense are the three main peaks of hexagonal-lattice ZnO until no ZnO is observed within Nexar membranes at 80 % (v/v) methanol/water. In addition, the ratio of the AUC for (002)/(100) peaks decreases as methanol content increases, suggesting that the presence of methanol favors the growth of aggregates resembling needle-shape structures rather than platelet-like aggregates. Crystallographic plane (002) seems to be particularly affected as its relative peak area has a negative correlation with increasing amounts of methanol, as it can be seen more clearly in the (002)/(100) relative peak area ratio. Moreover, the average ZnO aggregate size is also affected. Figure 8 (shows how the average

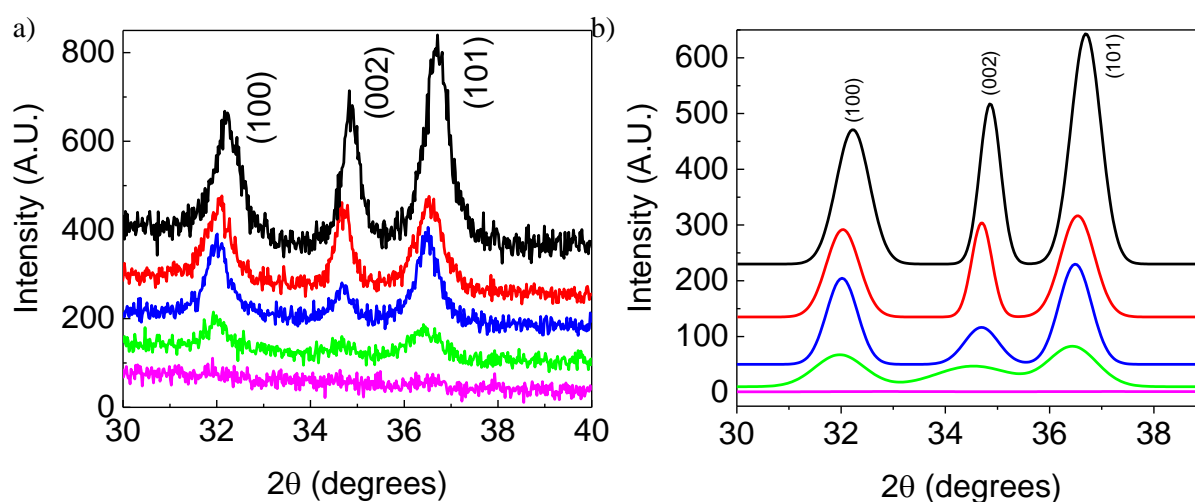


Figure 4-7. (a) Raw XRD diffractograms of Nexar-ZnO with varying amount of binary solvent/water composition: (black) control Nexar-ZnO, (red) 20 % (v/v) MeOH, (blue) 40 % (v/v) MeOH, (green) 60 % (v/v) MeOH, (magenta) 80 % (v/v) MeOH (b) Fitted XRD diffractograms of Nexar-ZnO with varying amount of binary solvent/water composition: (black) control Nexar-ZnO, (red) 20 % (v/v) MeOH, (blue) 40 % (v/v) MeOH, (green) 60 % (v/v) MeOH, (magenta) 80 % (v/v) MeOH.

aggregate size of ZnO within Nexar, 60 nm, decreases by a factor of 2 by increasing the methanol content to 60 % (v/v) while growing ZnO, demonstrating the ability to control the average size of

ZnO nanoaggregates. No ZnO was observed for samples immersed in 80 % (v/v) methanol solutions.

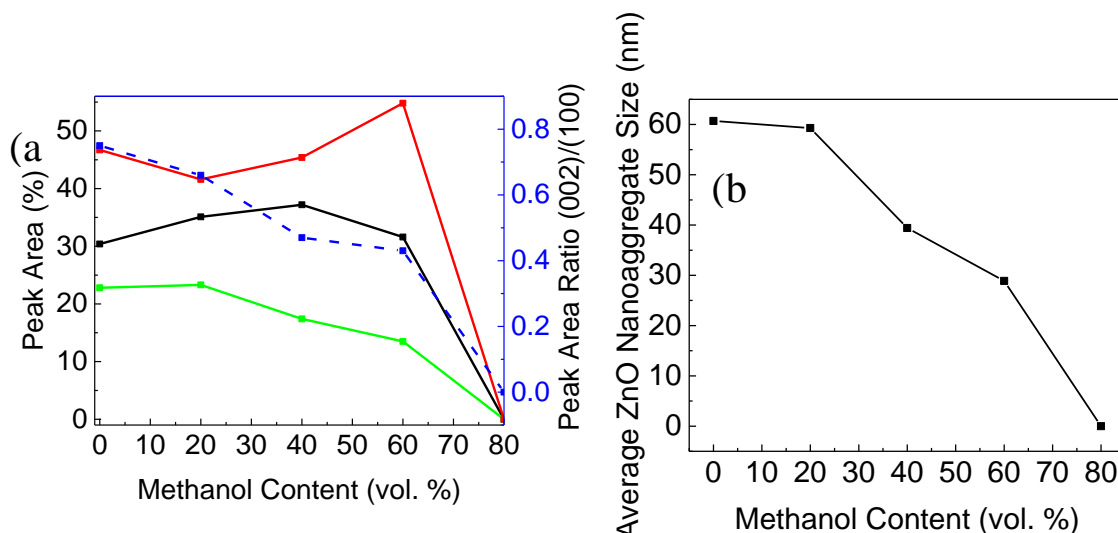


Figure 4-8. (a) Evolution of the relative peak area of the three main ZnO crystallographic planes as a function of methanol content in solvent: (black) (100), (green) (002), (red) (101) and (blue) the (002)/(100) peak area ratio. (b) Average ZnO nanoaggregate size as a function of methanol content in solvent.

For Nafion membranes, the use of less polar alcohols resulted in a tendency to form larger zinc oxide particles exacerbated by higher alcohol contents. This increase in particle size is accompanied by a decrease in intensities for the higher index peaks (i.e. corners and edges) that appear in the XRD pattern. By comparing relative peak intensities for all peaks, it can be observed that the use of higher homologous alcohols led to a decrease in total intensities for the higher index planes. For example, the higher index peaks amounted to over 30% of the total peak intensity for all concentrations of methanol. This is contrary to the case of 2-propanol where the accumulated peak intensity amounted to 20% of the total. Thus it could be envisioned that although the {002} plane is more catalytically active in certain scenarios over the {101} plane, it comes at the consumption of highly active corners and edges. However, for Nexar membranes, the opposite result occurs. As there is an increase in the organic solvent, methanol, the {002} plane becomes less prominent to the extent of no growth of ZnO when using 80 % (v/v) of methanol solutions.

CHAPTER 5. Hydrolytic Decomposition of CWA and Simulants

This chapter is based on work that has been published to the references shown below:

- J. Colón-Ortiz, et. Al., Disordered Mesoporous Zirconium (Hydr)Oxides for Decomposition of Dimethyl Chloro-Phosphate. “Just Accepted” at Applied Materials and Interfaces.

5.1 Surface Modification on MONP to Improve Reactivity against CWA and Simulants

Modification of metal-oxide surfaces have been performed in order to improve their catalytic capabilities by introducing surface defects, such as oxygen vacancies and mixed-metal valencies.¹⁰⁵⁻¹⁰⁶ Warm hydrogen peroxide solutions have been used to induce surface defects, such as oxygen vacancies, within metal oxides in order to increase their reactivity.¹⁰⁷ One consequence of using hydrogen peroxide on metal oxides is that, in addition to surface chemistry alterations, there are also physical changes within the oxides. Some examples of the physical changes, discussed herein, are the increased surface area to volume ratio and the transformation of crystalline phases into amorphous phases. A significant increase of the surface area comes from the formation of mesopores that enhances the catalytic efficiency. Nitrogen adsorption experiments, Figure 5-1(a), indicate that there is formation of mesopores during H_2O_2 treatment on the $\text{ZrO}_2/\text{Zr}(\text{OH})_4$ samples as there is increased adsorption of nitrogen and the presence of a hysteresis loop on H_2O_2 treated $\text{ZrO}_2/\text{Zr}(\text{OH})_4$. A non-local density functional theory (NLDFT) model was used to deconvolute the pore size distributions of untreated and H_2O_2 treated zirconium (hydr)oxides based on the adsorption branch, Figure 5-1(b). The NLDFT model estimates

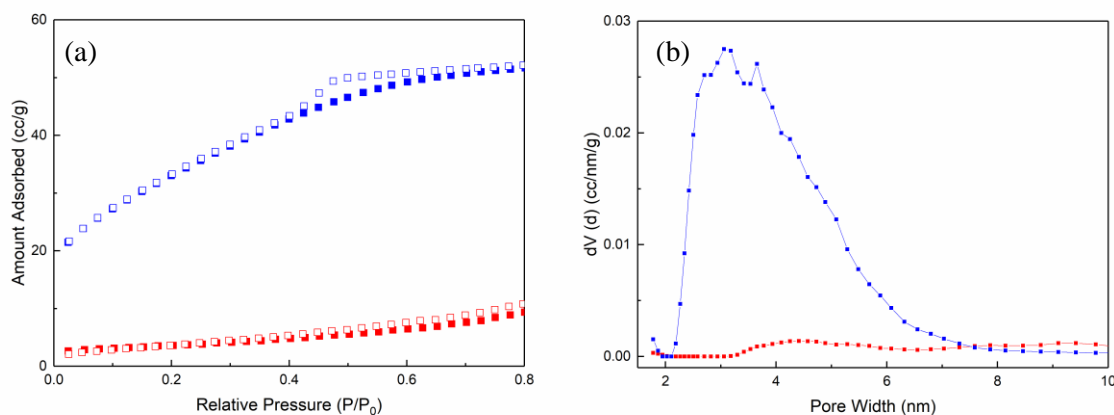


Figure 5-1. (a) Nitrogen adsorption isotherms for $\text{ZrO}_2/\text{Zr}(\text{OH})_4$ (untreated – red, H_2O_2 treated – blue). Solid squares are adsorption points and open squares are desorption points. (b) Pore size distributions based on NLDFT model (untreated – red, H_2O_2 treated – blue).

that the average pore size for H_2O_2 treated $\text{ZrO}_2/\text{Zr}(\text{OH})_4$ is around 3.1 nm, while the untreated $\text{ZrO}_2/\text{Zr}(\text{OH})_4$ remain essentially non-porous. In addition, the untreated $\text{ZrO}_2/\text{Zr}(\text{OH})_4$ exhibit a surface area of $12.4 \text{ m}^2/\text{g}$ while the H_2O_2 treated $\text{ZrO}_2/\text{Zr}(\text{OH})_4$ have an order of magnitude increase in surface area of $101.8 \text{ m}^2/\text{g}$. Similar results were obtained for cerium (hydr)oxides prepared in the same manner, but not for zinc (hydr)oxides (see Figure 5-2). H_2O_2 has minimal effect on the formation of mesopores within zinc (hydr)oxides. This may be due to its single valence state that may not allow for a density of oxygen vacancies high enough to disrupt its crystalline structure.

X-ray photoelectron spectroscopy (XPS) was used to measure the chemical surface modifications that arise from the hydrogen peroxide treatment. The core energy level spectra of O 1s and Zr 3d are collected in Figure 5-3. For the untreated $\text{ZrO}_2/\text{Zr}(\text{OH})_4$, the position and shape of the peaks related to Zr 3d are representative for the oxidation state, +4.¹⁰⁸ shown in Figure 5-3(a), in which both the Zr $3d_{3/2}$ and Zr $3d_{5/2}$ are located at 181.2 and 183.8 eV, respectively.¹⁰⁹ Of the four components on the O 1s spectrum, Figure 5-3(b), the first two peaks located at binding energies of 529.1 and 530.8 eV are assigned to the lattice Zr–O bonds and surface chemisorbed oxygen, respectively.^{108, 110-111}

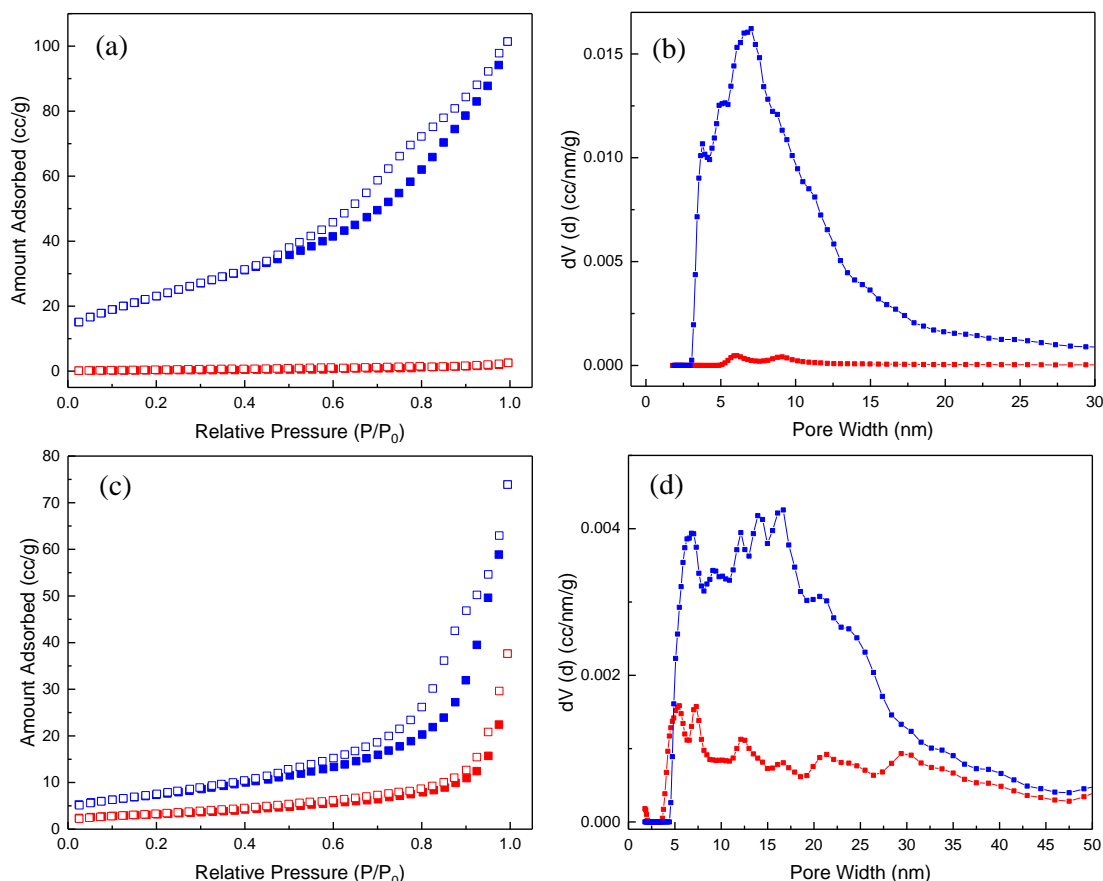


Figure 5-2. (a) Adsorption Isotherms for untreated CeO₂ (red) and H₂O₂ treated CeO₂ (blue). (b) Pore size distribution of untreated CeO₂ (red) and H₂O₂ treated CeO₂ (blue) based on a NLDFT model. (c) Adsorption Isotherms for untreated ZnO (red) and H₂O₂ treated ZnO (blue). (d) Pore size distribution of untreated ZnO (red) and H₂O₂ treated ZnO (blue) based on a NLDFT model.

These surface chemisorbed species arise from the presence of O⁻, O₂⁻, and O²⁻, which have been associated with the formation of surface oxygen vacancies.¹¹¹ It has been shown that the presence of oxygen vacancies within the surface of metal-oxides has proven to enhance the decomposition of CWA.^{105-106, 111} The reactive oxygen vacancies present within the zirconium (hydr)oxides as seen from our XPS studies in Figure 5-3(b,d) may have an important role in the decomposition of DMCP. However, isolating the effect of oxygen vacancies against the decomposition of DMCP were outside the scope of this study. The lower intensity peaks at 532.7 and 536.1 eV can be linked to the presence of the hydroxyl

groups bonded to zirconium and the presence of humidity or surface bound water, respectively.¹¹²

Although there is evidence of mixed valence states in H_2O_2 -treated metal oxides¹⁰⁶

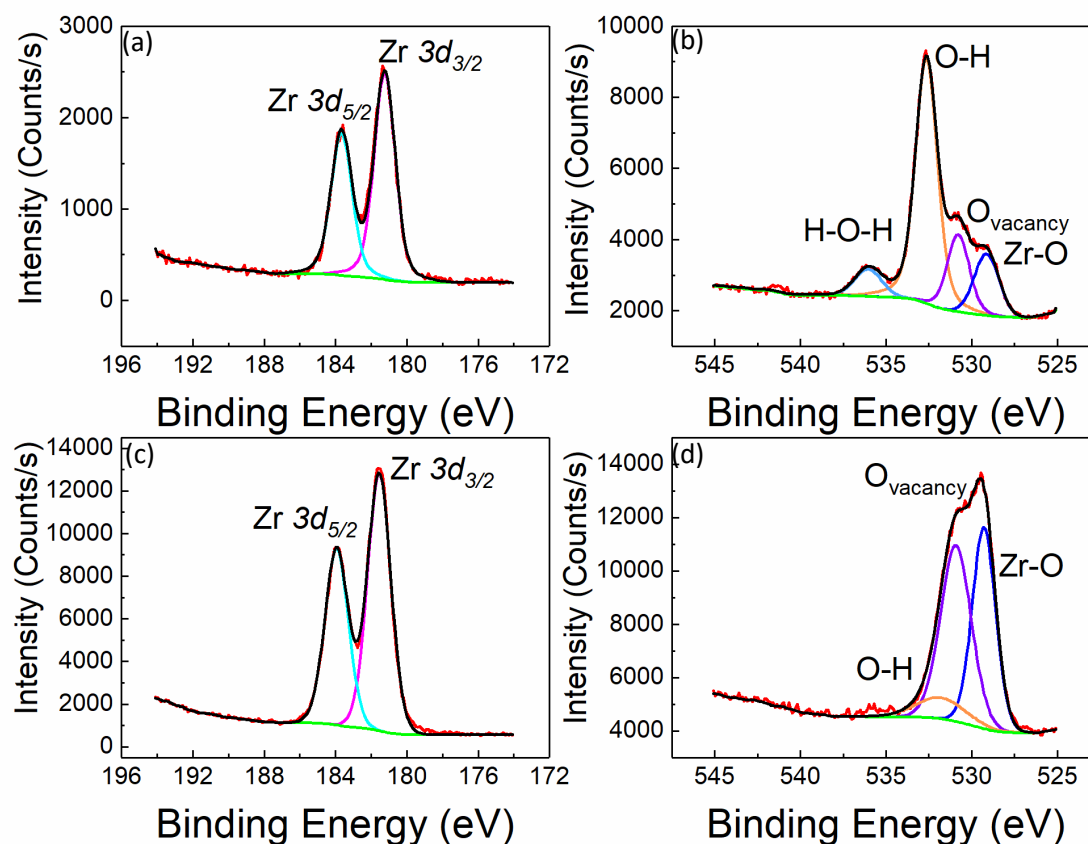


Figure 5-3. (a) Zr 3d core level spectrum of untreated $\text{ZrO}_2/\text{Zr(OH)}_4$ (b) O 1s core level spectrum of untreated $\text{ZrO}_2/\text{Zr(OH)}_4$ (c) Zr 3d core level spectrum of H_2O_2 treated $\text{ZrO}_2/\text{Zr(OH)}_4$ (d) O 1s core level spectrum of H_2O_2 treated $\text{ZrO}_2/\text{Zr(OH)}_4$.

in our case there was no apparent change in the oxidation state of zirconium during the H_2O_2 treatment, Figure 5-3(c). In addition, it can be seen in Figure 5-3(d) that the surface bound water molecules mostly disappear and the surface hydroxyls are significantly reduced when compared to the untreated $\text{ZrO}_2/\text{Zr(OH)}_4$. This reduction in O-H and H_2O species from the sample after H_2O_2 treatment has been observed theoretically¹¹³ as H_2O_2 molecules interact with O-H and H_2O species adsorbed on the surface of the sample by being cleaved and forming highly reactive H–O radicals that later react with other adsorbed

species producing water molecules that leave the oxide surface. However, treated and untreated samples contain hydroxyl groups. Therefore, we refer to treated and untreated samples as (hydr)oxides as both, oxide and hydroxide, phases coexist between both samples. The untreated sample, which is predominantly Zr(OH)_4 , is composed of approximately of 25.4 at.% ZrO_2 and the H_2O_2 -treated sample, which is predominantly ZrO_2 , is composed of approximately of 22.2 at.% Zr(OH)_4 based on the Zr–O and O–H components in the O 1s peaks at 529.1 and 532.7 eV, respectively in Figure 5-3(b,d).

The morphological structures of the $\text{ZrO}_2/\text{Zr(OH)}_4$ were studied by Transmission Electron Microscopy (TEM) and X-ray diffraction (XRD). The TEM images, Figure 5-4, show that nanoaggregates within 25-200 nm are densely supported on micron-sized thin flakes for both untreated and H_2O_2 -treated samples. The H_2O_2 treatment appears to have an insignificant effect on the particle size distribution of the zirconium (hydr)oxides, although there is more abundance of large thin flakes on the treated samples.

In Figure 5-5 it can be seen that parental samples of $\text{ZrO}_2/\text{Zr(OH)}_4$ prior to H_2O_2 treatment exhibit the crystalline features that are found within cubic-lattice ZrO_2 , less intense but sharp peaks of Zr(OH)_4 and impurities that come from the precursors used to synthesize the $\text{ZrO}_2/\text{Zr(OH)}_4$, in this case NaNO_3 . However, after the treatment, the cubic-lattice features disappear and the treated sample appears to be rather amorphous, suggesting that the H_2O_2 treatment vigorously transforms the crystallinity of the material.

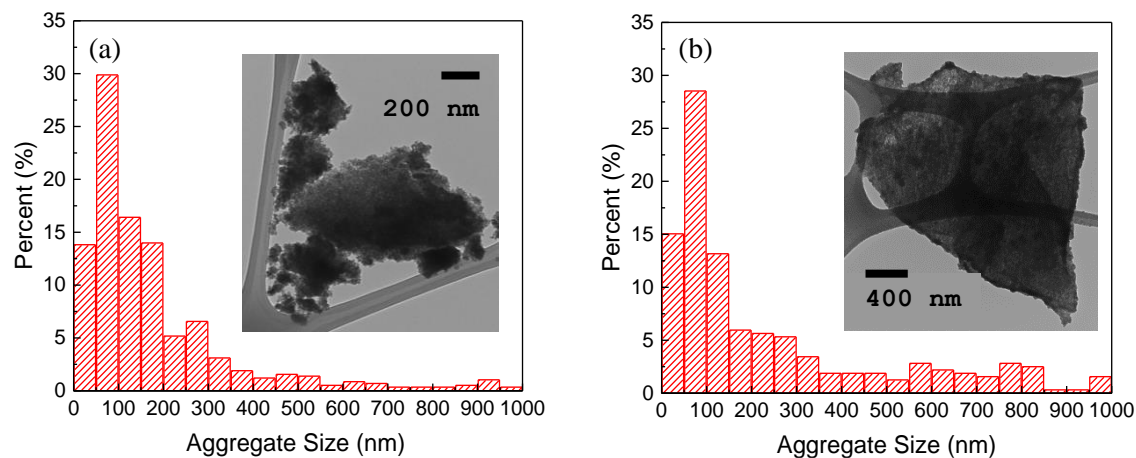


Figure 5-4. (a) Aggregate size distributions of untreated $\text{ZrO}_2/\text{Zr(OH)}_4$, inset – TEM micrograph of untreated $\text{ZrO}_2/\text{Zr(OH)}_4$. (b). Aggregate size distributions of H_2O_2 -treated $\text{ZrO}_2/\text{Zr(OH)}_4$, inset – TEM micrograph of H_2O_2 treated $\text{ZrO}_2/\text{Zr(OH)}_4$.

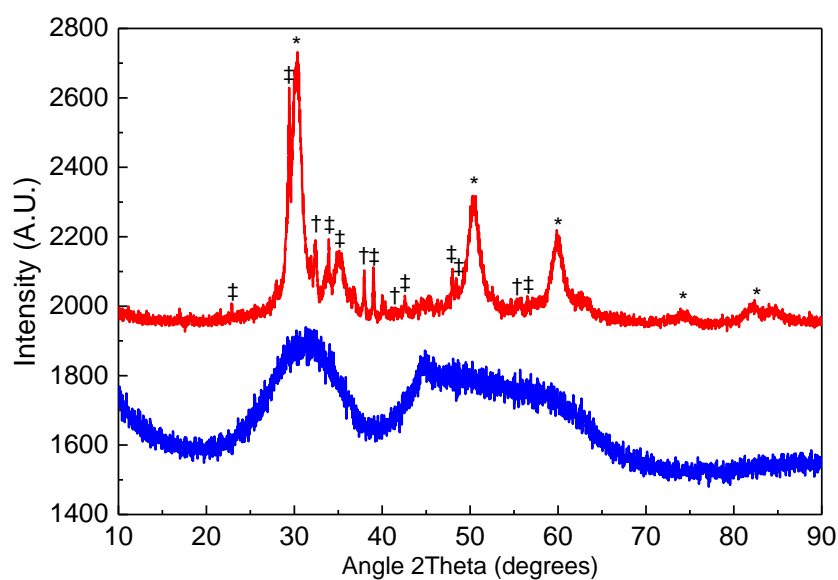


Figure 5-5. X-ray diffractogram of untreated $\text{ZrO}_2/\text{Zr(OH)}_4$ (red) and H_2O_2 treated $\text{ZrO}_2/\text{Zr(OH)}_4$ (blue). Symbols above peaks represent phases of: (*) ZrO_2 , (†) Zr(OH)_4 , (‡) NaNO_3 .

5.2 CWA Simulant Reactivity against Surface-Modified $\text{ZrO}_2/\text{Zr}(\text{OH})_4$

DRIFTS measurements were performed to assess the reactivity differences between the H_2O_2 treated and untreated $\text{ZrO}_2/\text{Zr}(\text{OH})_4$ samples. Time-resolved difference spectra are reported herein, with the initial (black) and final (brick red) in order to identify spectral changes with respect to the native material. Peak assignments were made based on DFT calculations of DMCP and corroborated with literature assignments for 1) DMCP in the gas phase,¹¹⁴ 2) on previously reported solid substrates,¹¹⁵ 3) DMCP adsorbed onto silica¹¹⁴ and 4) DMMP on $\text{Zr}(\text{OH})_4$.¹¹⁶

Characteristic spectral features are observed between the H_2O_2 treated and untreated $\text{ZrO}_2/\text{Zr}(\text{OH})_4$. The decomposition of organophosphorus agents on metal (hydr)-oxides have been reported through a two-step mechanism of first bonding of the phosphorus moiety followed by hydrolysis to form dimethyl phosphonate (DMHP) followed by methanolysis to form methyl methylphosphonate and methanol.¹¹⁷ However,

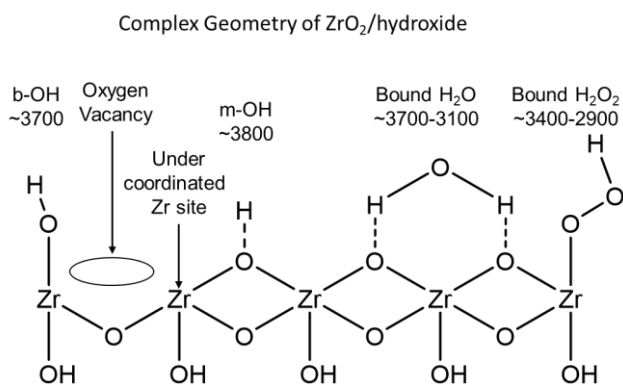


Figure 5-6. Different reactive sites and hydroxyl groups present on the $\text{ZrO}_2/\text{Zr}(\text{OH})_4$ structure.

a close inspection of our spectral data indicates the picture to be more complex. The structure of $\text{ZrO}_2/\text{Zr}(\text{OH})_4$ is known to consist of a complex array of reactive moieties ranging from various adsorbed hydroxyl species (monodentate, bidentate) peroxide species, water and Lewis acid sites such as oxygen vacancies as shown in Figure 5-6.

It is generally agreed upon that the primary adsorption pathway of organophosphorus agents will occur through the P=O moiety on metal oxides.¹¹⁸ Within our investigation, it was revealed that several reaction pathways are likely to occur. For instance, upon DMCP adsorption to the H₂O₂-treated sample, there is an observed increase in the P=O at 1256 cm⁻¹ stretching mode with a decrease in a mode at 1288 cm⁻¹ that follows, as shown in Figure 5-7.

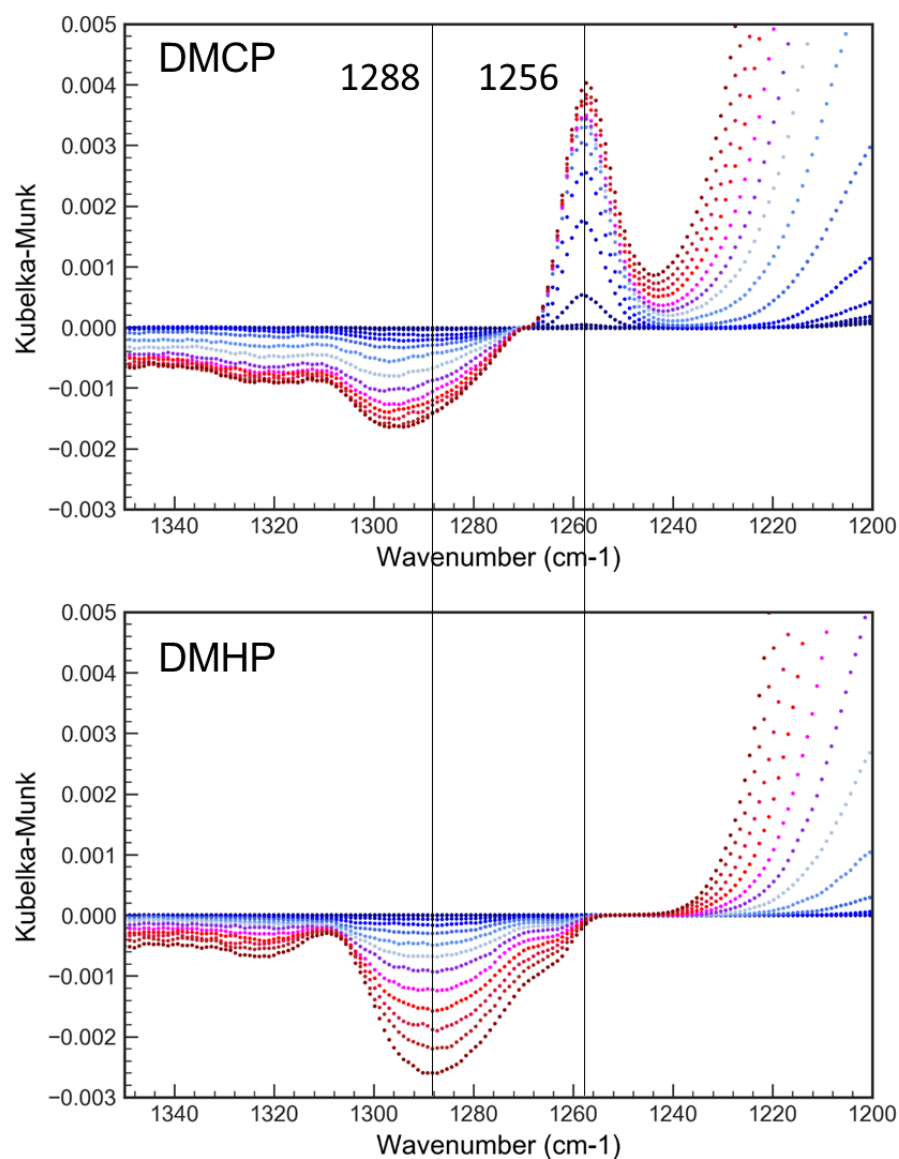


Figure 5-7. Closer examination of the P=O mode occurring at 1256 cm⁻¹ for defect DMCP (top) and occurring at 1288 cm⁻¹ for DMHP (bottom) for the H₂O₂-treated ZrO₂/Zr(OH)₄.

Examining the results of DMHP adsorption we see that the P=O mode at 1256 cm^{-1} of DMCP is no longer present, but a greater decrease in the 1288 cm^{-1} mode is observed, as shown in Figure 5-8.

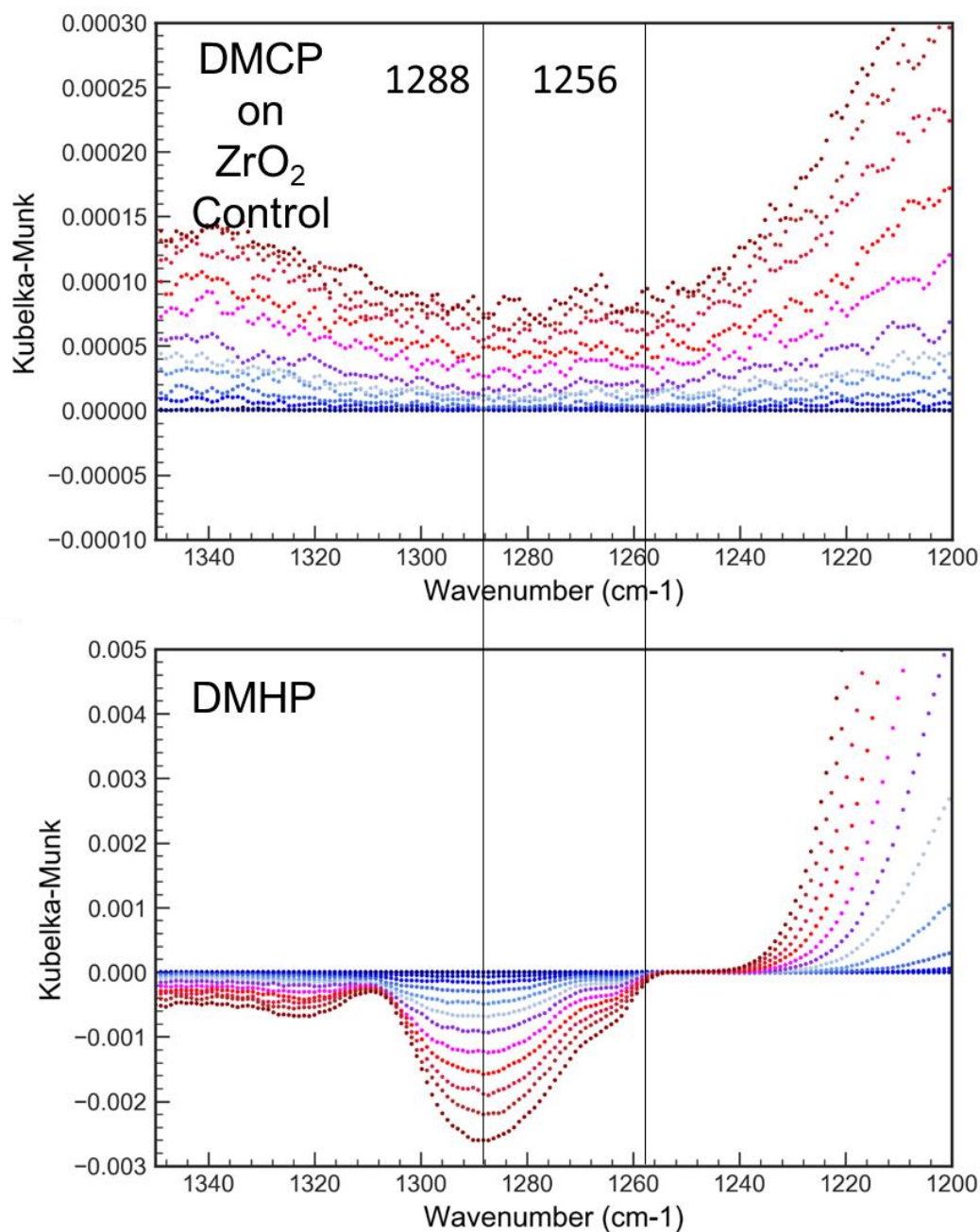


Figure 5-8. Closer examination of the P=O mode occurring at 1256 cm^{-1} for DMCP (top) and occurring at 1288 cm^{-1} for DMHP (bottom) for the untreated ZrO₂/Zr(OH)₄.

This broad peak is likely a convolution of several surface modes that obscures the DMHP P=O mode. Nevertheless these results would imply the conversion of DMCP to DMHP on the H_2O_2 -treated sample, and the rapid loss of the P=O mode in DMHP upon adsorption. This is in contrast to the control sample where the P=O mode related to DMHP is not observed. This indicates that the H_2O_2 -treated sample allows for an additional reaction pathway that is absent in the control as shown in Figure 5-9.

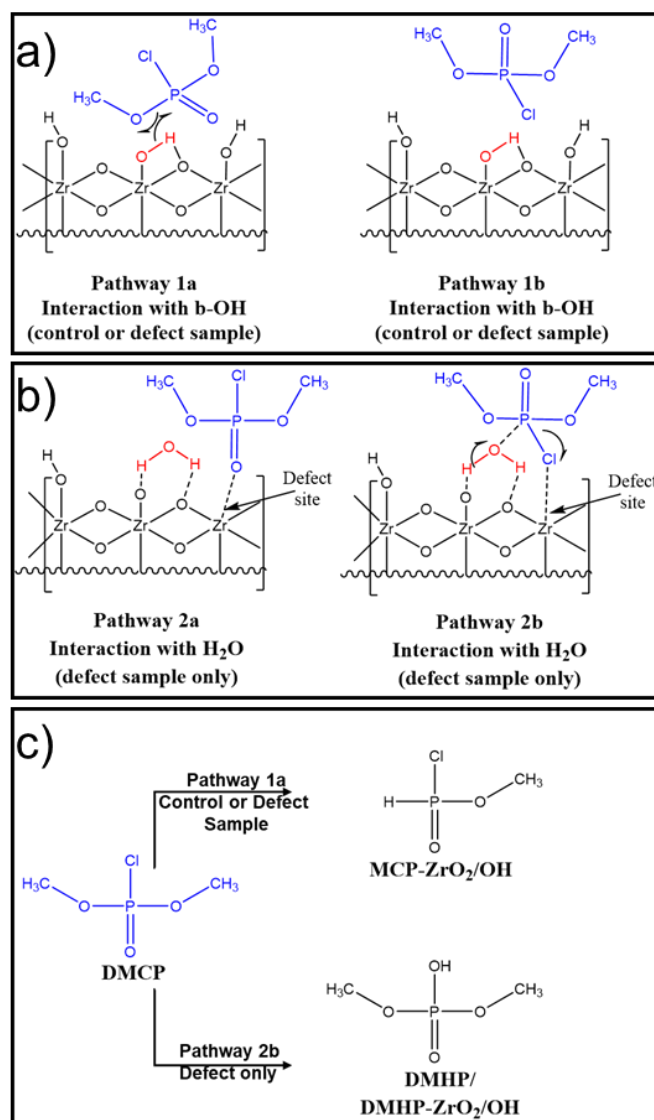


Figure 5-9. a) Plausible reaction pathways involving b-OH groups affecting both the control and defective sample. b) Plausible reaction pathways involving water which only affects the defective sample. Red indicates reactive surface bound species. c) The two pathways concluded here.

Several reaction pathways are plausible based on how DMCP approaches the surface, either through P=O approach (A) or Cl approach (B). For both the control and H₂O₂-treated sample, DMCP likely undergoes **Pathway 1a**, whereby only bidentate (bridged) hydroxyls are consumed (see Figure 5-12 for the high wavenumber region). This results in the hydrolytic decomposition through the loss of a methoxy group (CH₃O) which can be observed in the low wavenumber region (see Figure 5-10). **Pathway 2b** demonstrates a hydrolytic mechanism of DMCP with the reaction of tightly bound water along with cleavage of the chlorine group to form DMHP, respectively. While **Pathways 1b** and **2a** may be plausible, we do not see any spectral evidence through the formation of DMHP in the former. Additionally, while we cannot rule out the cleavage of the chlorine atom, detecting the chlorine surface mode that occurs below 1000 cm⁻¹ is below the detection limit.

DMCP binding peaks can be inferred from the low wavenumber region from 1400-900 cm⁻¹. Several regions are observed that correspond to binding of the DMCP molecule and possible products. For the H₂O₂ treated sample (Figure 5-10), we observe peaks at 1175 cm⁻¹ and 1144 cm⁻¹ with the former representing the $\nu_a(\text{O-P-O})$ mode and the latter the dissociative methoxy bound to a zirconium atom and possibly an additional $\nu(\text{P-O}_x)$ mode.¹¹⁶ Plotting the peak heights of the two largest modes in this region (1175 cm⁻¹ and 1144 cm⁻¹) as a function of time (inset of Figure 5-10), it can be observed that there is a lag phase that occurs for the first 30 min, which is the amount of time for the DMCP vapor to diffuse through the packed bed. After 30 min, there is a linear increase in both peaks, which suggests first order kinetics, the height increases for both peaks appear to be the same as in the untreated sample, Figure 5-11, but with significantly less intensity. Meanwhile, a third

peak associated with the $\nu_s(\text{O-P-O})$ mode can also be observed at lower wavelengths of 1080 cm^{-1} which is known to occur approximately 100 cm^{-1} lower than the higher energetic asymmetric peak.¹¹⁹ All three peaks represent possible products and are corroborated by the fact that they do not appear in the DFT calculated spectra nor in the gas phase of DMCP. The peak centered at 1030 cm^{-1} is associated with the $\nu(\text{C-O})$ mode of DMCP. Peaks related to the P=O stretching liquid/multi-layer mode of DMCP can be observed at 1256 cm^{-1} and is supported by our DFT calculations. Interfacial carbonate complexes were also found on the surface residing in the region of $1700\text{-}1300\text{ cm}^{-1}$ which are eventually displaced with exposure to DMCP.

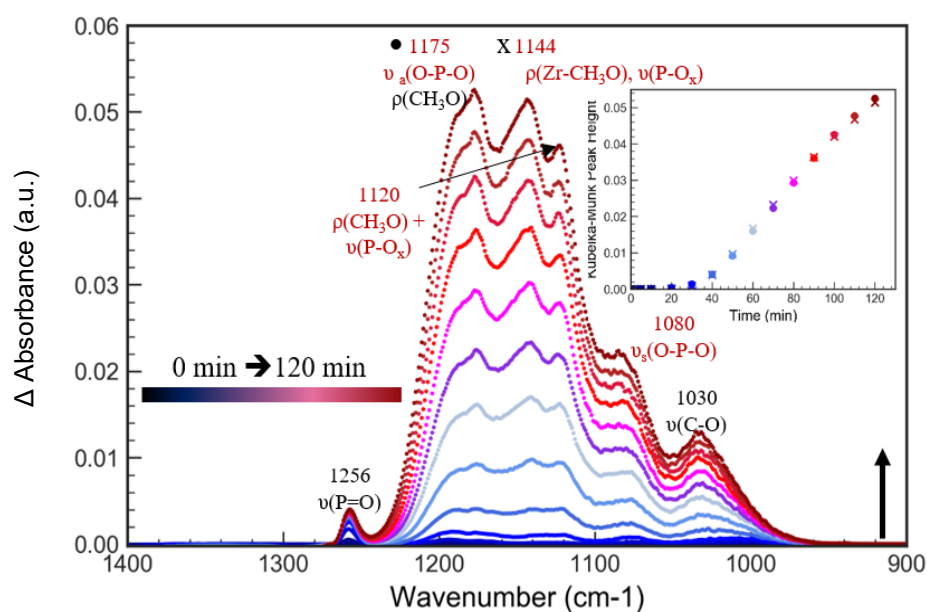


Figure 5-10. Low wavenumber region of DMCP on H_2O_2 -treated $\text{ZrO}_2/\text{Zr}(\text{OH})_4$ between 1400-900 wavenumbers. Inset: Peak height as a function of time. O = 1177, X = 1144 cm^{-1} . A lag phase occurs for the first 30 minutes, after which a linear increase in products could be observed. Modes in red represent those attributed to decomposition product. Time intervals between spectra are: 0, 2, 5, 10, 20, 30, 40, 50, 60, 70, 80, 90, 100, 110, 120 min

The untreated $\text{ZrO}_2/\text{Zr}(\text{OH})_4$ sample demonstrates two orders of magnitude decrease in the observed signal compared to the H_2O_2 -treated sample, which may be a qualitative indicator for the lower adsorption of DMCP, Figure 5-11. It should be noted that for the H_2O_2 -treated sample, the dominant peak is the asymmetric (O-P-O) mode while for the untreated sample

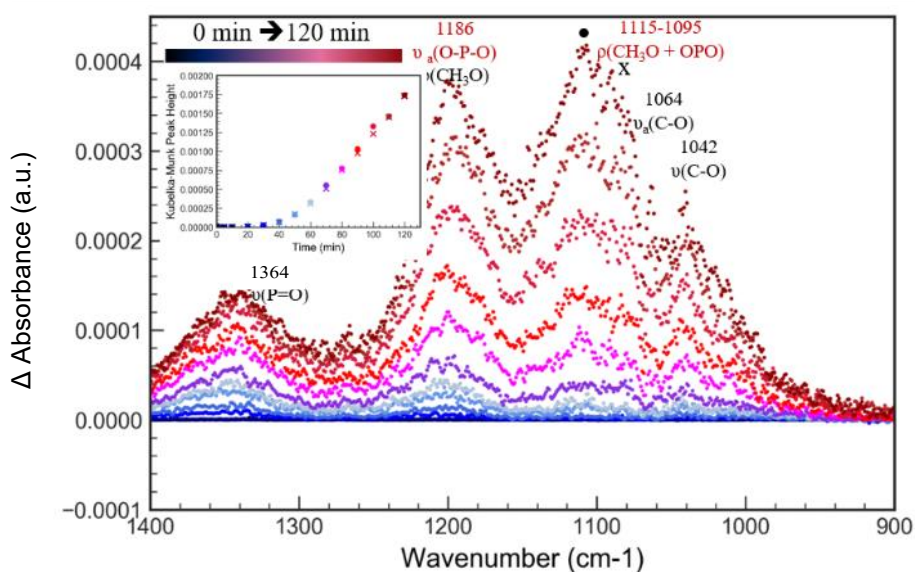


Figure 5-11. Low wavenumber region of DMCP on untreated $\text{ZrO}_2/\text{Zr}(\text{OH})_4$ between 1400-900 wavenumbers. Inset: Peak height as a function of time. O = 1115, X = 1095 cm^{-1} . Modes in red represent those attributed to decomposition product. Time intervals between spectra are: 0, 2, 5, 10, 20, 30, 40, 50, 60, 70, 80, 90, 100, 110, 120 min.

it is the lower energetic symmetric stretch. Peaks could not be observed below 900 cm^{-1} for both materials, as metal oxides strongly absorb in this region

The contrast between the two samples is more apparent at higher wave numbers in the region between 4000-2700 cm^{-1} (Figure 5-12). Upon exposure to DMCP, there is a decrease for the H_2O_2 -treated sample in the amount of free bi-dentate hydroxyl groups on the surface, occurring at 3700 cm^{-1} and 3628 cm^{-1} , respectively, indicating the decomposition of DMCP upon contact with the surface.

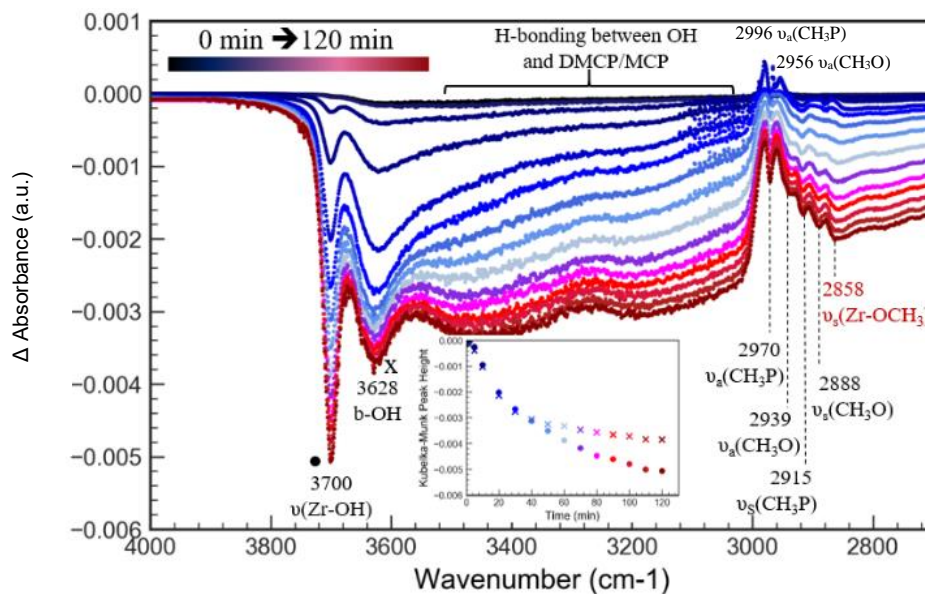


Figure 5-12. High wavenumber region of DMCP on H_2O_2 -treated $\text{ZrO}_2/\text{Zr}(\text{OH})_4$. $\text{O} = 3700$, $\text{X} = 3628 \text{ cm}^{-1}$. Modes in red represent those attributed to decomposition product. Time intervals between spectra are: 0, 2, 5, 10, 20, 30, 40, 50, 60, 70, 80, 90, 100, 110, 120 min.

The inset of Figure 5-12 plots the decrease of bridged hydroxyls (b-OH) and tightly bound water modes at 3700 cm^{-1} and 3628 cm^{-1} , respectively, the rate of which suggest first order kinetics. Meanwhile, there is also a reduction in the region that is attributed to the hydrogen bonding between the hydroxyls and DMCP in the range of $3550\text{--}3050 \text{ cm}^{-1}$. The decrease of peaks at higher wavenumber regions coupled with the reaction products seen in lower wavenumber regions not only indicate the loss of water through desorption but also the loss of hydroxyl groups implying that DMCP decomposes forming the $\nu_a(\text{CH}_3\text{P})$ mode at 2996 cm^{-1} , $\nu_a(\text{CH}_3\text{O})$ mode at 2956 cm^{-1} , which are only seen on the H_2O_2 -treated sample, see Figure 5-12. Based on the interaction with the non-reactive silica surface,¹¹⁴ adsorbed DMCP is expected to exhaust the surface hydroxyl group resulting in the decline of a sharp peak located at 3748 cm^{-1} , which relates to the monodentate (terminal) hydroxyl groups (m-OH). Contrary to the H_2O_2 treated sample, there is only one observed change at higher wavenumbers for the untreated sample, namely the decrease that occurs at 3700 cm^{-1} , which is related to the bidentate (bridged) hydroxyl groups (b-OH). It should be noted that

the apparent differences between XPS and DRIFTS data regarding the presence of OH and water molecules adsorbed at the sample's surfaces arises because the evacuation pressure was 3 orders of magnitude higher for XPS ($\sim 10^{-8}$ torr) than for DRIFTS ($\sim 10^{-5}$ torr) which leads to reduced amounts of weakly adsorbed species.

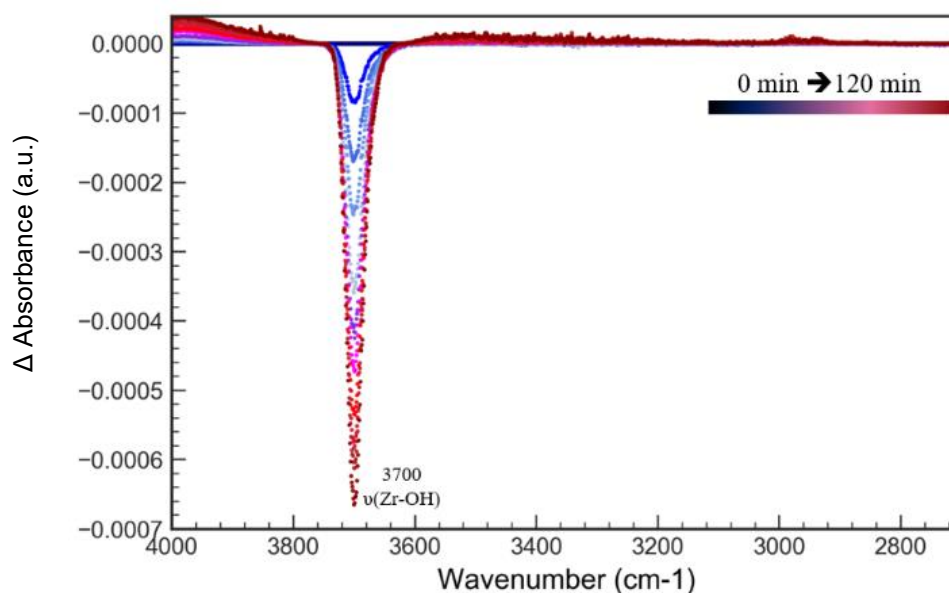


Figure 5-13. High wavenumber region of DMCP on the untreated $\text{ZrO}_2/\text{Zr}(\text{OH})_4$. Time intervals between spectra are: 0, 2, 5, 10, 20, 30, 40, 50, 60, 70, 80, 90, 100, 110, 120 min.

In order to assess if the peak increases are due to decomposition of DMCP or due to reversible adsorption of weakly bound multi-layer/liquid DMCP, a post-purge was performed with He for 2 hr. It is likely that vibrational bands due to weakly bound species would decrease due to desorption. From the two samples, it can be concluded that the H_2O_2 -treated sample provides additional reaction pathways, where the pathway resulting in the asymmetric (O–P–O) mode is the primary adsorbed species.

To confirm the decomposition product, *in-situ* DRIFTS experiments were performed with the anticipated hydrolysis product dimethyl phosphonate (DMHP) (see Figure 5-9). It can be seen that the adsorption of DMHP results in a large mode related to the asymmetric (O–

P–O) binding mode, confirming the decomposition of DMCP. Notably less prominent is the mode near 1144 cm^{-1} which may be attributed to additional decomposition products. Following the He purge, each sample was heated to $220\text{ }^{\circ}\text{C}$ over the course of 20 min then allowed to cool for an additional 10 min in order to further confirm the reactive differences of the two catalysts. Figure 5-14 shows that the peaks located at 1251 cm^{-1} and 1177 cm^{-1} experience monotonic declines, representing weakly bound DMCP and the decomposed asymmetric (O–P–O) mode along with the methoxy mode on DMCP, respectively, and continues to decline upon cooling the H_2O_2 treated sample.

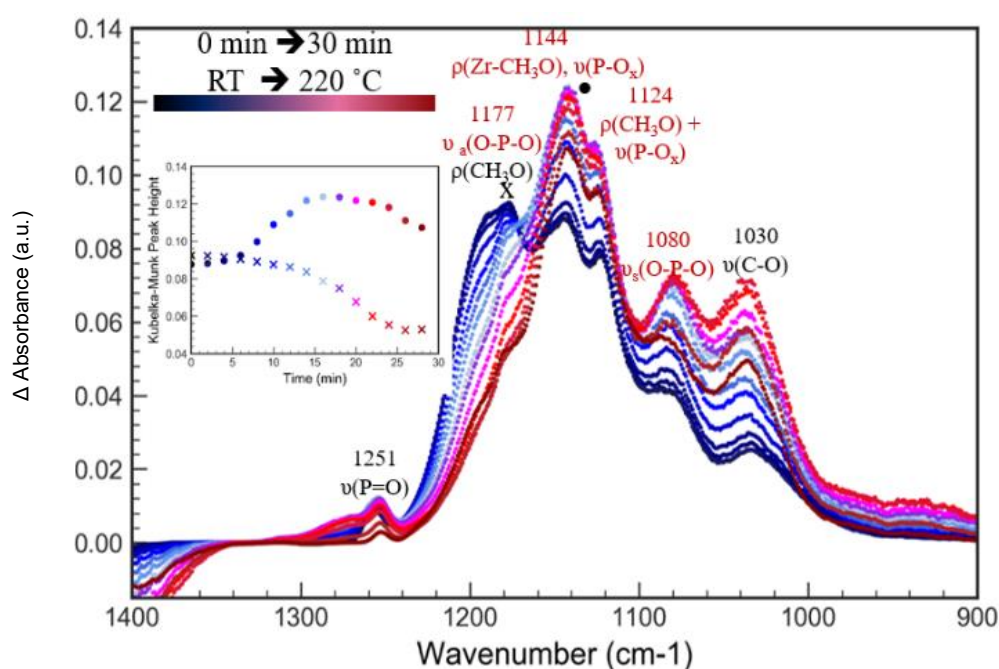


Figure 5-14. Low wavenumber region of the post heating of DMCP on H_2O_2 -treated $\text{ZrO}_2/\text{Zr}(\text{OH})_4$. O = 1144 cm^{-1} , X = 1177 cm^{-1} . Modes in red represent those attributed to decomposition product. Time intervals between spectra are: 0, 2, 4, 6, 8, 10, 12, 14, 16, 18, 20, 22, 24, 26, 28 min.

At the same time, the Zr-bound methoxy mode at 1144 cm^{-1} experiences an initial increase before plateauing near 15 min of heating, followed by a slight decrease upon cooling. Similar non-monotonic trends could be observed for both the symmetric (O–P–O) mode at 1080 cm^{-1} and the (C–O) mode at 1030 cm^{-1} . Meanwhile, the control sample shows a non-monotonic trend for the entire region ($1400\text{--}900\text{ cm}^{-1}$). The trend associated with the

pristine sample results in negative peaks after 10 min for the region, indicating the complete desorption of species possessing these vibrational modes. Post-heating experiments were also carried out with the hydrolysis product DMHP, see Figure 5-15. The presence of an isosbestic point, identified by the simultaneous decrease in the mode occurring at 1177 cm^{-1} and increase in the mode at 1144 cm^{-1} , respectively, confirms the decomposition of the adsorbed DMHP. It should be noted that the spectral difference in the asymmetric (O–P–O) mode for DMHP changes much more rapidly compared to DMCP, indicating that DMHP is more reactive than DMCP.

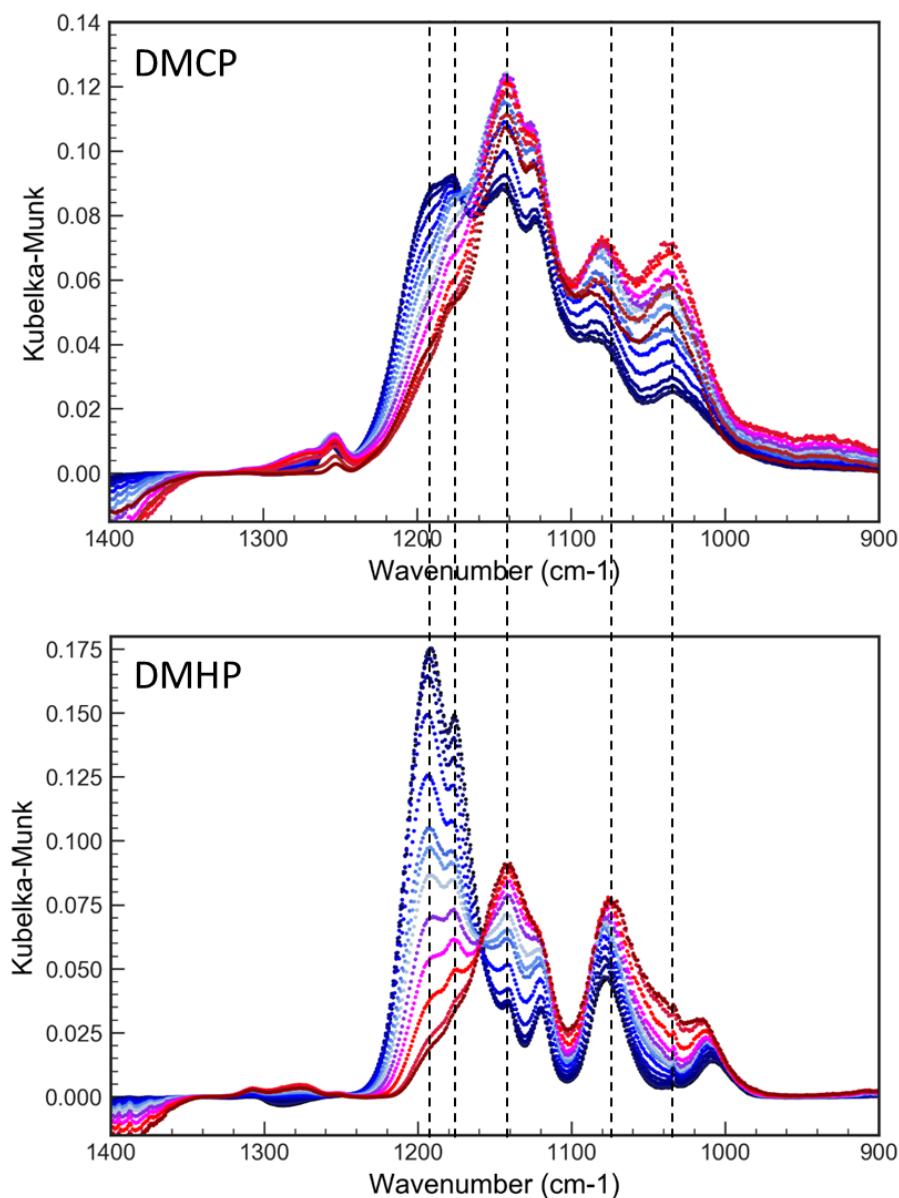


Figure 5-15. Post-heating comparison of DMCP to DMHP exposure on H_2O_2 -treated $ZrO_2/Zr(OH)_4$.

By performing a simple H_2O_2 treatment to metal-oxides, beneficial physical and chemical changes occur within metal-oxide surfaces that improve their decomposition of CWA simulants. Some observed changes include the formation of mesoporosity and reactive surface moieties that enhance agent decomposition.

CHAPTER 6. Photo-Oxidative Decomposition of CWA and Simulants

This chapter is based on work that has been published to the reference shown below, and was used within the author rights as established with publishing company:

- D. Giannkoudakis*, J. Colón-Ortiz*, et. Al., Polyoxometalate hybrid catalyst for detection and photodecomposition of mustard gas surrogate vapors, *Appl. Surf. Sci.*, 2019, **467-468**, 428-438

* Equally contributing first authors

Within the field of CWA decomposition, polyoxometalates (POM) have been previously used mostly for the oxidative decomposition of sulfur containing agents and surrogates and have shown catalytic ability under ambient conditions^{27, 63, 120-121}. There are many opportunities for the investigation of this family of catalysts, since there are not many references for this catalyst within the decomposition of CWA application. We have synthesized a $\text{KCo}^{\text{III}}\text{W}_{12}\text{O}_{40}$ POM that has a deep yellow color, almost golden, when synthesized. This material exhibits an interesting feature as it has the ability to change color based on the oxidative reactions that occur on its surface, bestowing it with colorimetric detection capabilities.

6.1 Physical and Chemical Characterization of POM

The obtained yellow powder and a theoretical 3D representation of the structure of the polyoxometalate (POM) $\text{K}_5\text{Co}^{\text{III}}\text{W}_{12}\text{O}_{40}$ are presented in Figure 6-1(a-b). Based on the nitrogen adsorption analysis, the material is essentially non-porous (surface area: $1.2 \text{ m}^2/\text{g}$, total pore volume: $0.006 \text{ cm}^3/\text{g}$). The TEM images showed nanorods with diameter of 50 to 100 nm, and length of around $1 \mu\text{m}$, Figure 6-1(c). They are stacked together by forming star-like nanostructured aggregates.

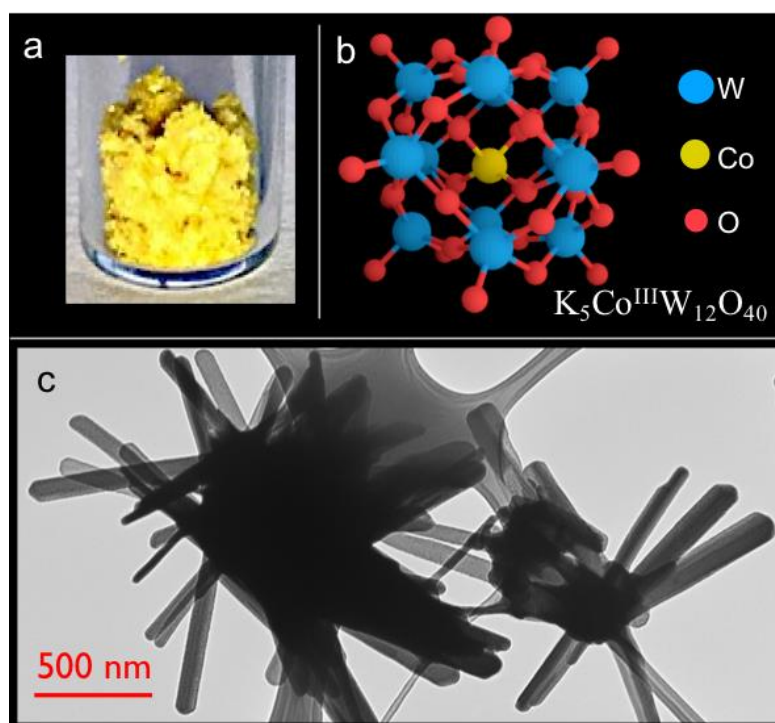


Figure 6-1. (a) POM-h powder of bright yellow color, (b) theoretical 3D representation of the structure of $(\text{Co}^{\text{III}}\text{W}_{12}\text{O}_{40})^{-5}$ ion (red spheres – oxygen atoms, blue spheres – tungsten atoms, and the yellow sphere in the core – cobalt atom), and (c) TEM image of POM-h nanorods.

Inductively coupled plasma (ICP) analysis revealed the contents of W, Co, K, S, and O as 28.7, 0.7, 14.7, 12.0, and 43.7 wt. % approximately. Detection of sulfur suggests that the obtained sample is not a pure POM but rather a hybrid material containing a marked

amount potassium persulfate (KPS), which was added to promote polyoxometalate crystallization, and apparently was not removed during thermal annealing.

The content of W, Co, K, S and O on the surface from XPS analysis was 5.4, 0.7, 14.7, 13 and 66.2 at. %, respectively. Assuming that the surface here represents the bulk composition, the content of W, Co, K, S, and O, in the bulk is 3.2, 1.3, 18.6, 13.5 and 34.4 wt. %, respectively. These amounts agree well with the ICP results. The findings indicate that in the bulk material both components, POM and KPS, are in almost equal quantities per weight. The core energy level spectra of O 1s, W 4f, Co 2p, S 2p, and K 2p are collected in Figure 6-2. The position and shape of the peaks related to W4f are representative for the oxidation state +6^{37,38}. The two components in the O1s spectrum are assigned to the W-O (530.2 eV) and S-O (532.2 eV) bonds, respectively^{38,39}. The low intensity peak at 534.2 eV can be linked to the presence of the hydroxyl groups bonded to tungsten and/or the presence of humidity³⁸. The binding energy of cobalt atoms showed two major peaks at around 782 eV and 797 eV, which represent Co⁺² (2p_{3/2} and Co 2p_{1/2}, respectively).⁴⁰ The deconvolution of the spectrum region for sulfur revealed the presence of the two characteristic peaks of 2p_{3/2} and 2p_{1/2} representing sulfates.^{39,41} The 2p spectrum of potassium showed also the two well separated characteristic peaks corresponding to K 2p_{3/2} at 293.3 eV and K2p_{1/2} at 296.0 eV characteristic to potassium ions.^{42,43} The morphological structure of the hybrid material was evaluated extensively by SEM. The images (Figure 6-3) revealed morphologically different structures for two components of this material. The polyoxometalate phase consist of two different structures; the hexagonal rod-like particles (with a diameter in the range of 15-25 µm and length between 70 and 90 µm) and the orzo

like particles with sizes from 600 nm to 2 μm . In the former, the particles are colored yellow and are indicated by the yellow arrows in the SEM images, Figure 6-3(a, b, g, h).

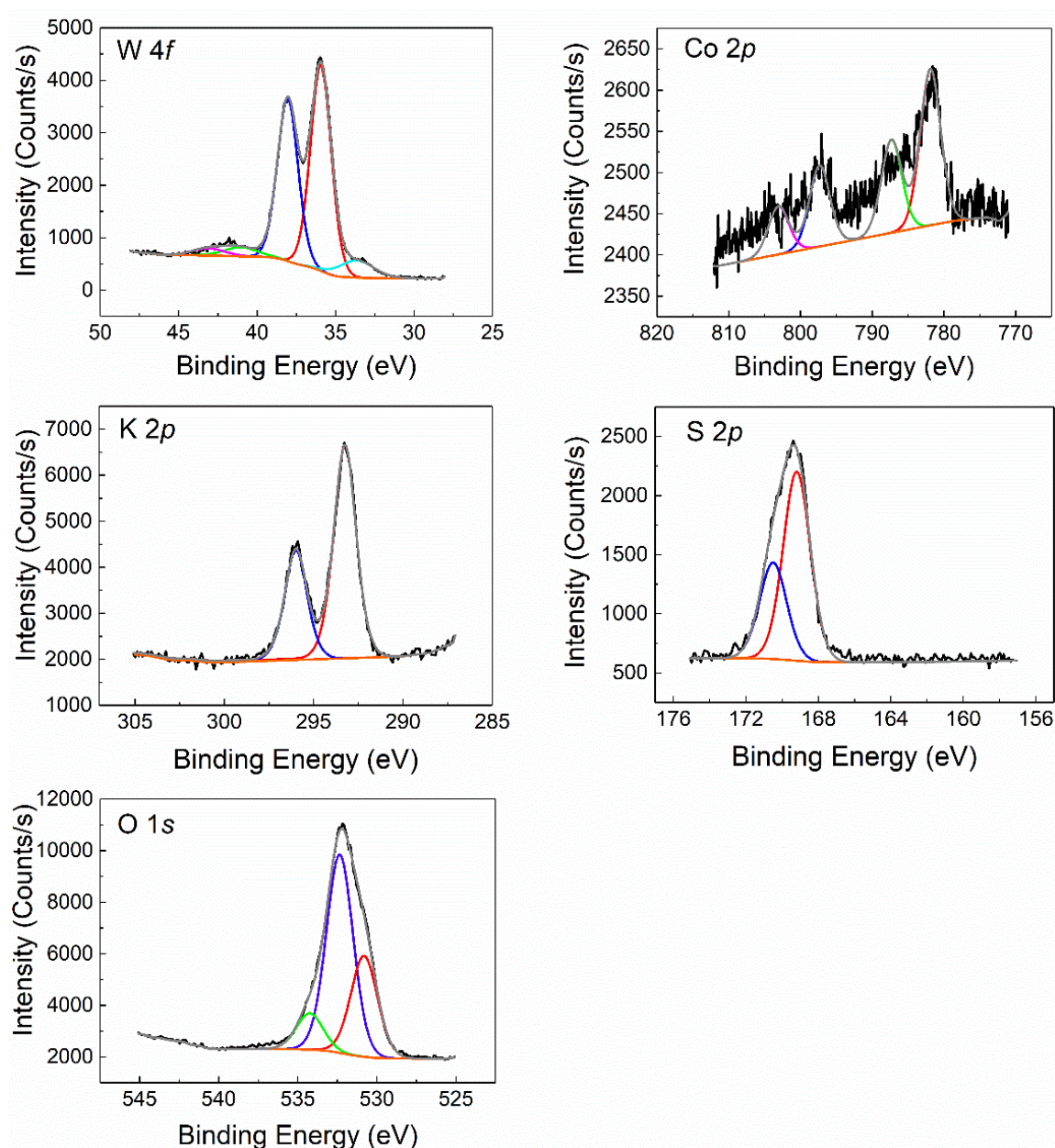


Figure 6-2. *O 1s, W 4f, Co 2p, S 2p, and K 2p core level spectra of POM-h.*

Colored cyan areas at the SEM images can be linked to a polyoxometalate phase that appeared in a very small quantity in between the bulky phase of hexagonal rod-like particles of POM and KPS. The EDX elemental mapping analysis in Figure 6-3(c-f)

supports the presence of tungsten in these regions. It is plausible to assume that the bulky hexagonal rods observed in the SEM images consist of bundles of nanorods. It is likely that the bulky POM-based rods were disassembled by the solvent (isopropanol) after sonication during the preparation of the samples for the TEM analysis.⁴⁴ The orzo-like particles are colored red and indicated by the red arrows in Figure 6-3. The KPS phase has three kinds of morphologies (green arrows in Figure 6-3): long rods (or elongated prisms), polyhedrals, and platelets. The appearance of these two phases of POM might be related to differences in the crystallization process. Potassium on KPS might participate as a "seed" in the growth of small POM particles highly dispersed on the surface of KPS phase. The absence of the cobalt signal on EDX maps could be due to its limited amount in the crystallographic phase of POM (1.7 % based on the $\text{K}_5\text{CoW}_{12}\text{O}_{40}$ elemental stoichiometry), or due to the beam obstruction by the larger W atoms that surround the Co atoms. The EDX maps further confirm that POM-h is a hybrid material containing two separate phases.

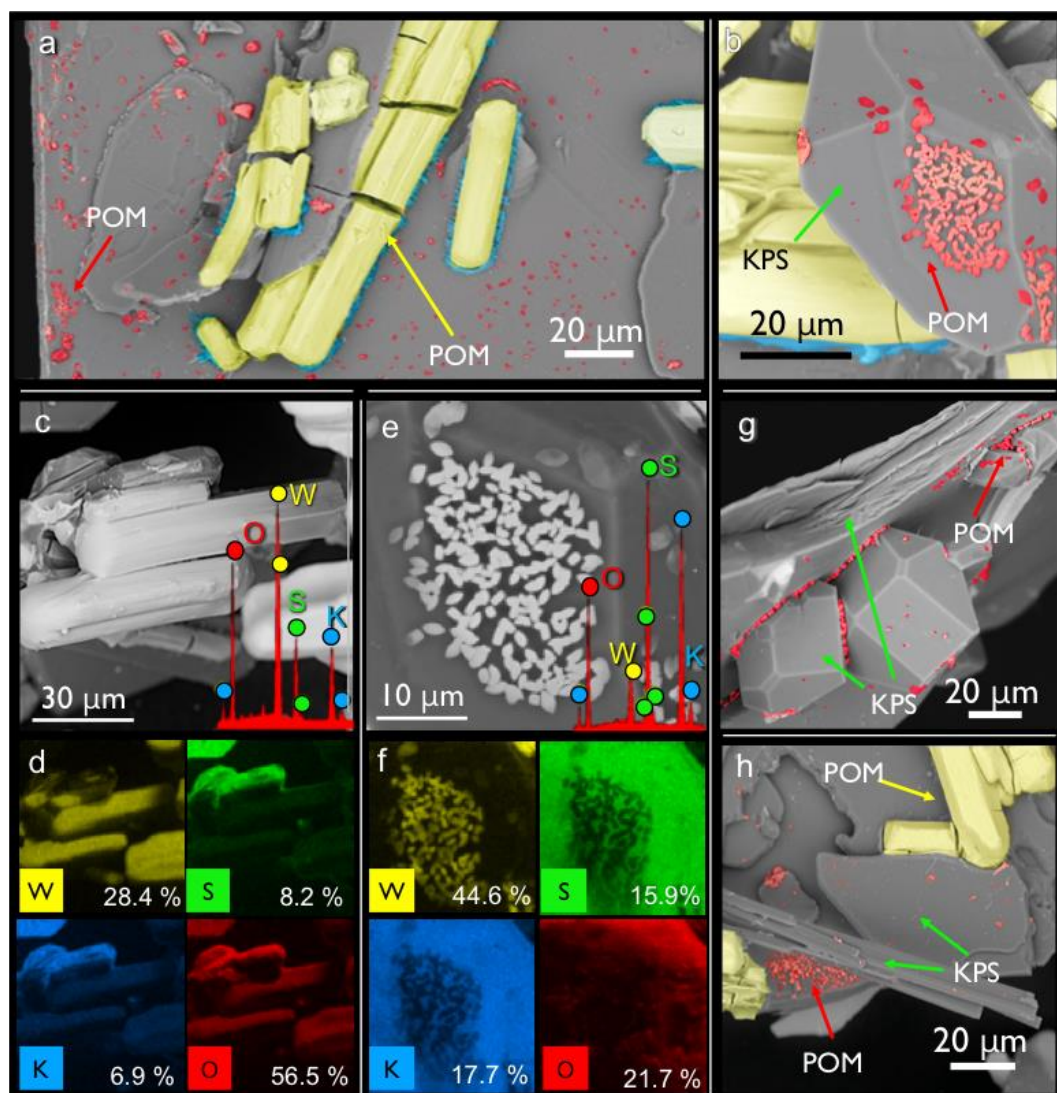


Figure 6-3. SEM images of (a-b) POM-h (polyoxometalate phase colored yellow and red, yellow arrows indicate the rod-like POM, red arrows -the orzo like particles, and green arrows-the potassium persulfate phase), (c-d) with the EDX elemental energy histogram as insets, and (d, f) EDX maps with weight percent of detected elements.

The X-ray diffraction pattern of POM-h, Figure 6-4(a), shows various characteristic reflections of potassium persulfate (ICSD card 01-087-0310).⁴⁵ The peaks that are not linked to KPS (at 10.7, 17.7, 20.6, 21.6, 24.7, 31.9, 41.1, and 54.5 2 θ) are assigned to the polyoxometalate phase of the material.¹⁹ FTIR spectra of POM-h and KPS are collected in Figure 4b. For KPS, three strong and sharp bands are revealed at 1259, 1059, and 683 cm⁻¹

¹; the first two are linked to the asymmetric stretching vibration of the S=O bond and the third one- to the bending vibrations of O=S=O.⁴⁶ For POM-h, three additional intense bands appear at 1629, 949, and 871 cm^{-1} , that are assigned to vibration of the bonds between the metal and oxygen atoms, Figure 6-4.⁴⁷ The wide band in the range from 3600 to 3300 cm^{-1} represents the structural water molecules.⁴⁸ The XRD and FTIR results agree with the EDX element maps. XPS and ICP results also revealed almost equal in weight contributions of the polyoxometalate and KPS phases in POM-h.

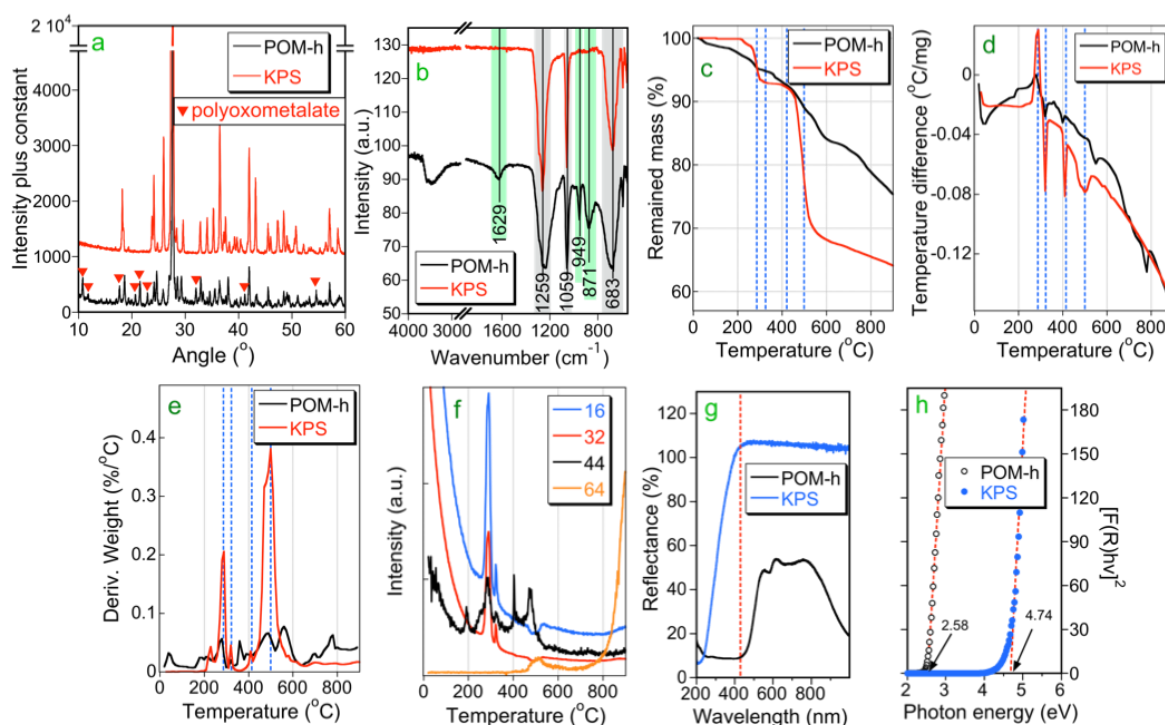


Figure 6-4. XRD patterns (a), FTIR spectra (b), thermal analysis (TA) curves (c), DTA curves (d), DTG curves (e), of pure KPS and synthesized POM-h nanorods, MS thermal profiles (in helium) of the fragments representing oxygen (m/z 16), O_2 or S (m/z 32), CO_2 (m/z), and SO_2 (m/z 64) for KPS (f), diffuse reflectance UV-Vis-NIR spectra (g), Tauc plots of KPS and POM-h (h).

To gain more information on the chemical nature of the POM-h nanorods, the obtained yellow powder and pure KPS were exposed to heating in helium atmosphere. The TA, DTG, and DTA curves are collected in Figure 6-4 (d-f). The DTA curve of KPS

showed one exothermic decomposition peak with maximum at 290 °C and three endothermic ones with maxima at 320, 410, and 500 °C. The weight losses associated with these changes are 5.5, 0.8, 0.7, and 25.9 %, respectively. Taking this into consideration, along with the results of the MS analysis of the species released during the heating process that contain oxygen (m/z 16), O₂ or S (m/z 32), CO₂ (m/z 44), and SO₂ (m/z 64), these weight losses are assigned to the removal of the water of crystallization, and the transformation of potassium persulfate to sulfur dioxide and potassium sulfate. The decomposition of the latter starts at above 850 °C. The DTG and DTA curves of POM-h were more complex with more decomposition steps than those of KPS. The total weight loss for POM-h was 24.6 %. Based on the comparison of the weight loss of POM-h between 200 and 600 °C (13.8 %) and of pure KPS in the same temperature range (30.9 %) the amount of KPS in our sample was estimated to be around 55 %. This is in good agreement with the amount of KPS in the final material provided by the ICP and XPS analyses.

UV-Vis-NIR diffuse reflectance spectra evidenced the POM-h nanorods' photoactivity, Figure 6-4(g). Pure KPS (as used for the synthesis) is a white powder and thus it is not expected to affect the bright yellow color of the POM phase. As revealed from the UV-Vis spectra, KPS does not absorb light at a wavelength above 410 nm. Thus, POM-h spectrum showed significantly lower reflectance than that of pure KPS in the range of visible light (VL). An estimated indirect band gap from the Tauc plot of the POM-h nanorods, Figure 6-4(h) is 2.58 eV (480 nm, blue region of the visible light).^{49–52} This value suggests that the material is photoactive in VL. It is also consistent with that reported in the literature for this particular polyoxometalate phase estimated by DFT studies.⁵³ On the contrary, pure KPS revealed a band gap of 4.74 eV (260 nm, deep UV region).

6.2 Photo-oxidative Capabilities of POM against H-agent Simulants

To test the decomposition/detoxification capability of POM-h, 2-chloroethyl ethyl sulfide (CEES) and diethyl sulfide (EES) were chosen as mustard gas surrogates. The tests were carried out in the vials-in-vial (ViV) closed adsorption system.⁵⁴ Knowing that the band gap of POM-h is in the VL range, the tests were run under ambient light and in the dark for 24 hours. The detoxification performance was estimated based on the weight uptakes and GC-MS analysis of the headspace after exposure to vapors. Weight uptakes upon exposure to surrogates are the first quantitative markers of the adsorption performance. They are expressed in mg per gram after 24 hours of exposure under light or in the dark. These values represent the adsorbed amounts of the surrogates/their decomposition products and they are not directly related to the number of surface-active sites. The results for POM-h and KPS are summarized in Figure 6-5(a). The weight uptakes (WU) for both materials are very low (in an absolute value), due to the negligible porosity. An important finding of this test, however, was a decrease in the weight of POM-h under light and an increase in the dark. For KPS, no weight change was recorded, since the values measured were within the balance's range of error. This indicates a lack of interaction/adsorption/detoxification activity of this phase. The trend in WU found for POM-h corroborates its photoreactivity. The collected data also suggests that POM-h is more active against CEES than it is against EES, since the absolute WU values upon exposure to the former are higher than those upon exposure to EES. Those recorded negative values of WU can be linked to the reactivity of the surface, which reflects a release of more gaseous products than those adsorbed/interacting on/with the surface. Extension of the exposure to surrogate vapors up to 7 days led to clearly positive values of WUs under all conditions, Figure 6-5. In the case of CEES exposure, the WUs measured under light

and in the dark were 45 and 12.5 mg/g, respectively, and for EES these values were 40 and 7.5 mg/g, respectively. In order to exclude the possibility of the weight due to instability of POM-h, the weights were also recorded for the vials with 20 mg of POM-h s without the presence of the surrogates. They were found stable either after 1 day or after 7 days. Weighing empty vials also led to stable readings.

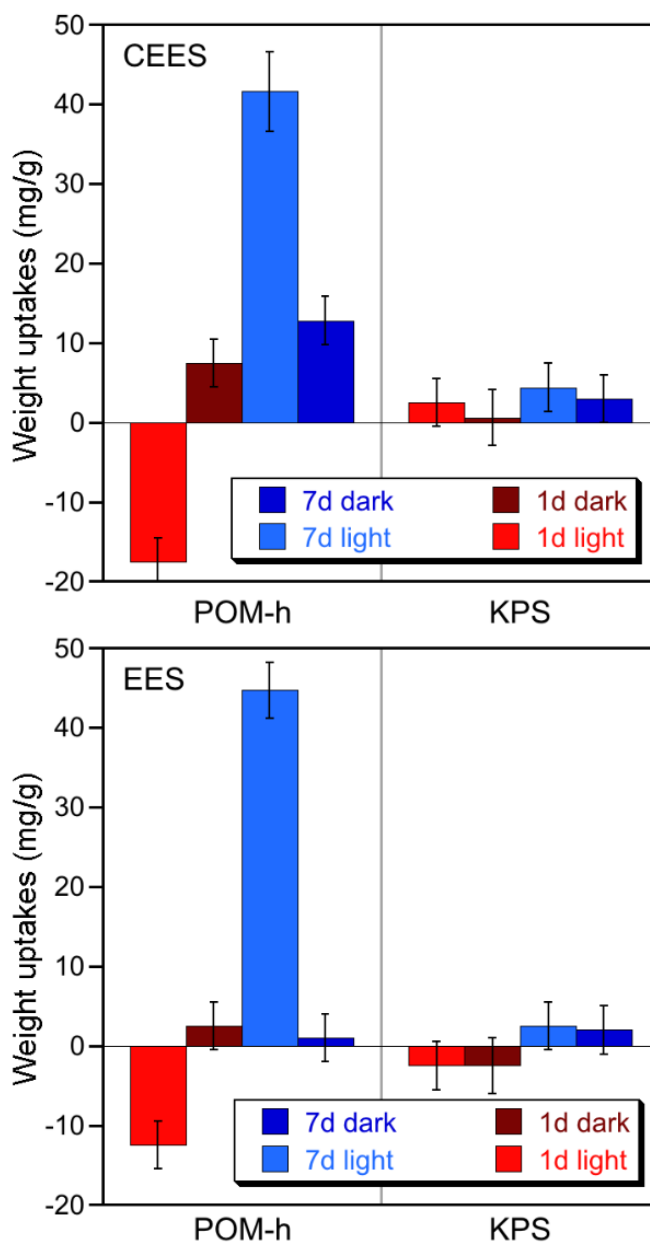


Figure 6-5. The recorder weight uptakes/changes after interactions with CEES or EES vapors for 1 and 7 days under light or in the dark.

The above discussion suggests that various interactions pathways might govern the surface interactions of our POM-h material with the CWA surrogates. They include: 1) weak retention of surrogate molecules on the surface; 2) degradation of surrogate molecules to smaller compounds that get attracted on the surface; 3) removal of some surface functional groups or exchange of some structural moieties with smaller ones, as a result of photoreactivity. Moreover, the removal of physically adsorbed water and its replacement by the reaction products is another reactivity scenario, since the initial material consisted of 4.2 % of adsorbed water (from TA until 200 °C ~2%). These pathways might occur simultaneously, and they are competitive to each other with respect to weight change. Pathways 1 and 2 should lead to the weight gain, while the third to the weight loss. The results suggest that under light the latter process occurs faster than the other two (weight gains) since negative WUs were recorded after exposure to CEES and EES. On the contrary, the slight increase in WUs in the dark suggests that the first two pathways predominate under these conditions.

The CEES and EES exposed samples were also weighed after being left inside a hood under VL irradiation and ambient conditions for additional 24 hours. The recorded WUs were -28 and -37.4 mg/g for the samples that were exposed to CEES and EES for 1 day, respectively. The WUs recorded for the samples exposed for 7 days were -20 and +5 mg/g. A further decrease in the samples mass after air exposure implies that the adsorbed molecules underwent a catalytic decomposition and were desorbed from the surface along with some surface components. Even though the absolute values of the weight uptakes are lower than those of various other materials that were evaluated under the same conditions (such as barium titanate nanoparticles, zinc hydroxide, zinc peroxide nanoparticles,

oxidized graphitic carbon nitride nanospheres, or mixed oxides),^{55–59} the fluctuations of WUs support an elevated activity for decomposition/degradation rather than adsorption. In fact, owing to the lack of surface area, we do not consider POM-h as an adsorbent.

To further test the samples reactivity, the headspace of the ViV adsorption systems was analyzed by GC-MS after 1, 6, and 24 hours of exposure to CEES or EES. These tests revealed a wide range of formed products upon exposure to both surrogates. In order to monitor the evolution of the formed products, the headspaces were analyzed by GC-MS after 1, 3, and 7 days of exposure to surrogates. The recorder chromatograms are collected in Figure 6-6. Details on all identified compounds, their linear chemical formula, nomenclature, and abbreviation, are collected in Figure 6-6(c-d) and Table 6-1.

In the case of CEES exposure, the detection of volatile thiirane (ThR), ethanol (EtOH), acetaldehyde (Ace), acetic acid (Aca), and diethyl disulfide (DEDS) is evidence that POM-h has the ability to decompose CEES to smaller compounds, through the cleavage of the S-C bond.^{2,57,60} Additionally, the formation of Ace and Aca as a result of EtOH oxidation elucidates the photo-oxidative capability of the nanorods.^{60,61} When the tests were performed in the dark, these products were not formed. The cleavage of the carbon/sulfur bond can occur through the formation of a transient intermediate cyclic sulfonium cation.^{58,62–65} The detection of the dehydrohalogenation product, ethyl vinyl sulfide (EVS), verifies the occurrence of the abovementioned reaction pathway.^{62,64–68} On the other hand, the formation of diethyl sulfide (EES) suggests that the dehalogenation by a nucleophilic attack from the active surface to the chloride atom of CEES is another alternative interaction pathway.^{62,69}

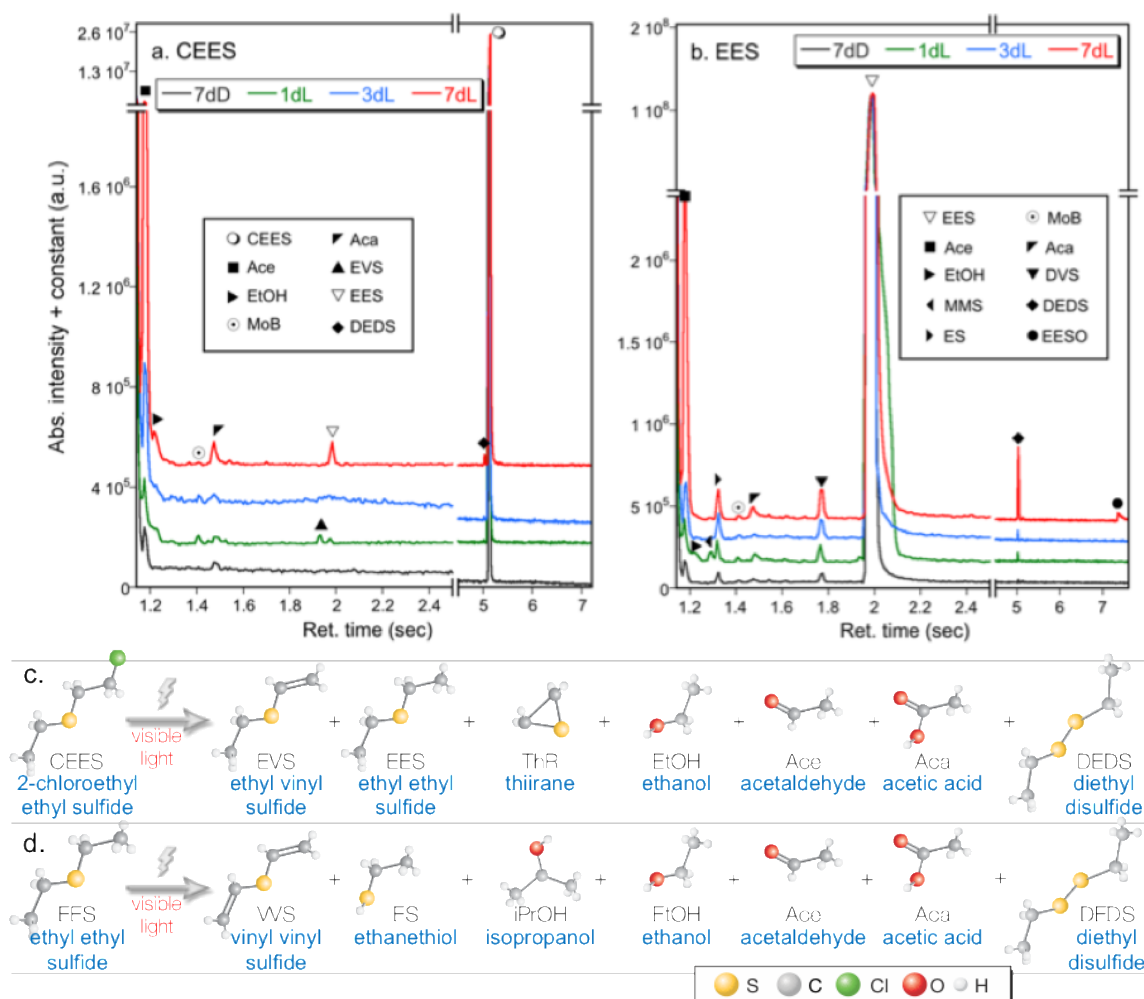


Figure 6-6. Chromatograms of the headspace after exposure to (a) CEES and (b) EES vapors under light irradiation for 1 (1dL), 3 (3dL), and 7 (7dL) days, and in the dark for 7 days (7dD); (d) the names, abbreviations, and the chemical structures of all detected compounds exposed to CEES (c) or EES.

The oxidative ability, the cleavage of the S-C bond, and the formation of EES can also be explained by the involvement of radical reactions.^{70–75} When the tests were performed in the dark, only EVS was detected. In order to ensure that the formed compounds are the result of the interactions of the surrogate vapors with the polyoxometalate phase of POM-h and not due to the KPS presence, the adsorption test and the analysis of the headspaces were also performed on pure KPS powder and no reactivity was observed.

Table 6-1. All identified compounds in the headspace of ViV, along with details on their nomenclature, linear chemical formula, abbreviation, molar mass, and retention times (min) at the chromatograms

Name	Linear Chemical Formula	Abbrev.	Molar Mass	Retention Time (min)
Acetaldehyde	CH ₃ CH ₂ O	Ace	44	1.18
Ethanol	CH ₃ CH ₂ OH	EtOH	46	1.22
Isopropanol	CH ₃ CH ₂ OHCH ₃	iPrOH	60	1.26
Methyl methyl sulfide	CH ₃ SCH ₃	MMS	62	1.29
Ethyl sulfide	CH ₃ CH ₂ S	ES	61	1.32
1-methoxybutane	CH ₃ CH ₂ CH ₂ CH ₂ OCH ₃	MoB	88	1.41
Thiirane	C ₂ H ₄ S	ThR	56	1.44
Acetic acid	CH ₃ COOH	Aca	60	1.48
Ethyl acetate	CH ₃ COOC ₂ H ₅	EAc	88	1.56
Divinyl sulfide	CH ₂ =CHSCH=CH ₂	DVS	84	1.78
Ethyl vinyl sulfide	CH ₃ CH ₂ SCH=CH ₂	EVS	88	1.94
Ethyl ethyl sulfide	CH ₃ CH ₂ SCH ₂ CH ₃	EES	90	1.98
Diethyl disulfide	CH ₃ CH ₂ SSCH ₂ CH ₃	DEDS	122	5.03
2-chloroethyl ethyl sulfide	CH ₃ CH ₂ SCH ₂ CH ₂ Cl	CEES	124	5.12
ethyl ethyl sulfoxide	CH ₃ CH ₂ SOCH ₂ CH ₃	EESO	138	7.26

The photo-catalytic detoxification and photo-oxidative ability of POM-h reflects the detection of DVS, DEDS, EtOH, Ace, and Aca. The photo-oxidative ability of POM-h can be also supported by the detection of ethyl ethyl sulfoxide (EESO) in the headspace after 7 days of exposure. It was detected only in the extracts of the exhausted samples, and it has never been identified in the headspace. EESO has a low volatilization rate at room temperature and can interact via specific forces with oxygen of the POM phase.

The presence of ethanethiol (ES), diethyl disulfide (DEDS), divinyl sulfide (DVS), and isopropanol (iPrOH) in the headspace verifies the involvement of radical reactions, since ethyl (ES^*), methyl (MS^*) and hydroxyl (OH^*) radicals, which recombine via different combinations in order to form DEDS, iPrOH or EtOH.^{55,56} The latter was photo-oxidized further to acetaldehyde and acetic acid, as in the case of CEES exposure. The interactions of EES vapors with POM-h nanorods in the dark, or with KPS at light did not lead to the formation of the abovementioned compounds. Another important finding is an increase in the intensity of the GC peaks representing EVS and after CEES exposure. The formation of EVS also in the dark indicates that dehydrohalogenation via an intermediate transient cyclic cation is not associated with the photoactivity of POM-h. Moreover, EVS did not degrade to other compounds.

To further investigate the POM-h activity, the trends in the EtOH and Aca GC peaks' intensities were analyzed. While the results indicate a stable concentration of EtOH, a declining trend is noticed for Aca. These findings suggest a continuous formation of EtOH that is further oxidized to Ace. The formed Aca upon Ace oxidation seems to be

further decomposed/mineralized to undetectable organic compounds with molecular weight less than 40 (detection limit of the GC-MS instrument), for example CH₄ or CO₂. The same trends in the GC peaks' intensity were revealed after EES exposure. In general, it is plausible to conclude that POM-h acts as a photocatalyst, degrading and/or oxidizing CEES and EES vapors in a fast and continuous manner. In the case of EES exposure, the increases in the concentrations of DEDS and DVS from 1 to 7 days of exposure further support that POM-h acts as a detoxifier in a continuous mode.

Analyzing the results one cannot exclude that more compounds were formed upon interacting with the POM-h, and they could not be detected in the headspace due to their low volatility and/or to the strong retention on the surface, as it was found for various materials exposed to HD surrogates.^{36,62,74,76} The main product detected in the extract of the samples exposed to EES is an oxidized compound, EESO. As indicated in the literature, this kind of materials can be considered rather as catalyst precursors than catalyst themselves, since polyoxoperoxo complexes were suggested as actual active sites for the formation of reactive oxygen species participating in oxidation reactions.^{12,23,25,77-79}

6.3 Colorimetric Sensing Capabilities of POM with respect to H-agent Simulants

The multi-functionality of advanced materials to simultaneously sense, in addition to degrade/adsorb, is also an important asset for their application as decontamination/detection media from the vapor phase and also for other potential applications.^{33,80-82} As seen in Figure 6-6, the initial bright yellow color of the sample turned gradually to light greenish turquoise with various shades upon exposure to toxic vapors of the surrogates. The more intense green shade in the case of EES exposure suggests differences in the detoxification pathways. It is worth mentioning that this color

change occurred even after 10 minutes of exposure. Taking into consideration that some lag time is needed for CWA surrogate to evaporate in our testing system, these results suggest that POM-h can be used as a fast detector of mustard gas vapors. The gradual color change is an interesting property, since it can also be used, upon calibration, to monitor the exhaustion level of a protection medium.

In order to determine whether or not POM-h can colorimetrically detect the presence of CEES or EES in their liquid form, droplets of the two surrogates were deposited on the POM-h powder. The color changes of the powder after five minutes of the droplet exposure, Figure 6-7, clearly shows the detection of the surrogates in the liquid forms. The darker final color in the case of CEES due to the presence of Cl at the surrogate molecule can be a beneficial fact for a potential sensor function.

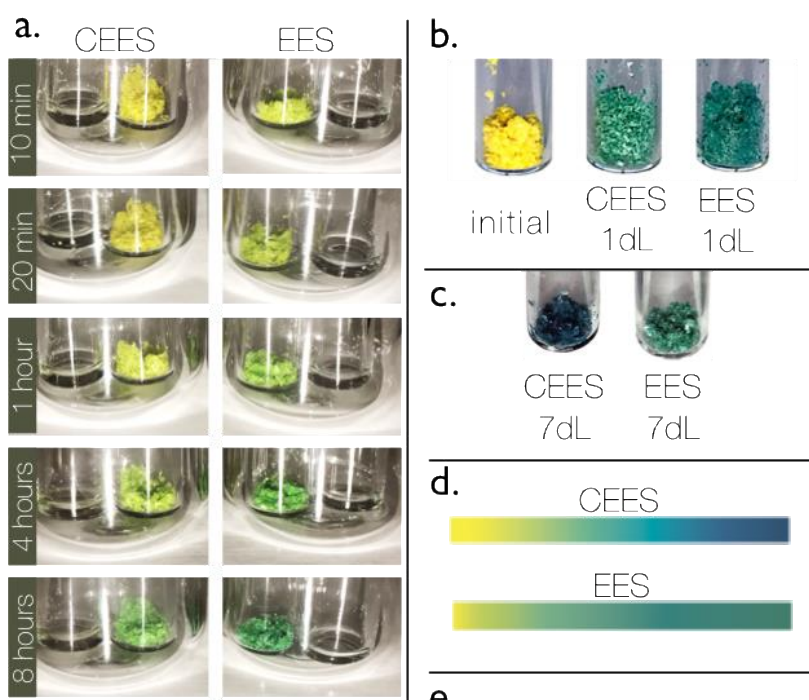


Figure 6-7. (a) Fast and gradual color changes upon the exposure to CEES and EES vapors at ambient light irradiation up to 24 hours, (b) the initial powder and the samples exposed for 1 day under ambient light (1dL) to CEES and EES, (c) the exposed samples to CEES and EES for 7 days under light (7dL), (d) a gradient representation of the gradual color during the exposure to CEES and EES vapors, (e) and the color after exposure of the powder to the droplet of the surrogate.

Our studies revealed that H-agent simulant detoxification occurs through various and complex photo-catalytic and photo-oxidative pathways with the formation of numerous products. The detection of compounds with smaller molecular weight than those of the surrogates and also the detection of oxidation products suggest the ability of the POM-h surface to break the S-C bond, and to promote the formation of hydroxyl radicals and other active oxygen species. In addition, POM-h can be considered as a potential multifunctional detoxifier, since its ability to gradually change color during the exposure to the toxic vapors can be a crucial asset for potential applications as a rapid CWAs sensor/detector or for the monitoring of the protection media exhaustion level.

CHAPTER 7. Transport Properties and Protective Capabilities of PEM Composites

This chapter is based on work that has been published to the reference shown below:

- J. Colón-Ortiz*, et. Al., Permeation Dynamics of Dimethyl Methylphosphonate through Polyelectrolyte Composite Membranes, Submitted to Chemistry and Reaction Engineering

Understanding the behavior of CWA/CWS through barriers enables the designer to devise clever ways to enhance the protective qualities of the materials involved in the protective fabric. Our goal is to develop a self-decontaminating barrier that would hinder the diffusion of CWA while providing catalytic centers for the decomposition of such agents.

7.1 DMMP Sorption within MONP-PEM Composites

To understand permeation of CWA/simulants through PEM a series of sorption studies were performed to estimate the saturation amounts of DMMP within PEM and MONP-PEM composites. In Figure 7-1(a) a series of experiments are presented where the amount of water absorbed by the material was recorded as a function of time exposed in a water bath for initially dry membranes. In all Nafion samples the total amount of water uptake is approximately 17 wt.%. It seems that water uptake is independent of chemical treatment for Nafion membranes whereas for Nexar membranes the difference among samples is quite sharp. Nexar-H⁺ and Nexar-Zn²⁺ absorb about 60 wt.% their dry weight but Nexar-ZnO absorbs almost 100 wt.% its own dry weight. It appears that MONP presence within PEM favors the absorption of water within Nexar membranes. Figure 7-1(b) shows that

Nafion and SEBS membranes equilibrate significantly much faster than Nexar membranes when absorbing water.

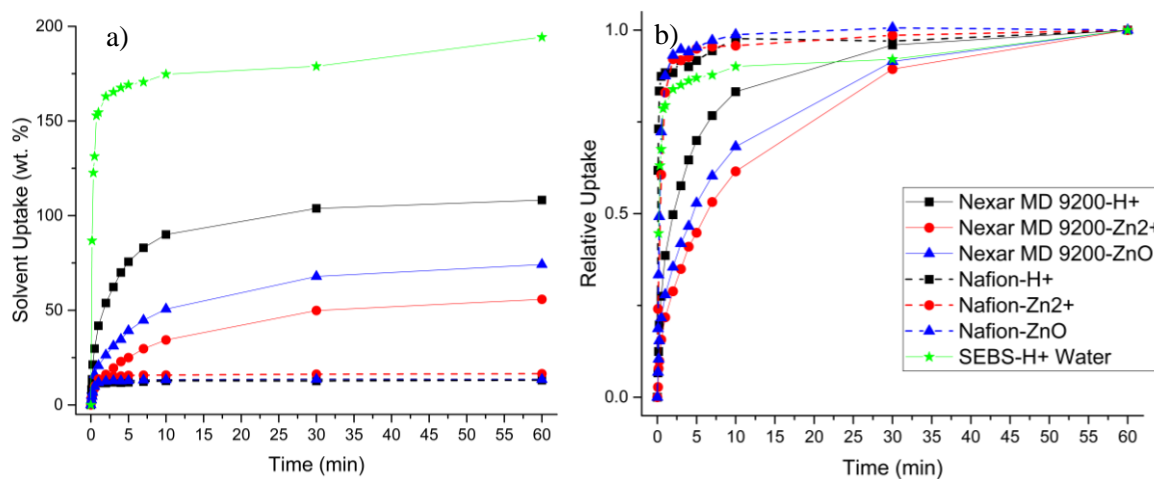


Figure 7-1. a) Sorption of water and b) relative sorption of water (with respect to saturation at 60 minutes) as a function of time within: Nafion-H⁺ (black squares-dashed line), Nafion-Zn²⁺ (red circles-dashed line), Nafion-ZnO (blue triangles-dashed line), Nexar-H⁺ (black squares-solid line), Nexar-Zn²⁺ (red circles-solid line), Nexar-ZnO (blue triangles-solid line), and SEBS-H⁺ (green stars-solid line).

In Figure 7-2(a) similar experiments are shown where DMMP sorption is obtained as a function of time until saturation for Nafion membranes. Results are compared against

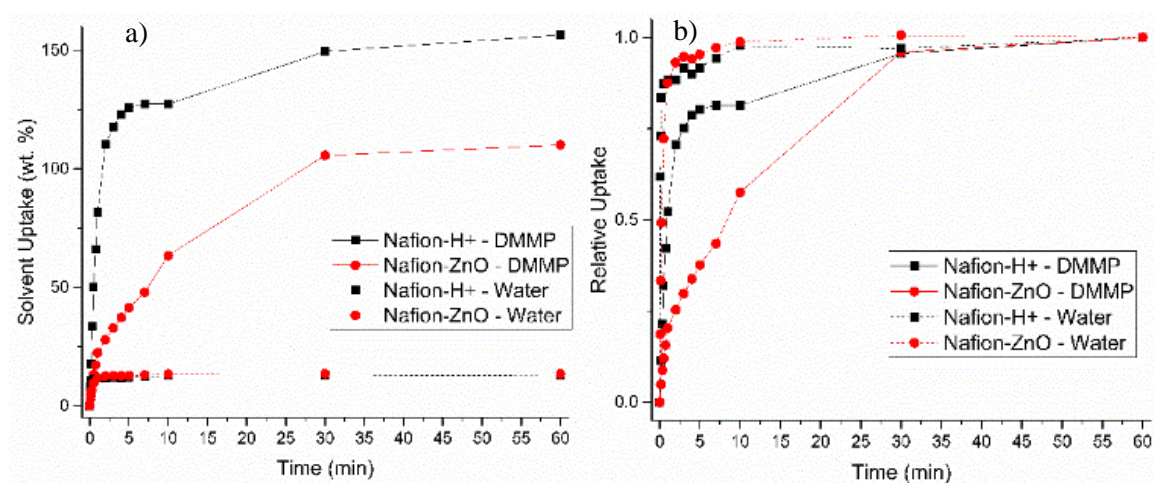


Figure 7-2. a) Sorption and b) relative sorption (with respect to saturation at 60 minutes) as a function of time for: Water-Nafion-H⁺ (black squares-dotted line), Water-Nafion-ZnO (red circles-dotted line), Nafion-H⁺ (black squares-dashed line), Nexar-ZnO (red circles-dashed line).

water sorption in Nafion membranes. DMMP uptake in Nafion-H⁺ sample is approximately 150 wt. % whereas for Nafion-ZnO the DMMP uptake is closer to 100 wt. %. In this case

the presence of MONP appears to be detrimental for the sorption of DMMP within Nafion membranes. In Figure 7-2(b) One can observe that Nafion saturates much faster with water than with DMMP. Given that Nafion membranes only absorb about 17 wt. % of water, it is reasonable to observe that Nafion membranes saturate much faster than with DMMP. On the other hand, the uptake of DMMP is much faster than with water as Nafion saturates with DMMP in a similar amount of time when compared to absorbing water.

7.2 Liquid Water-and Water-Vapor Sorption within MONP-PEM Composites

Another property of interest is the water-vapor adsorption of PEM as is it very important for these materials if they become implemented within military textiles. Although these PEM have the same sulfonate groups, their microstructure, ion exchange capacity and water sorption are quite different. In this case, Nafion and Nexar were challenged to a water vapor adsorption experiment to observe how water vapor behaves as it becomes in contact with these PEM. Nexar has nearly double the ion-exchange capacity (IEC) of Nafion and can absorb close to 6 times more water than Nafion. Water sorption experiments were held at room temperature and membranes were immersed in liquid water. Max sorption was taken at 1-hour as the difference between 1-hour and 24-hour sorption was insignificant in our case.

One parameter of importance for this study is the history that each sample experiences: H^+ and Zn^{2+} samples only experience chemical treatment, while ZnO samples experience chemical and thermal treatment, which can influence how they behave, yielding different behaviors under the same subjected conditions. Given this note, more samples have been prepared such that they would all be subjected under the same thermal treatments to remove any variability from processing history from sample to sample. In Figure 7-3(a)

the mass of water vapor solvated in the sample is presented as the relative humidity of the chamber increases to saturation. Nexar samples in acid form, metal-substituted and incorporated ZnO. Similarly, data is presented for Nafion, see Figure 7-3(b).

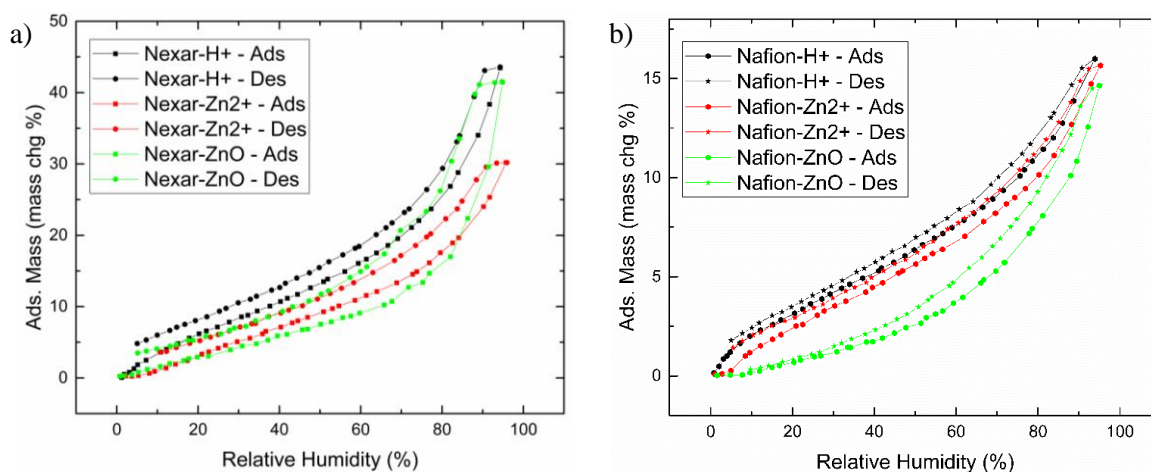


Figure 7-3. Water-vapor sorption isotherms (adsorption and desorption branches): (a) Nexar- H^+ (black), Nexar- Zn^{2+} (red), Nexar-ZnO (green) (b) Nafion- H^+ (black), Nafion- Zn^{2+} (red), Nafion-ZnO (green).

In Figure 7-3(a), one can observe that Nexar in acid form has the highest water-vapor uptake (also happens for Nafion). It seems like membranes in the acid form have the least trouble to solvate water. As the membranes are further processed (chemically and thermally), it becomes more challenging for the samples to solvate water. For metal-substituted membranes, water transport can become more challenging due to steric hindrances from much larger cations, such as Na^+ and Zn^{2+} that obstruct the transport of water molecules through the membrane's inter-connected hydrophilic clusters. In addition, zinc ions can act as ionic cross-linking centers within polymer chains making polymer relaxation (swelling)/water solvation more difficult. For ZnO incorporated samples, not only there are sodium ions interacting with the sulfonated moieties, but also the presence of ZnO nanoparticles. These nanoparticles can behave as anchors for water molecules and also to surrounding polymer chains, stabilizing the membranes as ZnO interacts with surrounding polymer chains (also true for TGA experiments where PEM-ZnO samples

increased their degradation temperature). In addition to all previous possible scenarios discussed, add the thermal treatment that ZnO-PEM samples experience. As the membranes are subjected to heat, membranes collapse and become stiffer and denser increasing the difficulty of water solvation at water-vapor/membrane interfaces. This can explain why ZnO-PEM samples show that adsorption branches are below adsorption branches of other non-thermally treated samples in the lower relative humidity regions.

In the case of Nexar-ZnO, it is possible that after some water-solvation energetic barrier is surpassed a large amount of water vapor can be adsorbed due to high amount of ZnO within the substrate. Since ZnO can act as attractive centers for water molecules, it becomes increasingly easier to solvate more water vapor. Nexar-ZnO sample shows the largest hysteresis, which can be explained due to ZnO anchoring water-molecules, leading to much more difficult desorption. In addition to diffusion limitations, now water molecules have to surpass the energetic barrier of desorption from the highly hydrophilic ZnO surfaces yielding large hysteresis. Nafion and Nexar samples exhibit open hysteresis loops, which may be an indication of the irreversibility of the sorption of water within samples. Nafion membranes have been known for irreversible sorption properties as they have strong interactions (tightly bound) with solvents and have poor memory (ability to recover towards previous structural configurations)¹²².

In the case of Nafion-ZnO, as the sample is heated first at 60 °C and later at 100 °C, it collapses (increases in density) and becomes stiffer. In this state, the polymer chains are closer together and can lightly cross-link with neighboring ZnO nanoparticles, making water sorption (and polymer chain relaxing) more difficult. This can lead to membrane

requiring higher humidity conditions in order to solvate water within itself when compared to non-thermally treated samples (Nafion-H⁺ and Nafion-Zn²⁺).

7.3 *In-situ* Monitoring of DMMP Permeation Dynamics across MONP-PEM Composites

For this study two sets of PEM were used to assess their capabilities as protective materials against chemical warfare agent (CWA) surrogates, such as dimethyl methylphosphonate (DMMP), Nafion 117 and Nexar MD9200.

Once the *in-situ* growth of MONP within PEM was completed, samples were examined by X-ray diffraction (XRD) to confirm the presence of ZnO within the membranes. In Figure 7-4, one can observe that Nafion and Nexar do have the characteristic peaks of hexagonal lattice ZnO as they match the superposed peaks of reference bulk ZnO.

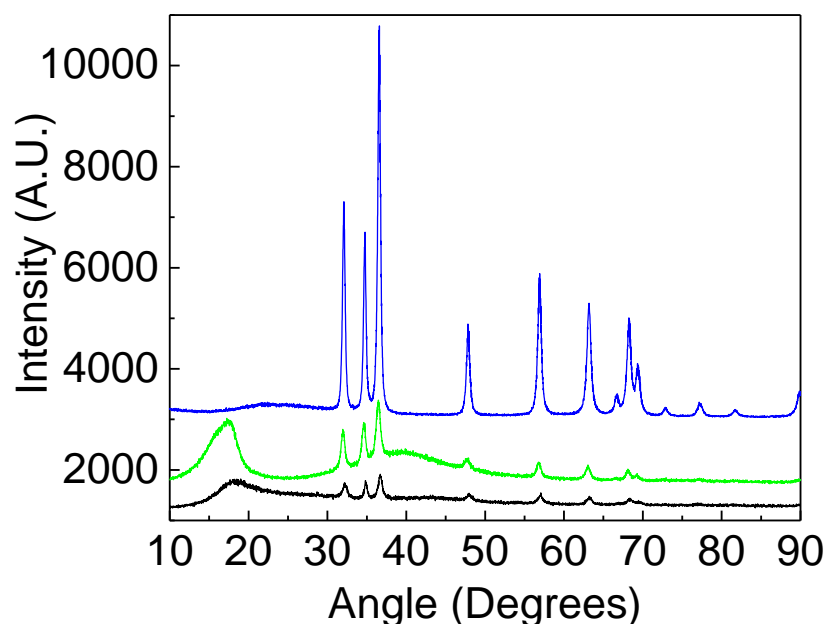


Figure 7-4. Wide angle x-ray diffractograms for Nexar-ZnO (black), Nafion-ZnO (green), and hexagonal-lattice bulk ZnO reference (blue).

ZnO nanoparticles range from 20 to 120 nm and have a rod-like elongated shape in Nexar-ZnO samples. Nafion-ZnO sample has much smaller nanoparticles with a PSD that

ranges from 10 to 40 nm. Although both PEM, Nafion and Nexar, were subjected to the same conditions for the *in-situ* growth of ZnO, it is clear that the microstructure of the polymer does play an important role. It is possible to use the PSD of MONP within these PEM as one design factor to help choose the appropriate PEM for the desired application.

A customized permeation setup was built to acquire *in-situ* Raman measurements of DMMP permeation through the PEM and PEM-MONP composites, Figure 7-5. The initial configuration comprises a 12 mL vial (top vial – donor compartment – depicted in Figure 7-5) with 10 mL of a 10 vol. % solution of DMMP is connected to a 2 mL (bottom vial – receiving compartment – depicted in Figure 7-5) vial that is completely full of water. Both vials are separated by the PEM studied and were tightly sealed to avoid leakage from any compartment. A 9 mm diameter sample of PEM was utilized for all permeation experiments. A 532 nm laser is used to radiate the small vial with water to detect the progression of DMMP permeation in the receiving compartment as a function of time.

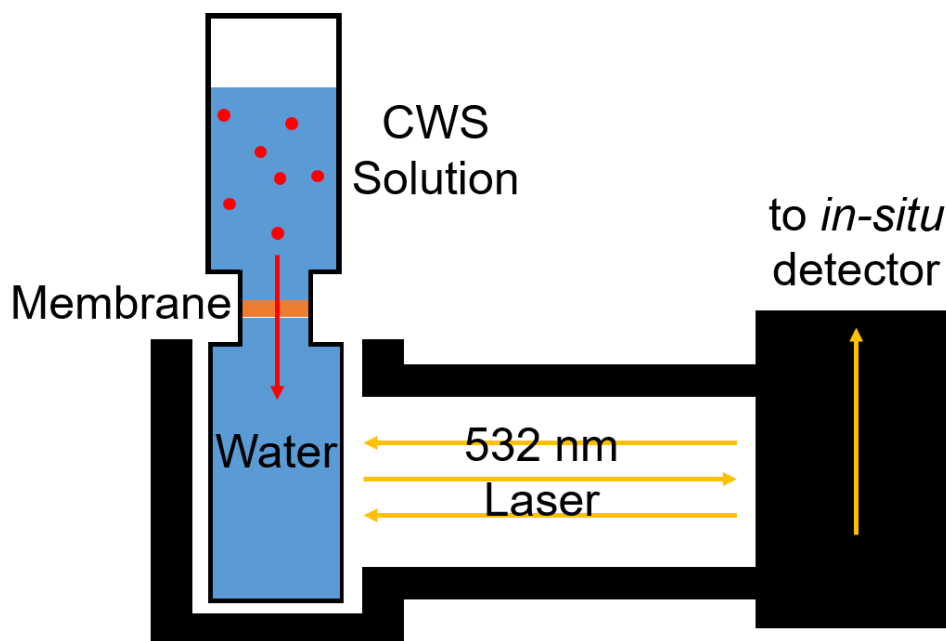


Figure 7-5. Experimental in-operando Raman spectroscopy setup for permeation cell.

A calibration curve, Figure 7-6, was developed for DMMP based on its peak located at 715 cm^{-1} , see Figure 7-6(a), associated with the P–C stretching mode $[(\text{P}-\text{CH}_3)]$ of DMMP.¹²³ The range of 680 to 745 cm^{-1} was used to calculate the mathematical area under the curve (AUC) at the aforementioned peak for the calibration curve. Figure 7-6(b) shows the calibration curve obtained from the AUC of DMMP spectra shown in Figure 7-6(a) and it shows a linear correlation with an R^2 of 0.999 over the entire range of DMMP concentrations studied.

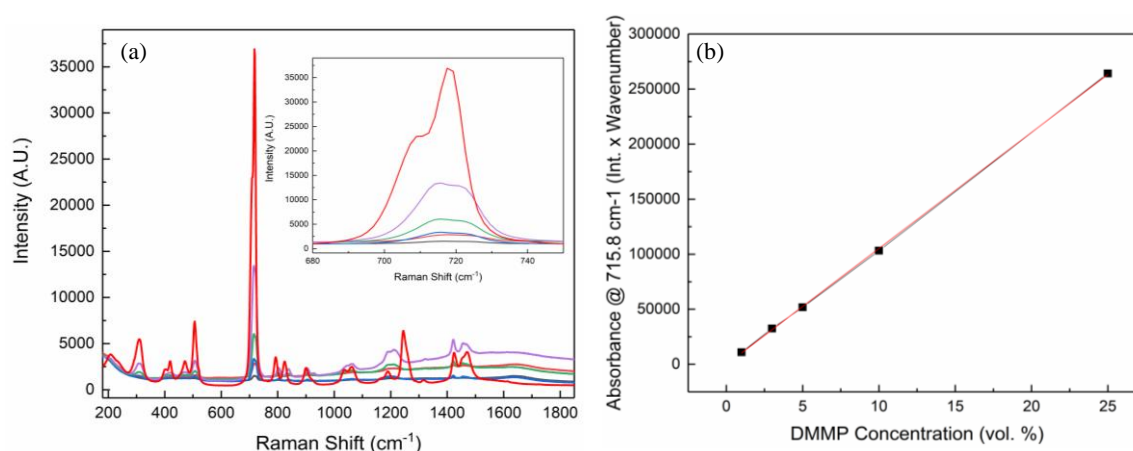


Figure 7-6. (a) Raman spectra for DMMP samples in solutions of varying concentrations: (gray) 1 vol.% DMMP, (orange) 3 vol.% DMMP, (blue) 5 vol.% DMMP, (green) 10 vol.% DMMP, (violet) 25 vol.% DMMP, (red) 100 vol.% DMMP. Inset shows a closer look at DMMP peak at 715 cm^{-1} . (b) Calibration curve for DMMP based on Raman spectra.

Figure 7-7 shows a three-dimensional representation of the evolution of the DMMP peak located at 715 cm^{-1} as a function of time. As it can be observed, the intensity of the peak at 715 cm^{-1} after one hour of permeation are most intense in the membranes without nanoparticles, Nafion- H^+ and Nexar- H^+ , and is the peak intensity is significantly less with the ZnO incorporated membranes. It is evident that the incorporation of nanoparticles does have a great influence over the permeation rate of DMMP across the PEM, as it is seen on both Nafion and Nexar cases. It is possible that the additional ZnO–DMMP may hinder

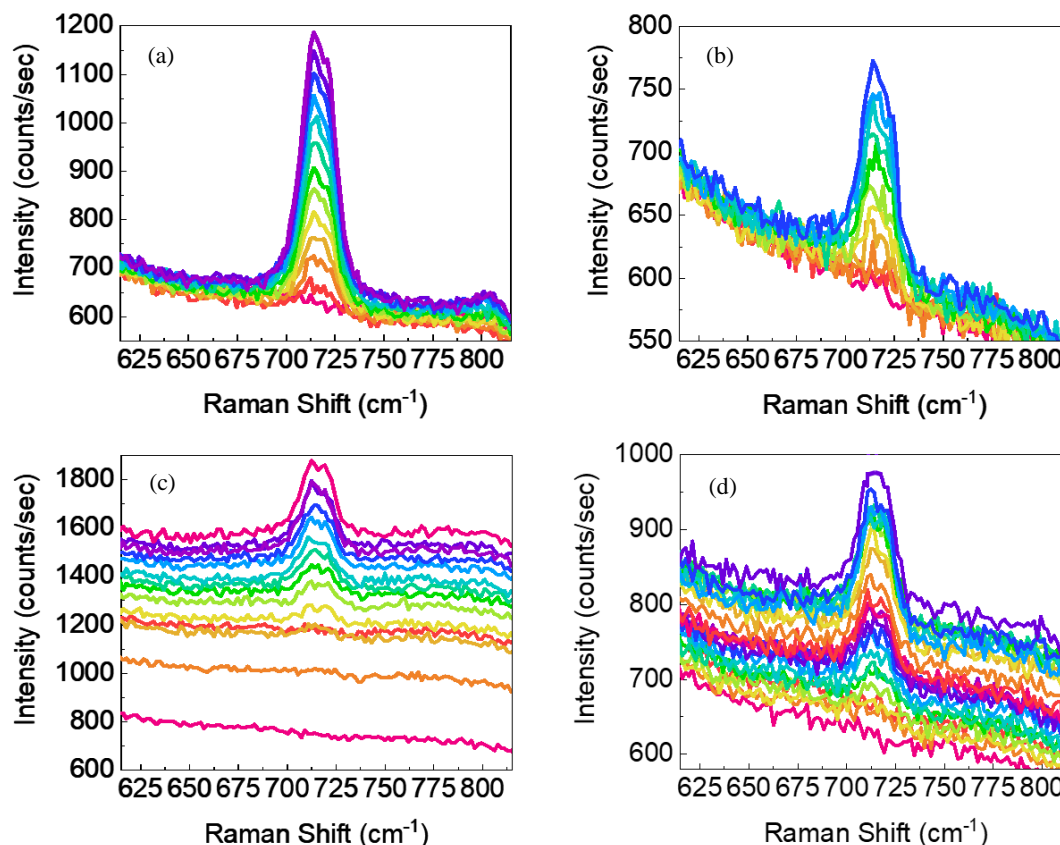


Figure 7-7. DMMP spectral evolution at peak located at 715 cm^{-1} as a function of time for DMMP permeation through: (a) Nafion- H^+ , (b) Nafion- ZnO , (c) Nexar- H^+ , (d) Nexar- ZnO .

DMMP diffusion as ZnO serves as attractive centers from which DMMP may be strongly adsorbed to, as it has been reported previously, DMMP strongly adsorbs to metal-oxide surfaces.⁴⁰ The reduced Signal/noise ratio in some of our measurements is due to the combination of the low concentration as well as fast acquisition time.

After performing a background subtraction and peak fitting for each spectra the AUC is calculated and later concentrations of permeated DMMP as a function of time are extracted from the calibration curve in Figure 7-6(b). When plotting the permeated DMMP concentration on the receiving compartment as a function of time, as in Figure 7-8, it can be seen that Nafion- H^+ has an observed breakthrough time, $t_{0,obs}$, defined as the time required to observe any DMMP in the receiving compartment, of 15 minutes when compared to Nafion- ZnO , which has a breakthrough time of 135 minutes. It takes 5 times

longer for DMMP to penetrate a Nafion-ZnO membrane when compared to its parental membrane, Nafion-H⁺. A similar behavior is shown with Nexar samples having a

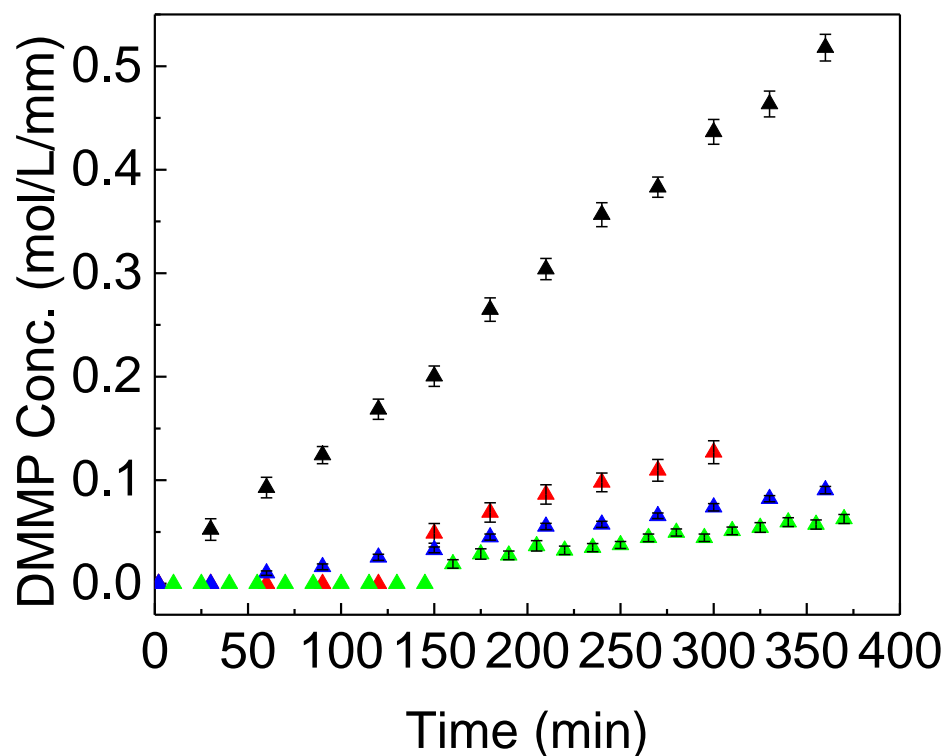


Figure 7-8. DMMP concentration in receiving compartment as a function of time through: (black triangles) Nafion-H⁺, (red triangles) Nafion-ZnO, (blue triangles) Nexar-H⁺, and (green triangles) Nexar-ZnO. Error bars are based on standard deviation from duplicate experiments.

breakthrough time of 45 and 145 minutes for Nexar-H⁺ and Nexar-ZnO, respectively. In addition, the permeation rate of Nafion-H⁺ is approximately 3, 5, and 7 times faster than Nafion-ZnO, Nexar-H⁺, and Nexar-ZnO, respectively.. In addition, the permeation rate of Nafion-H⁺ is ~3, 5, and 7 times faster than Nafion-ZnO, Nexar-H⁺, and Nexar-ZnO, respectively. These results show that the incorporation of ZnO nanoparticles has a large impact on both, breakthrough time and permeation rate in Nafion and Nexar samples.

DMMP permeation through PEM can be studied by using an approximate solution of the continuity equation for diffusion in a plane sheet geometry during early times¹²⁴:

$$C_B(t) = \frac{PC_{AA}}{V_{BL}}(t - t_0) \quad (7-1)$$

For boundary conditions: $C_A \gg C_B$, where C_A and C_B are the DMMP concentrations in the donating and receiving compartments, respectively. L is the membrane thickness, A is the cross-sectional area of the membrane, and P is the permeability coefficient for DMMP. DMMP permeability, P is defined as the product DK , where D is the DMMP diffusion coefficient, and K is the partition coefficient (ratio of DMMP concentration inside membrane and DMMP concentration in the donating compartment). The breakthrough time, t_0 , is defined as $\frac{L^2}{6D}$.

Data shown in Figure 7-8 could be fit to by using Equation 7-1 and transport properties could be extracted. However, Equation 1 is useful in the case when we have uniformity in membrane thickness, but in our case Nafion membrane thicknesses were approximately 190 μm , while Nexar membranes were approximately 500 μm thick. Therefore, a useful rearrangement of Equation 1 can be done to take into account membrane thickness differences as written in Equation 2. By rearranging Eq. (7-1) to:

$$\frac{C_B(t)V_B L}{C_A A} = P \left(t - \frac{L^2}{6D} \right) \quad (7-2)$$

When plotting data from Figure 7-8 using Equation 7-2, the rearranged permeation profiles result in data shown in Figure 7-9. This way we can make a more fair comparison between samples and get a more accurate picture of the permeation dynamics. From the observed breakthrough time, $t_{0,obs}$, from Figure 7-8, DMMP diffusivity coefficients were calculated by using the definition of $t_{0,obs} = \frac{L^2}{6D}$. Calculations of the slope of the curves in Figure 7-9 give the permeability constant, P , from which the partition coefficients were calculated. Extracted transport parameters are tabulated in Table 1. Linear fits of

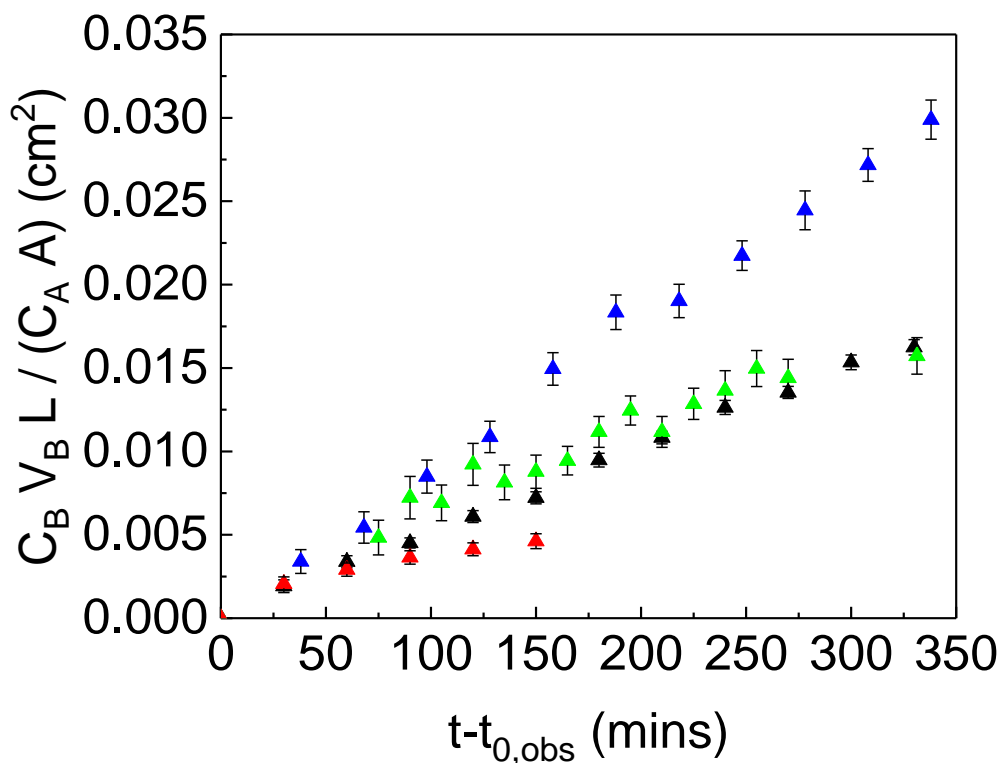


Figure 7-9. Rearranged DMMP permeation as expressed in Equation 2: (black triangles) Nafion-H⁺, (red triangles) Nafion-ZnO, (blue triangles) Nexar-H⁺, and (green triangles) Nexar-ZnO. Error bars are based on standard deviation from duplicate experiments.

permeation curves in Figure 6 had excellent agreement with an R^2 of 0.99, for the exception of Nexar-H⁺, which had an R^2 of 0.96.

Table 7-1. List of transport properties of DMMP across PEM studied

	$P \text{ (cm}^2\text{/s)} \times 10^7$	$t_{0,obs}^a \text{ (min)}$
Nafion-H⁺	8.23	15
Nafion-ZnO	2.84	135
Nexar-H⁺	14.80	45
Nexar-ZnO	7.90	145

^a Measurements have an uncertainty of ± 15 minutes

Of all samples studied, Nafion-ZnO seems to have the best blocking properties against DMMP permeation in liquid phase as it is among the samples with the largest

observed breakthrough time, ~150 min, and slowest permeation rate, $P = 2.84 \times 10^{-7} \text{ cm}^2/\text{s}$, after breakthrough.

A novel *in-situ* Raman spectroscopy setup is built to measure agent permeation across protective barriers and applied to study DMMP permeation through ZnO loaded Nafion and Nexar polyelectrolyte membranes. It is shown that, incorporation of ZnO nanoparticles increases the breakthrough time and reduces the agent permeability, providing better protective capabilities of composite membranes.

CHAPTER 8. Conclusions and Recommendations on Future Research

In the the preceeding chapters it was shown that growing MONP within polyelectrolyte membranes successfully through an *in situ* generation of MONP procedure was possible. It was shown that the size and morphology of *in situ* grown MONPs can be controlled through the use of binary water-alcohol solvents of different composition. The ability to tailor the MONP size and crystallinity during the *in situ* growth has far reaching implications in catalysis and optoelectronics, as well as in applications for sensors and chemical protection. The incorporation of MONP within PEM substrates not only reinforces the composite material mechanically, but also thermally in quite significant amounts.

Effective surface-modified metal-oxides were synthesized by performing a simple H₂O₂ treatment. Beneficial physical and chemical changes occur within metal-oxide surfaces that improve their decomposition of CWA simulants. Some observed changes include the formation of mesoporosity and reactive surface moieties that enhance agent decomposition.

In addition, photo-active POM were synthesized and their reactivity against H-agent simulant occurs through various and complex photo-catalytic and photo-oxidative pathways with the formation of numerous products. Moreover, POM nanoaggregates exhibit multi-functionality, as they show an ability to gradually change color during the exposure to the toxic in addition to their reactivity. This means that POM could be used as CWA sensors for the monitoring of the protection media exhaustion level.

Water and DMMP sorption experiments indicate the suitability of the developed MONP-PEM composites as barriers against harmful substances. On another note, a novel

and inexpensive permeation device was built with an *in-situ* Raman spectroscopy experimental setup that was capable of measuring DMMP permeation across PEM and PEM composites allowing for the real-time testing of MONP-PEM composites protective performance against the permeation of harmful substances.

Some ideas on future directions related to the decomposition of CWA include:

- In-depth analysis of the interaction between membrane substrates and agents to understand how to design more efficient protective materials.
- The testing of the fully-assembled multi-catalyst polyelectrolyte system we designed against the simultaneous exposure of G-agent and H-agent to observe its protective performance against the agents.
- More in-depth analysis of transport phenomena occurring at the membrane-air interface when an agent is in contact with the protective material.
- A route for commercialization of the technology developed in this dissertation.

Preparations for manuscript submissions that were discussed in this dissertation are ongoing. A patent application has been filed, in which the provisional patent application has been granted, regarding the development of a multi-catalyst polyelectrolyte membrane composite material.

Bibliography

1. Ganesan, K.; Raza, S. K.; Vijayaraghavan, R., Chemical Warfare Agents. *Journal of Pharmacy and Bioallied Sciences* **2010**, 2, 166-178.
2. Li, Y. X.; Klabunde, K. J., Nanoscale Metal Oxide Particles as Chemical Reagents. Destructive Adsorption of a Chemical Agent Simulant, Dimethyl Methylphosphonate, on Heat-Treated Magnesium Oxide. *Langmuir* **1991**, 7, 1388-1393.
3. Li, Y. X.; Koper, O.; Atteya, M.; Klabunde, K. J., Adsorption and Decomposition of Organophosphorus Compounds on Nanoscale Metal Oxide Particles. In Situ Gc-MS Studies of Pulsed Microreactions over Magnesium Oxide. *Chem. Mater.* **1992**, 4 (323-330).
4. Koper, O.; Lucas, E.; Klabunde, K. J., Development of Reactive Topical Skin Protectants against Sulfur Mustard and Nerve Agents. *J. Appl. Toxicol.* **1999**, 19, S59-S70.
5. Lucas, E.; Decker, S.; Khaleel, A.; Seitz, A.; Fultz, S.; Ponce, A.; Li, W.; Carnes, C.; Klabunde, K. J., Nanocrystalline Metal Oxides as Unique Chemical Reagents/Sorbents. *Chem. Eur. J.* **2001**, 7 (12), 2505-2510.
6. Mahato, T. H.; Prasad, G. K.; Singh, B.; Acharya, J.; Srivastava, A. R.; Vijayaraghavan, R., Nanocrystalline Zinc Oxide for the Decontamination of Sarin. *J Hazard Mater* **2009**, 165 (1-3), 928-32.
7. Nazari, B.; Jaafari, M., A New Method for the Synthesis of Mgo Nanoparticles for the Destructive Adsorption of Organo-Phosphorus Compounds. *Digest J. of Nanomaterials and Biostructures* **2010**, 5 (4), 909-917.
8. Bandosz, T. J.; Laskoski, M.; Mahle, J.; Mogilevsky, G.; Peterson, G. W.; Rossin, J. A.; Wagner, G. W., Reactions of Vx, Gd, and Hd with Zr(OH)₄: Near Instantaneous

Decontamination of Vx. *The Journal of Physical Chemistry C* **2012**, 116 (21), 11606-11614.

9. Janoš, P.; Kuráň, P.; Pilařová, V.; Trögl, J.; Šťastný, M.; Pelant, O.; Henych, J.; Bakardjieva, S.; Životský, O.; Kormunda, M.; Mazanec, K.; Skoumal, M., Magnetically Separable Reactive Sorbent Based on the CeO₂/Ti-Fe₂O₃ Composite and Its Utilization for Rapid Degradation of the Organophosphate Pesticide Parathion Methyl and Certain Nerve Agents. *Chemical Engineering Journal* **2015**, 262, 747-755.

10. Cojocaru, B.; Neatu, S.; Parvulescu, V. I.; Somoghi, V.; Petrea, N.; Epure, G.; Alvaro, M.; Garcia, H., Synergism of Activated Carbon and Undoped and Nitrogen-Doped TiO₂ in the Photocatalytic Degradation of the Chemical Warfare Agents Soman, Vx, and Yperite. *ChemSusChem* **2009**, 2 (5), 427-36.

11. Naseri, M. T.; Sarabadani, M.; Ashrafi, D.; Saeidian, H.; Babri, M., Photoassisted and Photocatalytic Degradation of Sulfur Mustard Using TiO₂ Nanoparticles and Polyoxometalates. *Environ Sci Pollut Res Int* **2013**, 20 (2), 907-16.

12. Prasad, G. K., Silver Ion Exchanged Titania Nanotubes for Decontamination of 2 Chloro Ethyl Phenyl Sulphide and Dimethyl Methyl Phosphonate. *J. Sci. Ind. Res.* **2009**, 68, 379-384.

13. Prasad, G. K.; Singh, B.; Ganesan, K.; Batra, A.; Kumeria, T.; Gutch, P. K.; Vijayaraghavan, R., Modified Titania Nanotubes for Decontamination of Sulphur Mustard. *J Hazard Mater* **2009**, 167 (1-3), 1192-7.

14. Han, S.; Zhang, G.; Xi, H.; Xu, D.; Fu, X.; Wang, X., Sulfated TiO₂ Decontaminate 2-Ceas and Dmmp in Vapor Phase. *Catalysis Letters* **2007**, 122 (1-2), 106-110.

15. Kozlov, D. V.; Vorontsov, A. V.; Smirniotis, P. G.; Savinov, E. N., Gas-Phase Photocatalytic Oxidation of Diethyl Sulfide over TiO_2 : Kinetic Investigations and Catalyst Deactivation. *Applied Catalysis B: Environmental* **2003**, *42* (1), 77-87.
16. Moss, J. A.; Szczepankiewicz, S. H.; Park, E.; Hoffman, M. R., Adsorption and Photodegradation of Dimethyl Methylphosphonate Vapor at TiO_2 Surfaces. *J. Phys. Chem. B* **2005**, *109*, 19779-19785.
17. Neațu, Ș.; Pârvulescu, V. I.; Epure, G.; Petrea, N.; Șomoghi, V.; Ricchiardi, G.; Bordiga, S.; Zecchina, A., M/ TiO_2 / SiO_2 (M=Fe, Mn, and V) Catalysts in Photo-Decomposition of Sulfur Mustard. *Applied Catalysis B: Environmental* **2009**, *91* (1-2), 546-553.
18. Vorontsov, A. V.; Chen, Y. C.; Smirniotis, P. G., Photocatalytic Oxidation of Vx Simulant 2-(Butylamino)Ethanethiol. *J Hazard Mater* **2004**, *113* (1-3), 89-95.
19. Buru, C. T.; Li, P.; Mehdi, B. L.; Dohnalkova, A.; Platero-Prats, A. E.; Browning, N. D.; Chapman, K. W.; Hupp, J. T.; Farha, O. K., Adsorption of a Catalytically Accessible Polyoxometalate in a Mesoporous Channel-Type Metal–Organic Framework. *Chemistry of Materials* **2017**, *29* (12), 5174-5181.
20. Katz, M. J.; Mondloch, J. E.; Totten, R. K.; Park, J. K.; Nguyen, S. T.; Farha, O. K.; Hupp, J. T., Simple and Compelling Biomimetic Metal-Organic Framework Catalyst for the Degradation of Nerve Agent Simulants. *Angew Chem Int Ed Engl* **2014**, *53* (2), 497-501.
21. Katz, M. J.; Moon, S.-Y.; Mondloch, J. E.; Beyzavi, M. H.; Stephenson, C. J.; Hupp, J. T.; Farha, O. K., Exploiting Parameter Space in Mofs: A 20-Fold Enhancement of Phosphate-Ester Hydrolysis with UiO-66-NH_2 . *Chem. Sci.* **2015**, *6* (4), 2286-2291.

22. Mondloch, J. E.; Katz, M. J.; Isley, W. C., 3rd; Ghosh, P.; Liao, P.; Bury, W.; Wagner, G. W.; Hall, M. G.; DeCoste, J. B.; Peterson, G. W.; Snurr, R. Q.; Cramer, C. J.; Hupp, J. T.; Farha, O. K., Destruction of Chemical Warfare Agents Using Metal-Organic Frameworks. *Nat Mater* **2015**, *14* (5), 512-6.
23. Moon, S. Y.; Liu, Y.; Hupp, J. T.; Farha, O. K., Instantaneous Hydrolysis of Nerve-Agent Simulants with a Six-Connected Zirconium-Based Metal-Organic Framework. *Angew Chem Int Ed Engl* **2015**, *54* (23), 6795-9.
24. Moon, S. Y.; Wagner, G. W.; Mondloch, J. E.; Peterson, G. W.; DeCoste, J. B.; Hupp, J. T.; Farha, O. K., Effective, Facile, and Selective Hydrolysis of the Chemical Warfare Agent Vx Using Zr₆-Based Metal-Organic Frameworks. *Inorg Chem* **2015**, *54* (22), 10829-33.
25. Peterson, G. W.; Moon, S. Y.; Wagner, G. W.; Hall, M. G.; DeCoste, J. B.; Hupp, J. T.; Farha, O. K., Tailoring the Pore Size and Functionality of Uio-Type Metal-Organic Frameworks for Optimal Nerve Agent Destruction. *Inorg Chem* **2015**, *54* (20), 9684-6.
26. Giles, S. L.; Lundin, J. G.; Balow, R. B.; Pehrsson, P. E.; Wynne, J. H., Comparative Roles of Zr⁴⁺ and Ni²⁺ Wells-Dawson Hetero-Metal Substituted Polyoxometalates on Oxidation of Chemical Contaminants. *Applied Catalysis A: General* **2017**, *542*, 306-310.
27. Mizrahi, D. M.; Saphier, S.; Columbus, I., Efficient Heterogeneous and Environmentally Friendly Degradation of Nerve Agents on a Tungsten-Based Pom. *J Hazard Mater* **2010**, *179* (1-3), 495-9.
28. Wu, K. H.; Yu, P. Y.; Yang, C. C.; Wang, G. P.; Chao, C. M., Preparation and Characterization of Polyoxometalate-Modified Poly(Vinyl Alcohol)/Polyethyleneimine

Hybrids as a Chemical and Biological Self-Detoxifying Material. *Polymer Degradation and Stability* **2009**, *94* (9), 1411-1418.

29. Johnson, R. P.; Hill, C. L., Polyoxometalate Oxidation of Chemical

Warfare Agent Simulants in Fluorinated

Media. *J. Appl. Toxicol.* **1999**, *19*, S71-S75.

30. Sharma, N.; Kakkar, R., Adsorption of Sarin on Mgo Nanotubes: Role of Doped and Defect Sites. *Journal of Computational Science* **2015**, *10*, 225-236.

31. Vernekar, A. A.; Das, T.; Mugesh, G., Vacancy-Engineered Nanocerria: Enzyme Mimetic Hotspots for the Degradation of Nerve Agents. *Angew. Chem. Int. Ed.* **2016**, *55*, 1412-1416.

32. Tang, H.; Cheng, Z.; Zhu, H.; Zuo, G.; Zhang, M., Effect of Acid and Base Sites on the Degradation of Sulfur Mustard over Several Typical Oxides. *Applied Catalysis B: Environmental* **2008**, *79* (4), 323-333.

33. Singh, B.; Mahato, T. H.; Srivastava, A. K.; Prasad, G. K.; Ganesan, K.; Vijayaraghavan, R.; Jain, R., Significance of Porous Structure on Degradatin of 2,2' Dichloro Diethyl Sulphide and 2 Chloroethyl Ethyl Sulphide on the Surface of Vanadium Oxide Nanostructure. *J Hazard Mater* **2011**, *190* (1-3), 1053-7.

34. Zafrani, Y.; Yehezkel, L.; Goldvaser, M.; Marciano, D.; Waysbort, D.; Gershonov, E.; Columbus, I., The Reactivity of Quaternary Ammonium- Versus Potassium-Fluorides Supported on Metal Oxides: Paving the Way to an Instantaneous Detoxification of Chemical Warfare Agents. *Org Biomol Chem* **2011**, *9* (24), 8445-51.

35. Naseri, M. T.; Sarabadani, M.; Ashrafi, D.; Saeidian, H.; Babri, M., Photoassisted and Photocatalytic Degradation of Sulfur Mustard Using TiO_2 Nanoparticles and Polyoxometalates. *Environ. Sci. Pollut. Res.* **20** (2), 907-916.
36. Mahato, T. H.; Prasad, G. K.; Singh, B.; Acharya, J.; Srivastava, A. R.; Vijayaraghavan, R., Nanocrystalline Zinc Oxide for the Decontamination of Sarin. *Journal of Hazardous Materials* **2009**, *165* (1-3), 928-932.
37. Kumar, J. P.; Prasad, G. K.; Ramacharyulu, P.; Garg, P.; Ganesan, K., Mesoporous Cuo-Zno Binary Metal Oxide Nanocomposite for Decontamination of Sulfur Mustard. *Mater. Chem. Phys.* **142** (2-3), 484-490.
38. Wagner, G. W.; Procell, L. R.; O'Connor, R. J.; Munavalli, S.; Carnes, C. L.; Kapoor, P. N.; Klabunde, K. J., Reactions of Vx , Gb, Gd, and Hd with Nanosize Al_2O_3 . Formation of Aluminophosphonates. *J. Am. Chem. Soc.* **2001**, *123* (8), 1636-1644.
39. Wagner, G. W.; Koper, O. B.; Lucas, E.; Decker, S.; Klabunde, K. J., Reactions of Vx , Gd, and Hd with Nanosize Cao: Autocatalytic Dehydrohalogenation of Hd. *J. Phys. Chem. B* **2000**, *104* (21), 5118-5123.
40. Sundarrajan, S.; Ramakrishna, S., Fabrication of Nanocomposite Membranes from Nanofibers and Nanoparticles for Protection against Chemical Warfare Stimulants. *Journal of Materials Science* **2007**, *42* (20), 8400-8407.
41. Panayotov, D. A.; Morris, J. R., Thermal Decomposition of a Chemical Warfare Agent Simulant (Dmmp) on TiO_2 : Adsorbate Reactions with Lattice Oxygen as Studied by Infrared Spectroscopy. *Journal of Physical Chemistry C* **2009**, *113* (35), 15684-15691.

42. Mitchell, M. B.; Sheinker, V. N.; Cox, W. W.; Hardcastle, K., Sustained Room Temperature Decomposition of Dimethyl Methylphosphonate (Dmmp) by O-3 on Alumina-Supported MnO₂. *J. Phys. Chem. C* **115** (23), 11514-11524.
43. Vernekar, A. A.; Das, T.; Mughesh, G., Vacancy-Engineered Nanocerium: Enzyme Mimetic Hotspots for the Degradation of Nerve Agents. *Angew. Chem.-Int. Edit.* **55** (4), 1412-1416.
44. Bandosz, T. J.; Laskoski, M.; Mahle, J.; Mogilevsky, G.; Peterson, G. W.; Rossin, J. A.; Wagner, G. W., Reactions of VX, GD, and HD with Zr(OH)₄: Near Instantaneous Decontamination of VX. *Journal of Physical Chemistry C* **116** (21), 11606-11614.
45. Stengl, V.; Matys Grygar, T.; Bludská, J.; Oplustil, F.; Nemec, T., Mesoporous Iron-Manganese Oxides for Sulphur Mustard and Soman Degradation. *Mater. Res. Bull.* **47** (12), 4291-4299.
46. Nagarapu, L.; Apuri, S.; Kantevari, S., Potassium Dodecatungstocobaltate Trihydrate (K₅CoW₁₂O₄₀·3H₂O): A Mild and Efficient Reusable Catalyst for the One-Pot Synthesis of 1,2,4,5-Tetrasubstituted Imidazoles under Conventional Heating and Microwave Irradiation. *Journal of Molecular Catalysis A: Chemical* **2007**, *266* (1-2), 104-108.
47. Nagarapu, L.; Kantevari, S.; Mahankhali, V. C.; Apuri, S., Potassium Dodecatungstocobaltate Trihydrate (K₅CoW₁₂O₄₀·3H₂O): A Mild and Efficient Reusable Catalyst for the Synthesis of Aryl-14H-Dibenzo[A,J]Xanthenes under Conventional Heating and Microwave Irradiation. *Catalysis Communications* **2007**, *8* (8), 1173-1177.

48. Rafiee, E.; Tork, F.; Joshaghani, M., Heteropoly Acids as Solid Green Bronsted Acids for a One-Pot Synthesis of Beta-Acetamido Ketones by Dakin-West Reaction. *Bioorg Med Chem Lett* **2006**, *16* (5), 1221-6.
49. Natali, M.; Bazzan, I.; Goberna-Ferrón, S.; Al-Oweini, R.; Ibrahim, M.; Bassil, B. S.; Dau, H.; Scandola, F.; Galán-Mascarós, J. R.; Kortz, U.; Sartorel, A.; Zaharieva, I.; Bonchio, M., Photo-Assisted Water Oxidation by High-Nuclearity Cobalt-Oxo Cores: Tracing the Catalyst Fate During Oxygen Evolution Turnover. *Green Chem.* **2017**, *19* (10), 2416-2426.
50. Song, F.; Ding, Y.; Ma, B.; Wang, C.; Wang, Q.; Du, X.; Fu, S.; Song, J., K7[Co₁₁(H₂O)₁₁W₁₀P₃]: A Molecular Mixed-Valence Keggin Polyoxometalate Catalyst of High Stability and Efficiency for Visible Light-Driven Water Oxidation. *Energy & Environmental Science* **2013**, *6* (4), 1170.
51. Pathan, S.; Patel, A., Solvent Free Clean Selective Oxidation of Alcohols Catalyzed by Mono Transition Metal (Co, Mn, Ni)-Substituted Keggin-Phosphomolybdates Using Hydrogen Peroxide. *Applied Catalysis A: General* **2013**, *459*, 59-64.
52. Johnson, R. P.; Hill, C. L., Polyoxometalate Oxidation of Chemical Warfare Agent Simulants in Fluorinated Media. *J. Appl. Toxicol.* **1999**, *19*, S71-S75.
53. Han, Q.; He, C.; Zhao, M.; Qi, B.; Niu, J.; Duan, C., Engineering Chiral Polyoxometalate Hybrid Metal-Organic Frameworks for Asymmetric Dihydroxylation of Olefins. *J Am Chem Soc* **2013**, *135* (28), 10186-9.
54. Hao, X. L.; Ma, Y. Y.; Zang, H. Y.; Wang, Y. H.; Li, Y. G.; Wang, E. B., A Polyoxometalate-Encapsulating Cationic Metal-Organic Framework as a Heterogeneous Catalyst for Desulfurization. *Chemistry* **2015**, *21* (9), 3778-84.

55. Liu, Y.; Liu, S.; He, D.; Li, N.; Ji, Y.; Zheng, Z.; Luo, F.; Liu, S.; Shi, Z.; Hu, C., Crystal Facets Make a Profound Difference in Polyoxometalate-Containing Metal-Organic Frameworks as Catalysts for Biodiesel Production. *J Am Chem Soc* **2015**, *137* (39), 12697-703.
56. Yang, X. Y.; Wei, T.; Li, J. S.; Sheng, N.; Zhu, P. P.; Sha, J. Q.; Wang, T.; Lan, Y. Q., Polyoxometalate-Incorporated Metallapillararene/Metallacalixarene Metal-Organic Frameworks as Anode Materials for Lithium Ion Batteries. *Inorg Chem* **2017**, *56* (14), 8311-8318.
57. Armatas, G. S.; Katsoulidis, A. P.; Petrakis, D. E.; Pomonis, P. J.; Kanatzidis, M. G., Nanocasting of Ordered Mesoporous Co₃O₄-Based Polyoxometalate Composite Frameworks. *Chemistry of Materials* **2010**, *22* (20), 5739-5746.
58. Lan, Q.; Zhang, Z. M.; Qin, C.; Wang, X. L.; Li, Y. G.; Tan, H. Q.; Wang, E. B., Highly Dispersed Polyoxometalate-Doped Porous Co₃O₄ Water Oxidation Photocatalysts Derived from Pom@Mof Crystalline Materials. *Chemistry* **2016**, *22* (43), 15513-15520.
59. Saux, C.; Marchena, C. L.; Pizzio, L. R.; Pierella, L. B., Dodecatungstocobaltate Supported over Zsm-5 Zeolite as Novel Solid Catalyst in Selective Sulfide Oxidation. *Journal of Porous Materials* **2016**, *23* (4), 947-956.
60. Song, X.; Zhu, W.; Yan, Y.; Gao, H.; Gao, W.; Zhang, W.; Jia, M., Triphenylamine-Based Porous Organic Polymers: Synthesis and Application for Supporting Phosphomolybdate to Fabricate Efficient Olefin Oxidation Catalysts. *Microporous and Mesoporous Materials* **2017**, *242*, 9-17.
61. Gao, G.-G.; Xu, L.; Wang, W.-J.; Qu, X.-S.; Liu, H.; Yang, Y.-Y., Cobalt(II)/Nickel(II)-Centered Keggin-Type Heteropolymolybdates: Syntheses, Crystal

Structures, Magnetic and Electrochemical Properties. *Inorg. Chem.* **2008**, 47 (7), 2325-2333.

62. Kinnan, M. K.; Creasy, W. R.; Fullmer, L. B.; Schreuder-Gibson, H. L.; Nyman, M., Nerve Agent Degradation with Polyoxoniobates. *European Journal of Inorganic Chemistry* **2014**, 2014 (14), 2361-2367.

63. Guo, W.; Bacsá, J.; van Leusen, J.; Sullivan, K. P.; Lv, H.; Kogerler, P.; Hill, C. L., A Layered Manganese(IV)-Containing Heteropolyvanadate with a 1:14 Stoichiometry. *Inorg Chem* **2015**, 54 (22), 10604-9.

64. Liu, F.; Lu, Q. F.; Jiao, X. L.; Chen, D. R., Fabrication of Nylon-6/Poms Nanofibrous Membranes and the Degradation of Mustard Stimulant Research. *RSC Adv.* 4 (78), 41271-41276.

65. Mizrahi, D. M.; Saphier, S.; Columbus, I., Efficient Heterogeneous and Environmentally Friendly Degradation of Nerve Agents on a Tungsten-Based Pom. *J. Hazard. Mater.* 179 (1-3), 495-499.

66. Okun, N. M.; Tarr, J. C.; Hilleshiem, D. A.; Zhang, L.; Hardcastle, K. I.; Hill, C. L., Highly Reactive Catalysts for Aerobic Thioether Oxidation - the Fe-Substituted Polyoxometalate/Hydrogen Dinitrate System. *Journal of Molecular Catalysis a-Chemical* **2006**, 246 (1-2), 11-17.

67. Guo, W. W.; Bacsá, J.; van Leusen, J.; Sullivan, K. P.; Lv, H. J.; Kogerler, P.; Hill, C. L., A Layered Manganese(IV)-Containing Heteropolyvanadate with a 1:14 Stoichiometry. *Inorg. Chem.* 54 (22), 10604-10609.

68. Giannakoudakis, D. A.; Colon-Ortiz, J.; Landers, J.; Murali, S.; Florent, M.; Neimark, A. V.; Bandosz, T. J., Polyoxometalate Hybrid Catalyst for Detection and

Photodecomposition of Mustard Gas Surrogate Vapors. *Applied Surface Science* **2019**, 467, 428-438.

69. Lopez-Maya, E.; Montoro, C.; Rodriguez-Albelo, L. M.; Aznar Cervantes, S. D.; Lozano-Perez, A. A.; Cenis, J. L.; Barea, E.; Navarro, J. A., Textile/Metal-Organic-Framework Composites as Self-Detoxifying Filters for Chemical-Warfare Agents. *Angew Chem Int Ed Engl* **2015**, 54 (23), 6790-4.

70. Katz, M. J.; Moon, S. Y.; Mondloch, J. E.; Beyzavi, M. H.; Stephenson, C. J.; Hupp, J. T.; Farha, O. K., Exploiting Parameter Space in Mofs: A 20-Fold Enhancement of Phosphate-Ester Hydrolysis with UiO-66-Nh₂. *Chemical Science* **2015**, 6 (4), 2286-2291.

71. Li, P.; Klet, R. C.; Moon, S. Y.; Wang, T. C.; Deria, P.; Peters, A. W.; Klahr, B. M.; Park, H. J.; Al-Juaid, S. S.; Hupp, J. T.; Farha, O. K., Synthesis of Nanocrystals of Zr-Based Metal-Organic Frameworks with Csq-Net: Significant Enhancement in the Degradation of a Nerve Agent Simulant. *Chem Commun (Camb)* **2015**, 51 (54), 10925-8.

72. Lopez-Maya, E.; Montoro, C.; Rodriguez-Albelo, L. M.; Cervantes, S. D. A.; Lozano-Perez, A. A.; Cenis, J. L.; Barea, E.; Navarro, J. A. R., Textile/Metal-Organic-Framework Composites as Self-Detoxifying Filters for Chemical-Warfare Agents. *Angew. Chem.-Int. Edit.* 54 (23), 6790-6794.

73. Roy, A.; Srivastava, A. K.; Singh, B.; Shah, D.; Mahato, T. H.; Gutch, P. K.; Halve, A. K., Degradation of Sarin, Declp and Decnp over Cu-Btc Metal Organic Framework. *J. Porous Mat.* 20 (5), 1103-1109.

74. Bromberg, L.; Klichko, Y.; Chang, E. P.; Speakman, S.; Straut, C. M.; Wilusz, E.; Hatton, T. A., Alkylaminopyridine-Modified Aluminum Aminoterephthalate Metal-

Organic Frameworks as Components of Reactive Self-Detoxifying Materials. *ACS Appl. Mater. Interfaces* 4 (9), 4595-4602.

75. Nunes, P.; Gomes, A. C.; Pillinger, M.; Goncalves, I. S.; Abrantes, M., Promotion of Phosphoester Hydrolysis by the Zr-IV-Based Metal-Organic Framework Uio-67. *Microporous Mesoporous Mat.* 208, 21-29.

76. Mondloch, J. E.; Katz, M. J.; Isley, W. C.; Ghosh, P.; Liao, P. L.; Bury, W.; Wagner, G.; Hall, M. G.; DeCoste, J. B.; Peterson, G. W.; Snurr, R. Q.; Cramer, C. J.; Hupp, J. T.; Farha, O. K., Destruction of Chemical Warfare Agents Using Metal-Organic Frameworks. *Nat. Mater.* 14 (5), 512-516.

77. Liu, Y.; Moon, S. Y.; Hupp, J. T.; Farha, O. K., Dual-Function Metal-Organic Framework as a Versatile Catalyst for Detoxifying Chemical Warfare Agent Simulants. *ACS Nano* 9 (12), 12358-12364.

78. Montoro, C.; Linares, F.; Procopio, E. Q.; Senkovska, I.; Kaskel, S.; Galli, S.; Masciocchi, N.; Barea, E.; Navarro, J. A., Capture of Nerve Agents and Mustard Gas Analogues by Hydrophobic Robust Mof-5 Type Metal-Organic Frameworks. *J Am Chem Soc* 2011, 133 (31), 11888-91.

79. Katz, M. J.; Klet, R. C.; Moon, S. Y.; Mondloch, J. E.; Hupp, J. T.; Farha, O. K., One Step Backward Is Two Steps Forward: Enhancing the Hydrolysis Rate of Uio-66 by Decreasing [OH⁻]. *ACS Catal.* 5 (8), 4637-4642.

80. Liu, Y. Y.; Howarth, A. J.; Hupp, J. T.; Farha, O. K., Selective Photooxidation of a Mustard-Gas Simulant Catalyzed by a Porphyrinic Metal-Organic Framework. *Angew. Chem.-Int. Edit.* 54 (31), 9001-9005.

81. Peterson, G. W.; Moon, S. Y.; Wagner, G. W.; Hall, M. G.; DeCoste, J. B.; Hupp, J. T.; Farha, O. K., Tailoring the Pore Size and Functionality of Uio-Type Metal-Organic Frameworks for Optimal Nerve Agent Destruction. *Inorg. Chem.* **54** (20), 9684-9686.
82. McCarthy, D. L.; Liu, J.; Dwyer, D. B.; Troiano, J. L.; Boyer, S. M.; DeCoste, J. B.; Bernier, W. E.; Jones, J. W. E., Electrospun Metal–Organic Framework Polymer Composites for the Catalytic Degradation of Methyl Paraoxon. *New J. Chem.* **2017**.
83. Peterson, G. W.; Wagner, G. W., Detoxification of Chemical Warfare Agents by Cubtc. *Journal of Porous Materials* **2013**, *21* (2), 121-126.
84. Cojocaru, B.; Parvulescu, V. I.; Preda, E.; Iepure, G.; Somoghi, V.; Carbonell, E.; Alvaro, M.; Garcia, H., Sensitizers on Inorganic Carriers for Decomposition of the Chemical Warfare Agent Yperite. *Environ. Sci. Technol.* **2008**, *42*, 4908-4913.
85. Kanyi, C. W.; Doetschman, D. C.; Schulte, J. T., Nucleophilic Chemistry of X-Type Faujasite Zeolites with 2-Chloroethyl Ethyl Sulfide (Cees), a Simulant of Common Mustard Gas. *Microporous and Mesoporous Materials* **2009**, *124* (1-3), 232-235.
86. Kanyi, C. W.; Doetschman, D. C.; Yang, S.-W.; Schulte, J. T., The Nucleophilic Chemical Reactions of Nax Faujasite Zeolite with Diisopropyl Phosphorofluoridate (Diisopropyl Fluorophosphate, Dfp). *Microporous and Mesoporous Materials* **2009**, *119* (1-3), 23-29.
87. Wagner, G. W.; Bartram, P. W., Reactions of Vx, Hd, and Their Simulants with Nay and Agy Zeolites. Desulfurization of Vx on Agy. *Langmuir* **1999**, *15*, 8113-8118.
88. Yang, S. W.; Doetschman, D. C.; Schulte, J. T.; Sarnbur, J. B.; Kanyi, C. W.; Fox, J. D., Sodium X-Type Faujasite Zeolite Decomposition of Dimethyl Methylphosphonate

(Dmmp) to Methylphosphonate: Nucleophilic Zeolite Reactions I. *Microporous and Mesoporous Materials* **2006**, 92 (1-3), 56-60.

89. Singh, V. V.; Jurado-Sanchez, B.; Sattayasamitsathit, S.; Orozco, J.; Li, J. X.; Galarnyk, M.; Fedorak, Y.; Wang, J., Multifunctional Silver-Exchanged Zeolite Micromotors for Catalytic Detoxification of Chemical and Biological Threats. *Adv. Funct. Mater.* 25 (14), 2147-2155.

90. Stout, S. C.; Larsen, S. C.; Grassian, V. H., Adsorption, Desorption and Thermal Oxidation of 2-Ceas on Nanocrystalline Zeolites. *Microporous and Mesoporous Materials* **2007**, 100 (1-3), 77-86.

91. Wagner, G. W.; Bartram, P. W., Reactions of Vx, Hd, and Their Simulants with Nay and Agy Zeolites. Desulfurization of Vx on Agy. *Langmuir* **1999**, 15 (23), 8113-8118.

92. Hudiono, Y. C.; Miller, A. L.; Gibson, P. W.; LaFrate, A. L.; Noble, R. D.; Gin, D. L., A Highly Breathable Organic/Inorganic Barrier Material That Blocks the Passage of Mustard Agent Simulants. *Industrial & Engineering Chemistry Research* 51 (21), 7453-7456.

93. Ramakrishna, C.; Shekar, S. C.; Gupta, A. K.; Saini, B.; Krishna, R.; Swetha, G.; Gopi, T., Degradation of Diethyl Sulfide Vapors with Manganese Oxide Catalysts Supported on Zeolite-13x: The Influence of Process Parameters and Mechanism in Presence of Ozone. *Journal of Environmental Chemical Engineering* **2017**, 5 (2), 1484-1493.

94. Boopathi, M.; Singh, B.; Vijayaraghavan, R., A Review on Nbc Body Protective Clothing. *The Open Textile Journal* **2008**, 1, 1-8.

95. Heled, Y.; Epstein, Y.; Moran, D. S., Heat Strain Attenuation While Wearing NBC Clothing: Dry-Ice Vest Compared to Water Spray. *Aviat Space Envir Md* **2004**, 75 (5), 391-396.
96. Lin, Y. W.; Jou, G. T.; Lin, G. H.; Chang, Y. C.; Lai, T. F., The Evaluation of Thermal Comfort for NBC Protective Garments. In *International Conference on Environmental Ergonomics XII*, Mekjavic, I. B.; Kounalakis, S. N.; Taylor, N. A. S., Eds. Biomed: Piran, Slovenia, 2007; pp 375-378.
97. Pomerantz, N.; Price, S. C.; Zukas, W. X.; Beyer, F. L., Water Transport in Bicontinuous, Phase-Separated Membranes Made from Reactive Block Copolymers. *Army Research Laboratory* **2014**, ARL-TR-7148.
98. Florent, M.; Giannakoudakis, D. A.; Wallace, R.; Bandosz, T. J., Mixed CuFe and ZnFe (Hydr)Oxides as Reactive Adsorbents of Chemical Warfare Agent Surrogates. *J Hazard Mater* **2017**, 329, 141-149.
99. Deng, X. H.; Chen, K.; Tuysuz, H., Protocol for the Nanocasting Method: Preparation of Ordered Mesoporous Metal Oxides. *Chem. Mat.* **2017**, 29 (1), 40-52.
100. Walmsley, F., Synthesis of a Heteropolytungstate and Its Use in Outer-Sphere Redox Kinetics - an Inorganic-Chemistry Laboratory Experiment. *J. Chem. Educ.* **1992**, 69 (11), 936-938.
101. Landers, J.; Neimark, A. V.; Asefa, T.; Vishnyakov, A.; Goswami, A.; Ortiz, J. C. Multicatalyst Polyelectrolyte Membranes and Materials and Methods Utilizing the Same. US20170007871 A1, Jan 12, 2017, 2017.

102. Pesika, N. S.; Stebe, K. J.; Searson, P. C., Determination of the Particle Size Distribution of Quantum Nanocrystals from Absorbance Spectra. *Adv. Mater.* **2003**, *15* (15), 1289-+.
103. Shi, G. M.; Zuo, J.; Tang, S. H.; Wei, S.; Chung, T. S., Layer-by-Layer (LbL) Polyelectrolyte Membrane with Nexar™ Polymer as a Polyanion for Pervaporation Dehydration of Ethanol. *Sep Purif Technol* **2015**, *140*, 13-22.
104. Zuo, J.; Shi, G. M.; Wei, S.; Chung, T. S., The Development of Novel Nexar Block Copolymer/Ultem Composite Membranes for C2-C4 Alcohols Dehydration Via Pervaporation. *ACS Appl Mater Interfaces* **2014**, *6* (16), 13874-83.
105. Wang, J. P.; Wang, Z. Y.; Huang, B. B.; Ma, Y. D.; Liu, Y. Y.; Qin, X. Y.; Zhang, X. Y.; Dai, Y., Oxygen Vacancy Induced Band-Gap Narrowing and Enhanced Visible Light Photocatalytic Activity of ZnO. *ACS Appl. Mater. Interfaces* **2012**, *4* (8), 4024-4030.
106. Vernekar, A. A.; Das, T.; Mugesh, G., Vacancy-Engineered Nanoceria: Enzyme Mimetic Hotspots for the Degradation of Nerve Agents. *Angewandte Chemie-International Edition* **2016**, *55* (4), 1412-1416.
107. Korsvik, C.; Patil, S.; Seal, S.; Self, W. T., Superoxide Dismutase Mimetic Properties Exhibited by Vacancy Engineered Ceria Nanoparticles. *Chemical Communications* **2007**, (10), 1056-1058.
108. Wagner, C. D.; Zatko, D. A.; Raymond, R. H., Use of the Oxygen KII Auger Lines in Identification of Surface Chemical-States by Electron-Spectroscopy for Chemical-Analysis. *Analytical Chemistry* **1980**, *52* (9), 1445-1451.
109. Segawa, A.; Taniya, K.; Ichihashi, Y.; Nishiyama, S.; Yoshida, N.; Okamoto, M., Meerwein-Ponndorf-Verley Reduction of Crotonaldehyde over Supported Zirconium

Oxide Catalysts Using Batch and Tubular Flow Reactors. *Industrial & Engineering Chemistry Research* **2018**, 57 (1), 70-78.

110. Anderson, J. A.; Fierro, J. L. G., Bulk and Surface-Properties of Copper-Containing Oxides of the General Formula $\text{La}_{1-x}\text{Cu}_x\text{O}_3$. *J. Solid State Chem.* **1994**, 108 (2), 305-313.

111. Wang, F.; Chen, D.; Zhang, N.; Wang, S.; Qin, L. S.; Sun, X. G.; Huang, Y. X., Oxygen Vacancies Induced by Zirconium Doping in Bismuth Ferrite Nanoparticles for Enhanced Photocatalytic Performance. *Journal of Colloid and Interface Science* **2017**, 508, 237-247.

112. Morant, C.; Sanz, J. M.; Galan, L.; Soriano, L.; Rueda, F., An Xps Study of the Interaction of Oxygen with Zirconium. *Surface Science* **1989**, 218 (2-3), 331-345.

113. Lousada, C. M.; Johansson, A. J.; Brinck, T.; Jonsson, M., Mechanism of H_2O_2 Decomposition on Transition Metal Oxide Surfaces. *Journal of Physical Chemistry C* **2012**, 116 (17), 9533-9543.

114. Wilmsmeyer, A. R.; Uzarski, J.; Barrie, P. J.; Morris, J. R., Interactions and Binding Energies of Dimethyl Methylphosphonate and Dimethyl Chlorophosphate with Amorphous Silica. *Langmuir* **2012**, 28 (30), 10962-10967.

115. Giannakoudakis, D. A.; Hu, Y.; Florent, M.; Bandoz, T. J., Smart Textiles of Mof/Gc 3 N 4 Nanospheres for the Rapid Detection/Detoxification of Chemical Warfare Agents. *Nanoscale Horizons* **2017**, 2 (6), 356-364.

116. Balow, R. B.; Lundin, J. G.; Daniels, G. C.; Gordon, W. O.; McEntee, M.; Peterson, G. W.; Wynne, J. H.; Pehrsson, P. E., Environmental Effects on Zirconium Hydroxide Nanoparticles and Chemical Warfare Agent Decomposition: Implications of Atmospheric

Water and Carbon Dioxide. *ACS applied materials & interfaces* **2017**, 9 (45), 39747-39757.

117. Giannakoudakis, D. A.; Mitchell, J. K.; Bandosz, T. J., Reactive Adsorption of Mustard Gas Surrogate on Zirconium (Hydr)Oxide/Graphite Oxide Composites: The Role of Surface and Chemical Features. *J. Mater. Chem. A* **2016**, 4 (3), 1008-1019.

118. Kanan, S. M.; Tripp, C. P., An Infrared Study of Adsorbed Organophosphonates on Silica: A Prefiltering Strategy for the Detection of Nerve Agents on Metal Oxide Sensors. *Langmuir* **2001**, 17 (7), 2213-2218.

119. Kuiper, A.; Van Bokhoven, J.; Medema, J., The Role of Heterogeneity in the Kinetics of a Surface Reaction: I. Infrared Characterization of the Adsorption Structures of Organophosphonates and Their Decomposition. *Journal of Catalysis* **1976**, 43 (1-3), 154-167.

120. Liu, F.; Lu, Q.; Jiao, X.; Chen, D., Fabrication of Nylon-6/Poms Nanofibrous Membranes and the Degradation of Mustard Stimulant Research. *RSC Adv.* **2014**, 4 (78), 41271-41276.

121. Okun, N. M.; Tarr, J. C.; Hilleshiem, D. A.; Zhang, L.; Hardcastle, K. I.; Hill, C. L., Highly Reactive Catalysts for Aerobic Thioether Oxidation. *Journal of Molecular Catalysis A: Chemical* **2006**, 246 (1-2), 11-17.

122. Mauritz, K. A.; Moore, R. B., State of Understanding Nafion. *Chem. Rev.* **2004**, 104, 4535-4585.

123. Ruiz-Pesante, O.; Pacheco-Londoño, L. C.; Primera-Pedrozo, O. M.; Ortiz, W.; Soto-Feliciano, Y. M.; Nieves, D. E.; Ramirez, M. L.; Hernández-Rivera, S. P. In *Detection*

of Simulants and Degradation Products of Chemical Warfare Agents by Vibrational Spectroscopy, Defense and Security Symposium, SPIE: 2007; p 10.

124. Crank, J., *The Mathematics of Diffusion*. 2 ed.; Oxford University Press: 1975.